BUBBLES AND PARTICLES IN A CYLINDRICAL ROTATING FLOW

Samenstelling promotiecommissie:

Prof. dr. G. van der Steenhoven, voorzitter	Universiteit Twente
Prof. dr. rer. nat. D. Lohse, promotor	Universiteit Twente
Prof. dr. ir. L. van Wijngaarden, promotor	Universiteit Twente
Prof. dr. A. Prosperetti	Universiteit Twente
Prof. dr. J. Magnaudet	Institut de Mécanique des Fluides de Toulouse
Prof. dr. R. F. Mudde	Technische Universiteit Delft
Prof. dr. ir. J. J. W. van der Vegt	Universiteit Twente
Prof. dr. ir. J. A. M. Kuipers	Universiteit Twente

This research was financially supported by the Dutch Technology Foundation STW (06102) and the Dutch Foundation for Fundamental Research on Matter FOM, which is financially supported by the Dutch Organization for Scientific Research NWO. It was carried out at the Physics of Fluids research group of the Faculty of Science and Technology of the University of Twente.

Nederlandse titel:
Bellen en deeltjes in een cylindrische roterende stroming

Publisher:
Hanneke Bluemink, Physics of Fluids, University of Twente,
P.O. Box 217, 7500 AE Enschede, The Netherlands
pof.tnw.utwente.nl

Cover design: Annemieke Vliegen and Hanneke Bluemink
Print: Gildeprint B.V., Enschede

ISBN 978-90-365-2748-4

BUBBLES AND PARTICLES IN A CYLINDRICAL ROTATING FLOW

PROEFSCHRIFT

ter verkrijging van
de graad van doctor aan de Universiteit Twente,
op gezag van de rector magnificus,
prof. dr. W. H. M. Zijm,
volgens besluit van het College voor Promoties
in het openbaar te verdedigen
op vrijdag 12 december 2008 om 16.45 uur

door

Johanna Jacoba Bluemink
geboren op 9 augustus 1979

te Utrecht

Dit proefschrift is goedgekeurd door de promotoren:

prof. dr. rer. nat. D. Lohse
prof. dr. ir. L. van Wijngaarden

Contents

Chapter 1

Introduction

This chapter provides a short motivation for the research and presents an overview of the motion of bubbles and spheres in different regimes. The differences between bubbles and spheres are discussed, in what way these differences affect the forces acting on them, as well as how the motion of bubbles and spheres is affected by a flow in solid body rotation. The chapter concludes with a guide through the thesis.

1.1 Motivation

Bubbles and particles are found in many natural flow phenomena (for example atmospheric and oceanic flows) and many industrial applications (such as chemical reactions, fluid transport systems, mixing and separation processes). Due to the widespread occurrence of particle or bubble laden flows a lot of research effort is spend to understand, and sometimes control, the behavior of particles and bubbles in different types of flow. In this thesis the research is directed to understanding the fundamental aspects of a single particle or bubble or a pair of particles.

One specific flow type is thoroughly examined: a cylindrically rotating flow where a fluid volume is rotating around a horizontal axis in such a way that no part of the fluid has motion relative to any other part of the fluid, i.e. solid body rotation or, alternatively, rigid-body rotation. The understanding of this type of flow is important on a fundamental level, since the velocity between two points located a small distance apart can be decomposed into two types of motion: a pure straining motion and a rigid-body rotation (Batchelor [5]). The effects of the last type on particle and bubble behavior are studied here. An other reason for interest in this flow type is the occurrence of rotating flow regions in turbulent flows and geophysical flows.

1.2 Bubble and particle motion

In this section we introduce the equation of motion used throughout the thesis and discuss the forces that appear in this equation of motion. A distinction is made between the parameterizations and relevance of the forces on particles and bubbles.

1.2.1 Equation of motion for objects in a fluid

Consider an object with density ρ_b, volume V and projected area A, translating with velocity $\mathbf{v}$ in a fluid with dynamic viscosity μ and density ρ. The equation of motion for the object is given by (Candelier et al. [6], Magnaudet and Eames [19])

$$\begin{aligned} (\rho \mathsf{C}_A + \rho) V \frac{d\mathbf{v}}{dt} &= \rho V (\mathsf{C}_A + 1) \frac{D\mathbf{U}}{Dt} + (\rho_b - \rho) V \mathbf{g} + \\ \frac{1}{2} \rho C_D A |\mathbf{U} - \mathbf{v}| (\mathbf{U} - \mathbf{v}) &+ 6\sqrt{\mu\rho} C_H A \int_0^t \frac{\frac{\partial \mathbf{U}}{\partial \tau}(\tau) + \mathbf{v}\nabla\mathbf{U} - \frac{d\mathbf{v}}{d\tau}(\tau)}{\sqrt{\pi(t-\tau)}} d\tau + \\ &\rho V C_L (\mathbf{U} - \mathbf{v}) \times (\nabla \times \mathbf{U}), \end{aligned} \tag{1.1}$$

where $\mathbf{U}$ is the velocity of the undisturbed ambient flow taken at the center of the bubble. C_A, C_D, C_H and C_L are respectively the added mass, drag, history, and lift coefficients. The left hand side represents a combination of the inertia of the body and a part of the added mass force. The right hand side represents a combination of the added mass due to the spatial gradient of the flow field and the pressure gradient force. These terms are followed by the buoyancy force, the drag force, the history force and the lift force. In order to be able to model the object's behavior, we need to know the parameterizations for the added mass, drag, history and lift coefficients for different flow situations.

High Reynolds numbers

For high Reynolds numbers, the history term in (1.1) is no longer relevant. Analytical results for this regime have been obtained by neglecting viscosity in the Navier-Stokes equations. For a steady inviscid flow with a weak shear Auton [1] has shown that $C_L = 1/2$.

Low Reynolds numbers

For low Reynolds numbers inertia can be neglected. This, however, is not uniformly valid, which can be overcome by using singular perturbation techniques (for example [11, 13, 21, 27, 28]). For unsteady flow the history force becomes relevant in equation (1.1) and in this regime C_H=1. Usually, the lift coefficient for low-Reynolds-number flow is defined by $F_L = 1/2\rho C_L A U^2$.

Intermediate Reynolds numbers

For the intermediate Reynolds numbers no simplification of the Navier-Stokes equation such as neglecting viscosity (high Reynolds numbers) or inertia (low Reynolds numbers) is possible. To obtain a description of bubble and particle behavior in this range, experimental methods or direct numerical simulations (DNS) are used.

1.2.2 Differences between particles and (clean) bubbles

Although (1.1) is used throughout this work, important differences exist between bubbles and particles affecting the drag, lift, and added mass coefficients.

First, the boundary condition on the surface is different for a bubble or a particle. If the liquid is pure enough, it can slip along the surface of a bubble, whereas a rigid particle is subject to the no-slip boundary condition. As a consequence, the velocity perturbation due to a clean bubble is smaller than that due to a particle for $Re \gg 1$. Moreover, the wake region behind a bubble is thinner than behind a particle at equal Reynolds number. The critical Reynolds number Re_c at which the wake of the body becomes unsteady is higher for bubbles than for particles. Furthermore, particles can rotate, giving rise to a Magnus-like lift and thus influencing the lift coefficient. It should be noted that in experiments with non-clean bubbles the surface of such a bubble also rotates.

Due to the large density difference between a fluid and a bubble, inertia-induced hydrodynamic forces are particularly relevant for bubbles.

Another important issue is the deformability of bubbles. This will not only affect the lift and drag forces, but also the added mass force. Below, several parameterizations for the drag, lift and added mass coefficients are discussed.

It should be noted that these difference are valid when comparing clean spherical bubbles with solid spheres. However, it is known that due to surface-active impurities (e.g. [12]) a small fluid inclusion behaves much like a rigid sphere. Therefore we can use rigid spheres to obtain a better understanding of the behavior of surfacted bubbles and some of the parameterizations for spheres may be more applicable to bubbles in an impure fluid than those for clean spherical bubbles. Of course the effects of the deformation in the bubble is not included in these parameterizations and these should be further studied.

History force

The history force is a transient force. In Michaelides [23] a review of the transient forces on particles, bubbles, and droplets is given. In general much more vorticity is created on the surface of a solid sphere than on that of a clean spherical bubble. As a result the history force plays a larger role for solid spheres. For steady state situations there is no history force. In situations where the frequency of the motion is low and the Reynolds number is high, it is negligible.

Drag coefficient

For clean spherical bubbles the drag coefficient can be parameterized for all Re by [19, 22]:

$$C_D = \frac{16}{Re}\left[1+\left[\frac{8}{Re}+\frac{1}{2}(1+3.315Re^{-\frac{1}{2}})\right]^{-1}\right]. \tag{1.2}$$

For solid spheres a much used parametrization, valid for $Re < 800$ is that of Schiller and Neuman [8]:

$$C_D = \frac{24}{Re}[1+0.15Re^{0.687}]. \tag{1.3}$$

For deformed bubbles the drag coefficient changes, it can be expressed in terms of the aspect ratio χ (i.e. major axis / minor axis) as derived by Moore [25]

$$C_D = \frac{48}{Re}G(\chi)\left(1+\frac{H(\chi)}{\sqrt{Re}}\right), \tag{1.4}$$

where

$$G(\chi) = \frac{1}{3}\chi^{4/3}(\chi^2-1)^{3/2}\frac{[(\chi^2-1)^{1/2}-(2-\chi^2)\sec\chi^{-1}]}{[\chi^2\sec\chi^{-1}-(\chi^2-1)^{1/2}]^2}, \tag{1.5}$$

and $H(\chi)$ is tabulated in [25].

In contaminated systems, surfactants will collect at the bubble surface. This changes the surface tension and will make the bubble more rigid, so that it will behave more like a solid sphere. The slip along the surface of the bubble will be decreased, as a result the drag is increased [19].

The drag coefficient also depends on the shear rate. Magnaudet and Legendre [17] indicate for a spherical bubble in a linear shear flow that, when shear rates are in the order of unity, the drag coefficient is strongly increased by shear. From their numerical results they determined an expression for the dependence of the drag coefficient on the non-dimensional shear rate Sr_s

$$C_D = C_{D0}(1+0.55{Sr_s}^2), \tag{1.6}$$

where C_{D0} is the drag coefficient according to Moore for a spherical bubble in a uniform shear flow at high Reynolds number [24].

Lift coefficient

The lift coefficient at low Reynolds numbers is found to depend strongly on the Reynolds number and the shear rate. For moderate to high Reynolds numbers these dependencies are weak [17]. For low Reynolds numbers Saffman [28] and McLaughlin [21] analytically determined the size in a linear shear flow. In case of a low-Reynolds-number linear shear flow, Legendre and Magnaudet [16] calculated that the lift force experienced by a solid sphere is a factor $\frac{9}{4}$ larger than that experienced by a bubble. In the inviscid limit Auton [1], Auton et al. [2] found the lift coefficient to be 1/2. In the intermediate Reynolds range results for bubbles are obtained by DNS (for example Legendre and Magnaudet [17], Magnaudet and Legendre [20]) and experimentally (for example Tomiyama [32]). For spheres numerical results were obtained by Bagchi and Balachandar [4], Dandy and Dwyer [10], Kurose and Komori [14].

Because of the zero-shear-stress boundary condition of a spherical bubble, the flow around the bubble will not induce a rotation of a clean spherical bubble [17]. Particles however can start to spin due to the shear of the flow. This spin will introduce an additional contribution to the lift force since the flow field is changed by the rotation of the particle due to the no-slip boundary condition. Robins described the observation that a projectile spinning about its axis experiences a lift force [29]. Magnus later described this effect for rotating cylinders.

The lift force due to the Robins or Magnus effect F_{L_Ω} is directed normal to the velocity $\mathbf{U}$ and is proportional to the circulation Γ. The lift force on a small disk of the sphere as sketched in figure 1.1 is

$$dF_{L_\Omega} = \rho U \oint (\mathbf{U} \cdot d\mathbf{l}) dz,$$

where $\oint (\mathbf{U} \cdot d\mathbf{l})$ is the circulation Γ along a closed curve as depicted in figure 1.1. For a sphere with radius R rotating with angular velocity Ω_P this results in (by applying Stokes' theorem and noting that the vorticity equals twice the angular velocity of the sphere) an absolute value of

$$F_{L_\Omega} = \rho U 2\Omega_P \int A(z) dz = \frac{8}{3}\pi R^3 \rho U \Omega_P. \tag{1.7}$$

This lift force describes the specific case of a sphere spinning in a uniform flow. For the general case (where the flow may not be uniform) the lift is defined in terms of a lift coefficient throughout this thesis.

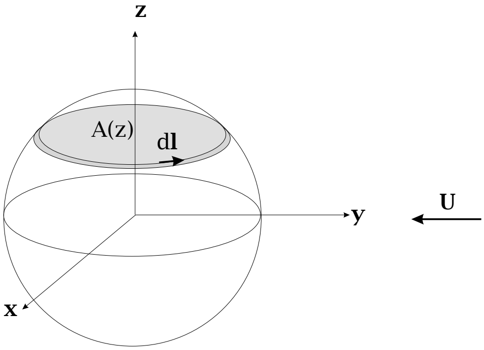

Figure 1.1: Sketch of circulation around a part of a sphere.

Added mass coefficient

The added-mass tensor for a sphere is diagonal and can be represented by an added-mass coefficient, $C_A = 1/2$. Since the added mass force is the reaction of the fluid to acceleration of the body, it takes a different value if the body has different shape. This is represented by the added mass tensor. For an oblate bubble, C_A is [15]:

$$\begin{aligned} C_A &= \frac{\alpha_0}{2-\alpha_0}, && \text{with} \\ \alpha_0 &= \frac{\sqrt{1-e^2}}{e^3}\arcsin(e) - \frac{1-e^2}{e^2}, && \text{where} \\ e &= \sqrt{1-(c/a)^2}, && (a > c), \end{aligned} \tag{1.8}$$

where a and c refer to the semi-major and semi-minor axis of the oblate ellipsoid.

1.2.3 Bubble and particle motion in solid body rotation

Most research for bubble and particle behavior considers uniform flow or linear shear flow. In this thesis the focus is on solid body rotation. In this type of flow the parameterization of the forces may be different, forces that or not relevant in a linear shear flow may become relevant in a solid body rotation and new effects may appear. This section provides a short overview of what modification of particle and bubble behavior we may expect due to the solid body rotation.

Forces due to acceleration of the flow

In the case of a rotating cylindrical system, the flow undergoes an acceleration ($\frac{D\mathbf{U}}{Dt}$). In the laboratory frame, the particle itself does not accelerate. An inertial force directed towards the center of the flow acts on the particle. The inertial force is sometimes referred to as the pressure force [30], because it can be seen as a result of the pressure gradient (due to the centrifugal acceleration) in the cylinder.

Wake interaction

For an object in a solid body rotation, the wake of the object may be advected down so far that it will reach the top of the object again after one revolution. In chapter 4 this mechanism is discussed in detail and possible consequences are considered. The effect is likely to be much smaller for clean bubbles than for solid spheres.

Parameterizations of the lift force in solid body rotation

Most parameterizations for the lift force are for a bubble or particle in a linear shear flow. As will become clear throughout this thesis, forces expressed in terms of coefficients in solid body rotation may take quite different forms than in a linear shear flow. Therefore it is of interest to explore previous work considering specifically the case of solid body rotation. Naciri [26] and Sridhar and Katz [31] both experimentally explored bubbles in this type of flow. Magnaudet and Legendre [20] found by a numerical study which also addresses solid body rotation a parameterization for the lift coefficient for clean spherical bubbles. Bagchi and Balachandar [3] studied the differences between shear and vortex induced lift for solid spheres. In the low but non-zero Reynolds regime Coimbra and Kobayashi [9] used an exact method to solve the Lagrangian equation of motion for a particle in a solid body rotation and the analytical work by Lim et al. [18] explores the history lift effects in a rotating flow. All of the previous cited papers address a cylindrical solid body rotation where the axis of rotation is perpendicular to the direction of the gravitational acceleration. Candelier et al. [6, 7] considered theoretically and experimentally a geometry where the axis of the solid body rotation coincides with the direction of the gravitational acceleration. Their research was for small Reynolds numbers.

1.3 A guide through the chapters

In this chapter the motivation for this research and some background information about particles and bubbles and their behavior in solid body rotation have been presented. In chapter 2 the behavior of bubbles in solid body rotation is addressed for a wide range of Reynolds numbers. The experimental setup for studying bubbles is also described. For the exploration of particle behavior a different experimental setup was used (chapter 4). Before the behavior of particles in solid body rotation is addressed, particle spin is studied in chapter 3. The experimental study of the particle spin rate is confined to spheres in solid body rotation. However, the results are mainly numerical and the differences in the spin rates for different flow types are investigated at moderate Reynolds numbers. Chapter 4 then addresses the experimentally obtained equilibrium positions of particles. The experiments cover a wide Reynolds range.

Since the sphere is the most simple three-dimensional shape, it is often used to model particle laden flows. However, many flow processes involve irregular shapes such as elongated bubbles, and non-spherical particles. Chapter 5 discusses the behavior of particles and bubbles with irregular shapes in a solid body rotation flow.

In chapter 6 hydrodynamic interactions between identical particles are explored, mainly numerically. Again, the flow field under consideration is a solid body rotation. The effects of changing the distance of a particle pair with respect to the cylinder axis are explored.

Chapter 7 connects the conclusions of the different chapters and summarizes the main results for particle and bubble behavior is the horizontal solid body rotation investigated in this thesis.

References

[1] T. R. Auton. The lift force on a spherical body in a rotational flow. *J. Fluid Mech.*, 183:199–218, 1987.

[2] T. R. Auton, J. C. R. Hunt, and M. Prud'Homme. The force excerted on a body in inviscid unsteady non-uniform rotating flow. *J. Fluid Mech.*, 197: 241–257, 1988.

[3] P. Bagchi and S. Balachandar. Shear versus vortex-induced lift force on a rigid sphere at moderate Re. *J. Fluid Mech.*, 473:379–388, 2002.

[4] P. Bagchi and S. Balachandar. Effect of free rotation on the motion of a solid sphere in linear shear flow at moderate Re. *Phys. Fluids*, 14:2719–2737, 2002.

[5] G. K. Batchelor. *An Introduction to Fluid Dynamics*. Cambridge University Press, Cambridge, 1967.

[6] F. Candelier, J. R. Angilella, and M. Souhar. On the effect of the Boussinesq-Basset force on the radial migration of a Stokes particle in a vortex. *Phys. Fluids*, 16:17651776, 2004.

[7] F. Candelier, J. R. Angilella, and M. Souhar. On the effect of inertia and history forces on the slow motion of a spherical solid or gaseous inclusion in a solid-body rotation flow. *J. Fluid Mech.*, 545:113–139, 2005.

[8] R. Clift, J. R. Grace, and M. E. Weber. *Bubbles, drops and particles*. Academics Press, New York, 1978.

[9] C. F. M. Coimbra and M. H. Kobayashi. On the viscous motion of a small particle in a rotating cylinder. *J. Fluid Mech.*, 469:257–286, 2002.

[10] D. S. Dandy and H. A. Dwyer. A sphere in shear flow at finite Reynolds number: effect of shear on particle lift, drag, and heat transfer. *J. Fluid Mech.*, 216:381, 1990.

[11] S. C. R. Dennis, S. N. Singh, and D. B. Ingham. The steady flow due to a rotating sphere at low and moderate Reynolds numbers. *J. Fluid Mech.*, 101: 257–279, 1980.

[12] P. C. Duineveld. The influence of an applied sound field on bubble coalescence. *J. Acoust. Soc. Am*, 99:622, 1996.

[13] E. Y. Harper and I-Dee Chang. Maximum dissipation resulting from lift in a slow viscous shear flow. *J. Fluid Mech.*, 33:209–225, 1968.

[14] R. Kurose and S. Komori. Drag and lift forces on a rotating sphere in a linear shear flow. *J. Fluid Mech.*, 384:183–206, 1999.

[15] H. Lamb. *Hydrodynamics, 6th Edn.* Dover, New York, 1932.

[16] D. Legendre and J. Magnaudet. A note on the lift force on a bubble or a drop in a low-Reynolds-number shear flow. *Phys. Fluids*, 9:3572, 1997.

[17] D. Legendre and J. Magnaudet. The lift force on a spherical bubble in a viscous linear shear flow. *J. Fluid Mech.*, 368:81–126, 1998.

[18] E. A. Lim, C. F. M. Coimbra, and M. H. Kobayashi. Dynamics of suspended particles in eccentrically rotating flows. *J. Fluid Mech.*, 535:101–110, 2005.

[19] J. Magnaudet and I. Eames. The motion of high-Reynolds number bubbles in inhomogeneous flows. *Ann. Rev. Fluid Mech.*, 32:659–708, 2000.

[20] J. Magnaudet and D. Legendre. Some aspects of the lift force on a spherical bubble. *Appl. Sci. Res.*, 58:441–461, 1998.

[21] J. B. McLaughlin. Inertial migration of a small sphere in linear shear flows. *J. Fluid Mech.*, 224:261–274, 1991.

[22] R. Mei, J.F. Klausner, and C. J. Lawrence. A note on the history force on a spherical bubble at finite Reynolds number. *Phys. Fluids*, 6:418–420, 1994.

[23] E. E. Michaelides. Review - the transient equation of motion for particles, bubbles, and droplets. *J. Fluid Eng.*, 119:233–247, 1997.

[24] D. W. Moore. The boundary layer on a spherical gas bubble. *J. Fluid Mech.*, 16:161–176, 1963.

[25] D. W. Moore. The velocity of rise of distorted gas bubbles in a liquid of small viscosity. *J. Fluid Mech.*, 23:749–766, 1965.

[26] M. A. Naciri. *Contribution à l'étude des forces exercées par un liquide sur une bulle de gaz: portance, masse ajoutée et interactions hydrodynamiques*. PhD thesis, L'Ecole Central de Lyon, 1992.

[27] I. Proudman and J. R. A. Pearson. Expansions at small Reynolds numbers for the flow past a sphere and a circular cylinder. *J. Fluid Mech.*, 2:237–262, 1957.

[28] P. G. Saffman. The lift on a small sphere in a slow shear flow. *J. Fluid Mech.*, 22:385–400; and Corrigendum, J. Fluid Mech. **31** p. 624 (1968), 1965.

[29] T. K. Sengupta and S. B. Talla. Robins-Magnus effect: A continuing saga. *Current Science*, 86:1033–1036, 2004.

[30] G. Sridhar and J. Katz. Drag and lift forces on microscopic bubbles entrained by a vortex. *Phys. Fluids.*, 7:389–399, 1995.

[31] G. Sridhar and J. Katz. Effect of entrained bubbles on the structure of vortex rings. *J. Fluid Mech.*, 397:171–202, 1999.

[32] A. Tomiyama. Transverse migration of single bubble in simple shear flows. *Chem. Eng. Sci.*, 57:1849–1858, 2002.

Chapter 2

Bubbles in a rotating flow[‡]

In this chapter the motion of small air bubbles in a horizontal solid body rotating flow is investigated experimentally. Bubbles with a typical radius of 1 mm are released in a liquid-filled, horizontally rotating cylinder. We measure the transient motion of the bubbles in solid body rotation and their final equilibrium position from which we compute drag and lift coefficients for a wide range of dimensionless shear rates $0.1 < Sr < 2$ *(*Sr *is the velocity difference over one bubble diameter divided by the slip velocity of the bubble) and Reynolds numbers* $0.01 < Re < 500$ *(*Re *is based on the slip velocity and bubble diameter). For large* Sr *we find that the drag force is increased by the shear rate. The lift force shows strong dependence on viscous effects. In particular, for* $Re < 5$ *we measure negative lift forces, in line with theoretical predictions.*

2.1 Introduction

Bubbly flows are of great importance in many technical and environmental questions and applications. Therefore understanding the dynamics of bubbles and the forces acting on them is a central issue in multi-phase flow research. These forces result from the integrated stresses acting on their (deformable) surfaces. A full numerical treatment is only possible for a limited number of bubbles. For instance, Tryggvason et al. [29] could simulate at most a few hundred bubbles, rising at moderate Reynolds number ($Re = 20 - 30$), by employing a front-tracking method. To be able to numerically track many more bubbles in an efficient way

---

[‡] E.A. van Nierop, S. Luther, J.J. Bluemink, J. Magnaudet, A. Prosperetti and D. Lohse, *Drag and lift forces on bubbles in a rotating flow*, J. Fluid Mech. **571**, 439-454 (2007).

(for instance to study modifications of turbulence by bubbles), realistic models of the various forces acting on bubbles are required. It is therefore crucial to know how the drag and lift – or, in nondimensional form, the drag and lift coefficients – depend on the particular flow situation, i.e., on the local velocity, shear, or vorticity, etc.

The importance and subtlety of the lift force is reflected in various examples: (i) In upward vertical pipe flow the lateral distribution of bubbles is governed by the lift. The radial bubble migration is found to strongly depend on the bubble size: small bubbles migrate towards the pipe wall, whereas large bubbles tend to accumulate in the center, resulting in a core-peak bubble distribution (Guet et al. [10]). The sign of the lift force is believed to also depend on the bubble's shape. Measurements of lift forces for bubbles in a simple shear flow were carried out at moderate Re by Tomiyama [28]. These measurements indicate negative lift forces for large deformed bubbles, resulting in a lateral motion of the bubbles opposite to that predicted for a spherical bubble by inviscid theory. (ii) Numerical simulations of bubble-laden homogeneous and isotropic turbulent flow show that the role of the lift force is crucial, because it strongly enhances the preferential accumulation of bubbles in the downward flow side of vortices (Climent and Magnaudet [7], Mazzitelli et al. [18, 19]). This results in a considerably reduced rise velocity of the bubbles and an alteration of large-scale motion.

The aim of this work is to experimentally measure the lift and drag forces in a well-defined flow geometry, with well defined and temporal constant flow velocity and vorticity. More specifically, we revisit the experiments by Naciri [21] who studied a bubble in a rotating cylinder, i.e., in a well-defined solid body rotating flow. The advantage of this set-up is that the bubbles reach a stable position. In this equilibrium position the forces acting on the bubble – buoyancy, viscous drag, added mass, inertial (or pressure gradient) force and lift – exactly balance each other. Drag and lift can then be deduced from the known added mass, inertial, and buoyancy forces. As compared to Naciri [21], we considerably extended the studied parameter space and also increased the experimental precision. We also compare our results with those from Sridhar and Katz [25] who studied the force on a bubble placed in a vortex ring.

Related work is described in Rensen et al. [22] where we study the competition between hydrodynamical and acoustical forces and in Lohse and Prosperetti [14]. Complementary work on the analysis of *heavy* particles in solid body rotation is reported in Ashmore et al. [1], Seddon and Mullin [24]; where the focus is on the interaction of the heavy object with the wall.

The outline of this paper is as follows. In Sec. 2.2 the equation of motion of a bubble is introduced, the relevant dimensionless numbers are indicated and previous results for lift and drag coefficients are discussed. The experimental set-up is described in Sec. 2.3. The results for the drag and lift coefficient measurements are stated in Sec. 2.4 followed by concluding remarks in Sec. 2.5.

2.2 Effective forces on bubbles

2.2.1 Dynamical equations, flow field, and dimensionless parameters

For a clean (i.e. uncontaminated by surfactants) spherical bubble rising at moderate-to-large Reynolds number, the approximate force balance is (Magnaudet and Eames [15]):

$$\begin{aligned}\rho_l V_b C_A \frac{d\mathbf{v}}{dt} = \rho_l V_b (C_A+1)\frac{D\mathbf{U}}{Dt} + \rho_l V_b C_L (\mathbf{U}-\mathbf{v}) \times (\nabla \times \mathbf{U}) + \\ \frac{1}{2}\rho_l C_D A |\mathbf{U}-\mathbf{v}|(\mathbf{U}-\mathbf{v}) - \rho_l V_b \mathbf{g}, \qquad (2.1)\end{aligned}$$

where $\mathbf{v}$ is the bubble velocity, $\mathbf{g}$ the gravitational acceleration, ρ_l the liquid density $\gg \rho_g$ the gas density, V_b the bubble volume, and A the projected area of the bubble. $\mathbf{U}$ is the velocity of the undisturbed ambient flow taken at the center of the bubble. This empirical equation is known to hold approximately for $Re > 5$. It depends on three coefficients, two of which are a priori unknown: the lift coefficient C_L, and the drag coefficient C_D. The same equation holds for spheroidal bubbles translating about one of their principal axes. For such spheroidal bubbles, C_A is known (Lamb [12]) and becomes $\frac{1}{2}$ in the spherical case for all Re (Magnaudet and Eames [15]). Equation (2.1) takes into account added mass, inertia, shear-induced lift, viscous drag, and buoyancy. We stress once more that eq. (2.1) is *not* a good description for low Reynolds number particles, as then the lift contribution is not appropriately parameterized and the history force matters, see e.g. Galindo and Gerbeth [8], Legendre and Magnaudet [13], Magnaudet and Legendre [16], Toegel et al. [27], Yang and Leal [30]. We will discuss the applicability of eq. (2.1) in more detail in section 2.2.3.

In a solid-body rotating flow with constant angular velocity ω, see figure 2.1, the undisturbed flow in cylindrical coordinates is:

$$\mathbf{U}(r) = \omega r \hat{\mathbf{e}}_\varphi, \qquad (2.2)$$

with vorticity $\nabla \times \mathbf{U} = 2\omega \hat{\mathbf{e}}_z$. The dimensionless numbers characterizing the

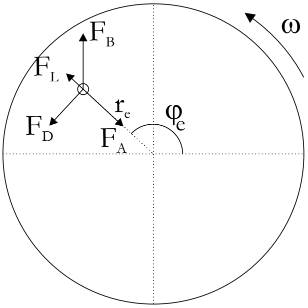

Figure 2.1: Balance of buoyancy, viscous drag, shear-induced lift, pressure gradient and added mass forces. The position of the bubble is given in cylindrical coordinates, in which the rotation and symmetry axis of the cylinder coincide with the z-axis. The cylinder rotates counter-clockwise with constant angular velocity ω.

system are the Reynolds, Strouhal, and Froude numbers,

$$Re = \frac{2R_b|\mathbf{U}-\mathbf{v}|}{\nu}, \qquad Sr = \frac{2R_b\omega}{|\mathbf{U}-\mathbf{v}|}, \qquad Fr = \frac{|\mathbf{U}-\mathbf{v}|^2}{2R_b g} \tag{2.3}$$

Here, R_b is the equivalent bubble radius and ν the kinematic viscosity. Note that the product of the Reynolds and Strouhal numbers results in another "Reynolds" number, Re_ω, which is just the Taylor number, viz.

$$Re_\omega = Re\,Sr = \frac{(2R_b)^2\omega}{\nu}. \tag{2.4}$$

It is known that the Taylor number is the central dimensionless control parameter of particle dynamics in low-Re rotating flows (Gotoh [9], Herron et al. [11]). The Weber number,

$$We = \frac{2R_b\rho_l|\mathbf{U}-\mathbf{v}|^2}{\sigma}, \tag{2.5}$$

determines whether the bubble will be spherical or not. When $We \ll 1$ the bubble can be assumed to be spherical.

2.2.2 Drag force

For a clean spherical bubble in steady motion in a uniform flow, the viscous drag force may be described by introducing the empirical relation due to Mei et al. [20]

for the drag coefficient C_D which matches asymptotic results in the limit of both low and high Re:

$$C_D = \frac{16}{Re}\left[1 + [\frac{8}{Re} + \frac{1}{2}(1 + 3.315Re^{-\frac{1}{2}})]^{-1}\right]. \tag{2.6}$$

Due to contamination of the liquid, surfactants may collect on the bubble surface and the zero-shear-stress boundary condition on the surface may no longer be valid. The viscous drag then increases and, for many surfactants, approaches that of a solid sphere, as indicated (for example) by the measurements by Maxworthy et al. [17], Naciri [21], Sridhar and Katz [25]. For a solid sphere one of the most widely used parameterizations for the drag coefficient is (Clift et al. [6]):

$$C_D = \frac{24}{Re}\left[1 + 0.15Re^{0.687}\right]. \tag{2.7}$$

Shear effects also increase the viscous drag force by broadening the near wake. Numerical simulations of a bubble in a linear shear flow of Legendre and Magnaudet [13] reveal a significant dependence of the drag coefficient on the dimensionless shear rate (Sr) for moderate-to-large Re (typically $Re \geq 50$). Whereas the drag remains essentially unaffected for $Sr \leq 0.2$, a huge increase is observed for $Sr = \mathcal{O}(1)$. From their numerical data they found the relation:

$$C_{D,Sr} = C_{D0}(1 + 0.55\,Sr^2), \tag{2.8}$$

where C_{D0} is the drag coefficient in the absence of shear.

2.2.3 Lift force

There have been various theoretical and numerical investigations of the lift force experienced by rigid spheres and bubbles in vortical flows. For a quasi-steady weak (i.e. $Sr \ll 1$) linear shear flow, Auton [2] analytically predicted the lift coefficient involved in (2.1) to be $\frac{1}{2}$ in the inviscid limit. Auton et al. [3] combined this result with that of Taylor [26] for the force on a sphere in an unsteady strained flow. In the limit of weak vorticity and unsteadiness, they showed that Auton's (1987) result may simply be added to Taylor's (1928) result, yielding the inviscid part of (2.1).

As pointed out above, an experiment similar to the present one was carried out by Naciri [21]. He experimentally found the lift coefficient to depend on the Froude number for $0.3 < Fr < 2.6$ and parameterized this dependence as:

$$C_L^N = \frac{1}{2}(1 + C_A) - \frac{0.81}{\sqrt{Fr}} + \frac{0.29}{Fr}. \tag{2.9}$$

The superscript “N” stands for Naciri. The range of Reynolds numbers covered in these measurements is between 10 and 2500 and the bubble radii ranged from 0.4 to 6 mm.

Similarly, Sridhar and Katz [25] studied bubbles entrained in vortices produced by a vortex ring generator. This is not solid body rotation, because vorticity decays away from the core. Moreover the authors used tap water, so that their bubbles were contaminated by surfactants. The measured lift coefficients were found to be almost independent of the Reynolds number but dependent on the shear rate through the following empirical relation:

$$C_L^{SK} = 0.22\, Sr^{-0.75}, \tag{2.10}$$

for $20 < Re < 80$, $0.004 < Sr < 0.09$ and bubble radii ranging from 0.25 to 0.4 mm. The measured lift coefficients were substantially larger than theoretical predictions, which is not very surprising since the low- (resp. high-) Re results were compared with Saffman’s (1965) result (resp. with Auton’s (1987) result), both of which were derived for a pure shear flow. Other empirical correlations are based on numerical simulations of the detailed flow structure around a sphere. Bagchi and Balachandar [4] studied vortex-induced lift for a rigid sphere at moderate Re in the range 10 to 100 and weak vorticity ($0.04 < Sr < 0.1$). They found a significantly enhanced positive lift coefficient for vortex flows in agreement with the measurements of Sridhar and Katz [25] and again at odds with predictions from inviscid and low-Re theories.

In a solid-body rotating flow with constant angular velocity ω, both the shear-induced lift force ($\mathbf{F}_L$) and the added mass and inertial force ($\mathbf{F}_A$) acting on a bubble in equilibrium have only radial components, and can be combined in terms of a rotational lift coefficient. In the inviscid limit, this yields for a bubble at rest

$$\mathbf{F}_L + \mathbf{F}_A = \rho_l V_b \left[C_L \mathbf{U} \times (2\omega \hat{\mathbf{e}}_z) + (C_A + 1)\frac{D\mathbf{U}}{Dt} \right] = \\ \rho_l V_b \omega^2 r_e [2C_L - (C_A + 1)]\, \hat{\mathbf{e}}_r = 2C_{L\Omega} \rho_l V_b \omega^2 r_e\, \hat{\mathbf{e}}_r, \tag{2.11}$$

where r_e is the equilibrium radial position of the bubble (see figure 2.1) and the rotational lift coefficient is defined as:

$$C_{L\Omega} = C_L - \frac{1}{2}(1 + C_A), \tag{2.12}$$

For a sphere, (2.12) results in $C_{L\Omega} = -\frac{1}{4}$, indicating that the direction of the total lift force is opposed to that found in a simple shear flow. This is because the inertial and added-mass forces (which are strictly zero in a linear shear flow) are centripetal in a solid-body rotation flow and exceed the centrifugal shear-induced lift force. Magnaudet and Legendre [16] obtained an empirical expression from numerical simulations for the rotational lift coefficient for a spherical shear-free bubble in solid-body rotation for $10 < Re < 1000$ and for weak to moderate shear ($0.02 < Sr < 0.2$), namely

$$C_{L\Omega}^{ML} = -0.25 + 1.2\,Re^{-\frac{1}{3}} - 6.5\,Re^{-1} + \mathcal{O}(Re^{-1}) \tag{2.13}$$

While (2.1) is widely used to track bubbles over a wide range of Reynolds numbers, it must be realized that it is inadequate in the low-Re regime. For instance, in the flow considered here, the inertial and added-mass contributions provided by the fluid acceleration are of $O(ReSr)$ (adopting a scaling in which the viscous drag is of $O(1)$), so that they are negligibly small compared to contributions like the history force which is neglected in (2.1). More importantly, the expression of the shear-induced lift force involved in (2.1) (the second term on the right-hand side) is specific to moderate or large Re. In contrast to this $O(ReSr)$ lift contribution, low-Re shear-induced lift forces are of $O((ReSr)^{\frac{1}{2}})$ as first shown by Saffman [23]. Hence they provide the dominant hydrodynamic contribution to the radial force balance. The reason why the low- and high-Re scalings of the shear-induced lift force are different is because the underlying physics differ from each other. At large Reynolds number, the shear-induced lift force taken into account in (2.1) results from the tilting of the upstream vorticity around the bubble which is a body of finite span, like an airfoil. This tilting induces a nonzero streamwise component of the vorticity in the wake, which gives rise to a pair of counter-rotating vortices (Fig. 2.2). The flow created by this pair of vortices results in a force $\mathbf{F_L}$ which, in a pure linear shear flow as well as in the solid-body rotation considered here, tends to push the body towards the high relative velocity side (as pointed out earlier, besides this shear-induced force there is in general another contribution to the lift which is due to the fluid acceleration $D\mathbf{U}/Dt$, and which in the present flow is dominant and makes the total lift force centripetal).

In contrast, the low-Re picture relies on the far-field flow in which the disturbance produced by the body (i.e. the force due to the Stokeslet associated with the body) generates small inertial and viscous contributions of similar magnitude which in turn produce a small uniform flow in the vicinity of the body. The direction of this uniform flow is generally not aligned with that of the primary flow, resulting in a lift force. For a bubble or a rigid sphere moving along a simple shear flow, this force has the same direction as its high-Re counterpart but the two mechanisms differ. At low Reynolds number, the sign of the force results from the displacement of fluid particles in the far-wake relatively to the ambient flow,

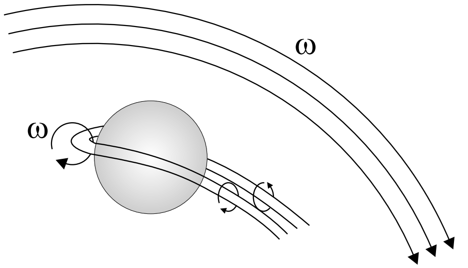

Figure 2.2: Sketch of the shear-induced lift mechanism in the high-Re regime. The vortex pair behind the bubble induces a lift force.

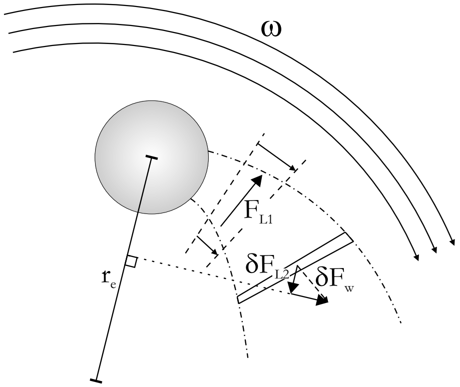

Figure 2.3: Sketch of the lift mechanism in the low-Re regime. There are two opposite contributions $\mathbf{F_{L1}}$ and $\mathbf{F_{L2}}$ to the lift force. For a detailed description of the mechanism see the end of section 2.2.3.

which increases (if the particle is fixed) in the direction of increasing velocities, resulting in a lateral pressure gradient which tends to move the particle in the same direction. This was the situation considered in the pioneering work of Saffman. While determining the sign of the low-Re lift force on the grounds of simple physical arguments is relatively easy in this case, it is frequently less intuitive when the particle moves at an arbitrary angle to the base flow or when the latter is not unidirectional. In the situation we are considering here, two opposite effects are competing. First, given the linear increase of the undisturbed velocity with the local radius r, the velocity difference between the outer (undisturbed) flow and the defect velocity within the wake is larger on the outward side of the wake than on the inner side. This effect, similar to that encountered with a fixed particle embedded in a pure shear flow, results in a centrifugal lift force ($\mathbf{F_{L1}}$ in Fig. 2.3). On the other hand, it must be borne in mind that the wake centreline approximately fol-

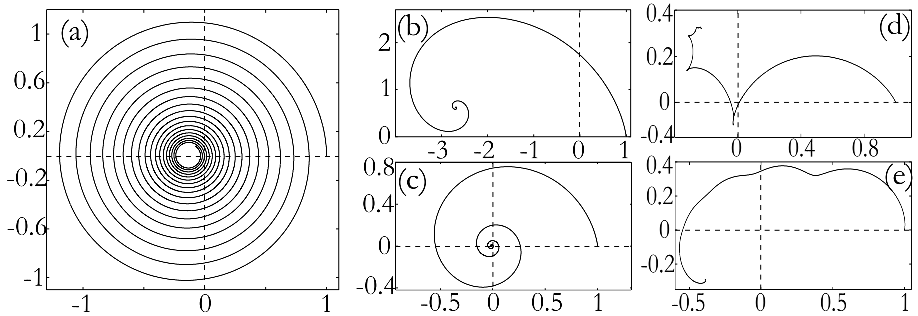

Figure 2.4: Theoretical bubble trajectories for different values of Re_ω and C_L: (a) Spiral with $Re_\omega = 0.1$, (b) spiral with $Re_\omega = 1$, (c) spiral with $Re_\omega = 10$, (d) cycloid with $Re_\omega = 50$ and (e) non-spiral with $Re_\omega = 50$. In (a)-(d) $C_L = 0.5$, while in (e) $C_L = 0.9$; $R_b = 0.5$ mm in all cases. The bubble was released from (1,0) each time, both x and y axes are in mm.

lows the streamlines of the base flow, i.e. the wake is curved by the external flow. Then, considering that any slice of wake results in an infinitesimal force $\delta\mathbf{F_w}$ perpendicular to its plane and directed downstream, it is immediately seen in Fig. 2.3 that the total wake-induced force $\mathbf{F_w} = \int \delta\mathbf{F_w}$ obtained by integrating along the wake consists of a drag force and a centripetal contribution ($\mathbf{F_{L2}}$ in Fig. 2.3). The question is then which of the centrifugal and centripetal lift contributions, both of which are of $O((ReSr)^{\frac{1}{2}})$, is larger. There seems to be no rational way to settle this question on the basis of simple qualitative arguments. However the full theoretical determination of the corresponding transverse force for a fixed sphere embedded in a solid-body rotation flow was achieved by Gotoh (1990) under asymptotic conditions identical to those considered by Saffman [23]. His result indicates that the centripetal effect is dominant, which implies that the lift coefficient is negative if the force is expressed using the inertial scaling of (2.1). Interestingly, the prefactor of this $O((ReSr)^{\frac{1}{2}})$ centripetal force is about six times smaller than that of the Saffman shear-induced lift force, a reduction which may be interpreted as a direct consequence of the competition between the two opposite contributions $\mathbf{F_{L1}}$ and $\mathbf{F_{L2}}$. The most important conclusion we can draw from the above considerations is that the mechanisms responsible for the shear-induced lift force are deeply different in the high- and low-Re regime. In the particular case of a fixed sphere embedded in a solid-body rotation flow, we expect this force to change from centrifugal to centripetal as the Reynolds number is decreased.

2.2.4 Trajectories and equilibrium bubble position

We now show typical bubble trajectories as they follow from the dynamical equation (2.1) with assumed drag and lift coefficients. Figure 2.4 shows the trajectory of the bubble for different values of $Re_\omega = (2R_b)^2\omega/\nu$ and C_L. To calculate these theoretical trajectories, C_A was assumed to be $\frac{1}{2}$ and (2.7) was used for C_D. For higher Re_ω and C_L (figure 2.4, (d) and (e)), the trajectories tend to go from spiralling towards cycloidal motion.

Finally, the bubble will reach an equilibrium position (r_e, φ_e) where all forces acting on it balance as shown in figure 2.1. The axial position is kept fixed, as for small enough bubbles there is no axial asymmetry capable of inducing forces acting in the axial direction. (Note that for large bubbles in the $R_b \sim 1$ cm-regime this can change (Bluemink et al. [5]). From the equation of motion (2.1) we therefore have two balance equations – one in the radial and one in the azimuthal direction – which for the equilibrium situation $\dot{r} = \ddot{r} = \dot{\varphi} = \ddot{\varphi} = 0$ can be solved for r_e and φ_e,

$$\tan\varphi_e = \frac{8}{3}\frac{R_b}{C_D r_e}(2C_L - 1 - C_A), \tag{2.14}$$

$$r_e = \frac{-g\sin\varphi_e}{\omega^2(2C_L - 1 - C_A)}, \tag{2.15}$$

Here the flow field from (2.2) has been used. The final position of the bubble (r_e, φ_e) depends on ω, R_b, ρ_l, g, and on the kinematic viscosity of the fluid ν (since it influences the values of C_D and C_L). Vice versa, the equilibrium position (r_e, φ_e) of the bubble directly reveals the lift coefficient C_L and the drag coefficient C_D,

$$C_L = \frac{1}{2}\left[1 + C_A - \frac{g\sin\varphi_e}{r_e\omega^2}\right], \tag{2.16}$$

$$C_D = -\frac{8}{3}\frac{R_b}{r_e^2\omega^2}g\cos\varphi_e. \tag{2.17}$$

R_b, ω and ν are the variables that can be adjusted in the experiment. The response of the system is reflected in the equilibrium position (r_e, φ_e) (Fig. 2.1), characterized by $\mathbf{v} = 0$. The equilibrium radius can be expressed in the dimensionless numbers of eqs. (2.3) and (2.5), namely

$$Re = \frac{2R_b\omega r_e}{\nu}, \qquad Sr = \frac{2R_b}{r_e}, \qquad Fr = \frac{\omega^2 {r_e}^2}{2R_b g}, \qquad We = \frac{2R_b\rho_l\omega^2 r_e^2}{\sigma}. \tag{2.18}$$

In both simulations and experiments, we find that the bubble equilibrium position is stable. In experiment, we test the stability by disturbing the bubble at equilibrium with another bubble of similar size. Once that second bubble approaches the bubble at equilibrium, this first bubble is kicked out off the equilibrium position, but then re-approaches it again. To further support the stability of the equilibrium position, a linear stability analysis was done for (r_e, φ_e) in (2.1), indeed confirming stability as long as $\rho_l > \rho_b$.

2.3 Experiment

2.3.1 Setup, uncertainties, and data analysis

The experimental apparatus is sketched in figure 2.5. A glass cylinder of 500 mm length and 100 mm inner diameter, is filled with de-ionized water or a water-glycerin mixture and is rotated with an angular velocity ω in the range of $2-35$ rad s^{-1} $\pm 0.5\%$ (at high rotation rates mechanical vibrations introduce additional errors). A bubble is injected approximately midway the length of the cylinder. The bubble size is controlled such that R_b is typically around 1 mm (uncertainty $\pm$ 2%), corresponding to $We \ll 1$ in the glycerin/water mixtures and $We \lesssim 1$ in water so that the bubble shape is essentially spherical. The transient motion of the bubble and its equilibrium position are recorded with a digital camera.

By image processing, the equilibrium position of the bubble (r_e, φ_e) is obtained, and from this Re and Sr are determined. The experiments were conducted with Re in the range $10^{-2} - 10^{3}$ and Sr varying between 0.1 and 2. As the rotation rate is decreased, the equilibrium radius r_e increases. Therefore there is a lower limitation on ω in order to avoid wall effects. In general, for low-Re and high rotation rates, equilibrium positions are close to the rotation axis and therefore accompanied by low accuracy of the r_e and φ_e measurements. Considerable effort was made to reduce the experimental errors and uncertainties to a minimum for these low-Re experiments. In order to have a reliable measurement of the equilibrium position, the camera was placed on a 2-way rotatable, $x-y-z$ translation stage to align the optical axis as precisely as possible with the axis of rotation of the cylinder. Additionally, the location of the rotation axis in the digital images was determined by linear extrapolation of the center-positions on the front and back end of the cylinder. Image analysis demonstrated a final uncertainty in the x, y position of the bubble center of no more than 0.75 pixels. Finally, the uncertainty in r_e was between 3-7%, and the uncertainty in φ_e was between 0.1°-4°, depending on the final bubble position.

For the water-glycerin mixtures, the viscosity ν and density ρ_l were measured using standard equipment, and the resulting accuracies are $\pm$ 5% and $\pm$ 0.1% respectively. The accuracy of the surface tension σ was estimated to be 0.5%. The

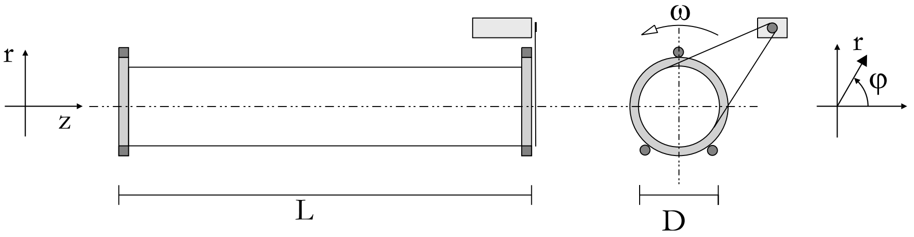

Figure 2.5: Sketch of the experimental setup. (left) Side view: glass cylinder of length $L = 500$ mm. The cylinder axis is aligned with the z-axis of the coordinate system. (right) Axial view: the cylinder has diameter $D = 100$ mm. The end caps rest on ball bearings. A DC motor drives the cylinder on the right end cap via a toothed belt at constant rotation rate ω.

systematic uncertainties of compounded quantities (such as Re, Sr, etc.) were determined from the systematic component uncertainties by the standard error propagation method. For the case of Sr this e.g. leads to $\frac{\Delta Sr}{Sr} = \frac{\Delta R_b}{R_b} + \frac{\Delta r_e}{r_e}$, implying that the uncertainties in Sr range from 5-9$\%$.

Image sequences are typically recorded at 500 frames per second. The effect of inhomogeneous background illumination is removed by subtracting an empty background image, after which a global grey level threshold is applied for image segmentation. For each frame in the image sequence, the position of the cylinder center, that of the centroid of the bubble and the length of its major and minor axes are computed.

2.3.2 Sphericity of bubbles and flow field uniformity

For 60 out of 78 recorded bubbles, the aspect ratio (major/minor axis = χ) was below 1.1. Data points for which the shape was less spherical (i.e., points corresponding to bubbles with an aspect ratio larger than 1.1) are indicated as such in the figures. The largest observed aspect ratio was 1.66 (for a bubble with $R_b = 1$ mm, $Re = 622$, and $\omega = 34.9$). Note that the aspect ratio of the bubbles (oblate spheroids) is taken into account when calculating C_A (Lamb [12]) and hence (through eqs. (2.16) and (2.17)) C_L etc. For $\chi = 1.1$ one obtains C_A = 0.56, about a 10$\%$ increase as compared to the spherical case.

The approximate sphericity of the bubbles is confirmed by formally calculating the Weber number according to eq. (2.18). Indeed, all of the bubbles considered in the present analysis have $We \leq$ 2.66; the average Weber number is only 0.54. The bubble with the largest Weber number $We = 2.66$ also has the largest measured

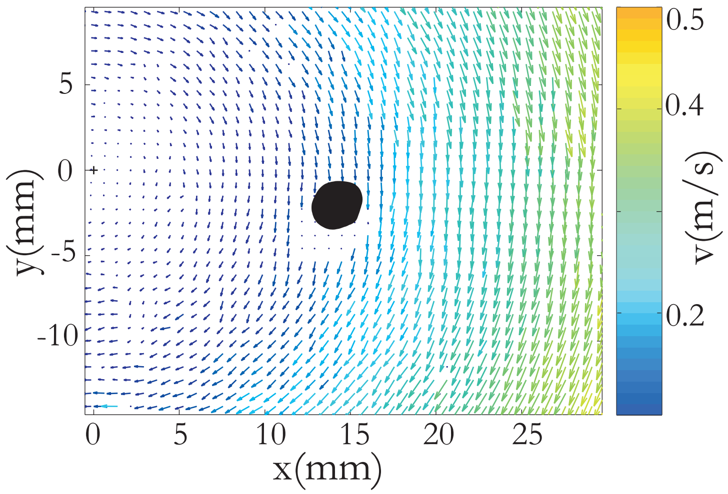

Figure 2.6: Flow field around a large bubble ($R_b \approx 1.5$ mm) at equilibrium, as measured by particle image velocimetry (PIV). Note how the influence of the bubble is negligible just a few bubble-diameters downstream. In this case, $Sr = 0.21$, $Re = 585$. PIV images for further cases with different Sr and Re and more details on the method can be found in ref. Bluemink et al. [5].

aspect ratio, namely 1.66. Results for larger bubbles have already been given in Bluemink et al. [5]; for these large bubbles the phenomenology is rather different as they deform to such a degree that off-diagonal elements of the added mass tensor become relevant, leading to a motion of the bubble along the axis of the cylinder.

The quality of the flow field and the influence of the wake behind the bubbles on their equilibrium position were studied using particle imaging velocimetry (PIV). As can be seen in figure 2.6, even for a relatively large bubble, the wake quickly decays and does not seem to affect the incident flow on the bubble. Therefore we consider it reasonable to assume that the flow field is in a state of uniform solid body rotation. Also order of magnitude estimates indicate that indeed the wake should be negligible for $Sr < 1$. In our current data Sr is smaller than 3 for all bubbles and only for 8 bubbles is it between 1 and 3.

2.4 Experimental results for bubbles in vortical flow

2.4.1 Trajectories

Figure 2.7 shows typical experimental trajectories for Reynolds numbers in the range from 102 to 622. Figure 2.7 (a) and (b) show spirals; the lower the angular velocity, the more slowly the bubble moves inwards leading to a more closely wound spiral. In other words, increasing the shear rate reduces the entrapment time. Also, as Sr increases, the equilibrium position shifts away from the cylinder center. As both Re and Sr increase, the trajectories become more complex and resemble cycloids as seen in figure 2.7 (c) and (d). Once the bubble has reached the vicinity of the equilibrium position, it seems to be captured on an erratic trajectory. We interpret this motion as jitter due to lack of stability in ω and in the horizontal alignment of the system. Note that both spiraling and cycloidal motions are found in experiments (figure 2.7) as well as in simulations (figure 2.4). For both, we find that cycloidal motion is predominant for large Re and/or Sr. Attempts were made to numerically integrate (2.1) using experimental data as inputs, thus providing a direct comparison between numerics and experiment. The agreement between the numerical integration and experiment was reasonable at best, indicating that the models for $C_L(Re, Sr)$ input into the numerical integration are not accurate enough. Additional problems in these comparisons arise from the fact that "real" bubbles have a finite eccentricity which introduces added mass components parallel to the direction of bubble motion, not accounted for in the numerical simulations. In section 2.5 we re-address the difficulty of numerically reconstructing the whole bubble trajectory.

2.4.2 Equilibrium positions

Drag coefficient

Figure 2.8 shows the measured dependence of the drag coefficient C_D on the Reynolds number, as calculated from the equilibrium position (cf. eq. (2.17)). Additionally, the drag curves for a clean spherical bubble (2.6) and a solid sphere (2.7) in a uniform flow are shown. We would expect the drag coefficients to fall in between the two lines indicating a certain amount of contamination of the system. However, the measured drag coefficients (open symbols in figure 2.8) are systematically above the solid drag curve. As indicated by the error bars, measurement errors cannot explain this effect. Taking a closer look at Sr for the different data points reveals that the deviation from the solid drag curve is larger when Sr is larger. Assuming that the drag coefficient depends on the shear rate as given in (2.8), the measured $C_{D,Sr}$ coefficients can be shear-compensated, i.e. we can es-

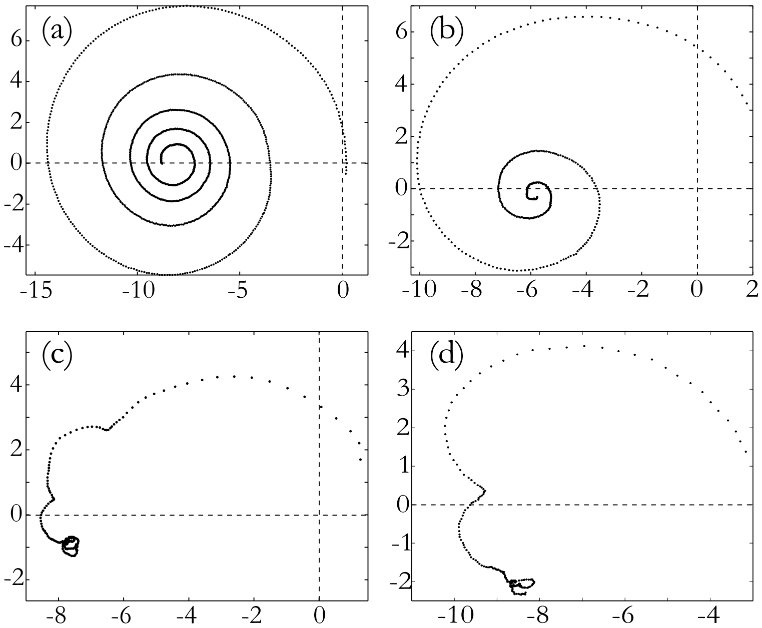

Figure 2.7: Typical experimental trajectories of the bubble: (a) $Re = 102$, $\omega = 15$ rad s^{-1}, $R_b = 0.4$ mm, $Re_\omega = 10$; (b) $Re = 186$, $\omega = 23.3$ rad s^{-1}, $R_b = 0.7$ mm, $Re_\omega = 45$; (c) $Re = 400$, $\omega = 35$ rad s^{-1}, $R_b = 0.7$ mm, $Re_\omega = 69$; (d) $Re = 622$, $\omega = 35$ rad s^{-1}, $R_b = 1.0$ mm, $Re_\omega = 140$. Both axes are in mm, and the center of the cylinder corresponds to $x = 0$, $y = 0$.

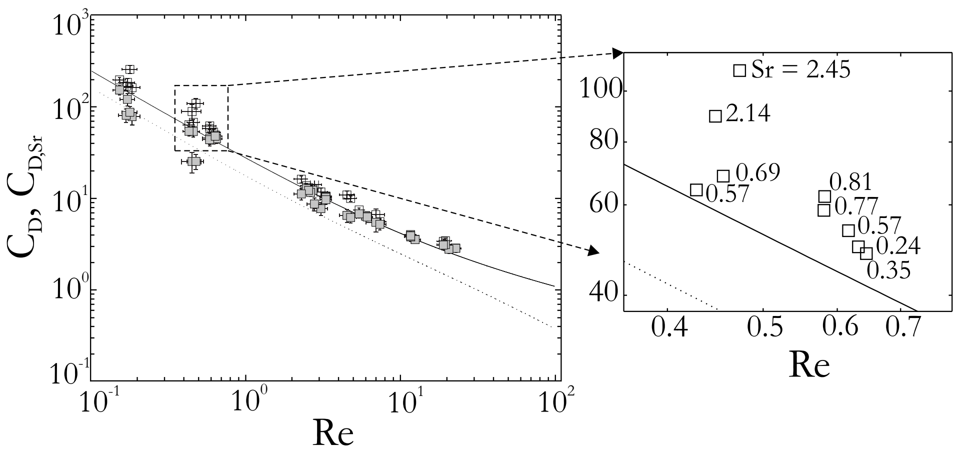

Figure 2.8: Drag coefficient versus Reynolds number. The drag coefficients C_D are indicated by open symbols. The corresponding closed symbols indicate the coefficients $C_{D,Sr}$ with shear correction according to (2.8). The solid line represents the drag coefficient for solid spheres, (2.7). The dashed line is for clean spherical bubbles according to (2.6).

timate the drag coefficient C_{D0} that the bubble would have if it were embedded in a uniform flow. The result of such a compensation is shown in figure 2.8 (closed symbols); compensated drag coefficients tend to fall in between the drag curves for a clean spherical bubble and a solid sphere, indicating that the shear in solid body rotation modifies the drag in a qualitatively similar fashion as in a linear shear flow.

Lift coefficient

Figure 2.9 shows the dependence of the lift coefficient on Sr, over three decades of Sr. In this plot we compare our results with available data from Sridhar and Katz [25] and Naciri [21]. There is some discrepancy between our measurements and Sridhar & Katz's extrapolated fit, but this discrepancy decreases with increasing Re.

Figure 2.10 shows the available data versus $Fr^{1/2}$. It summarizes the measurements of Naciri and our data in glycerin-water mixtures and water. The empirical fit suggested by Naciri does not hold for our data, and hence the Froude number does not seem to be an adequate parameter to describe our results.

Figure 2.11 shows the dependence of the lift coefficient on Re. While Srid-

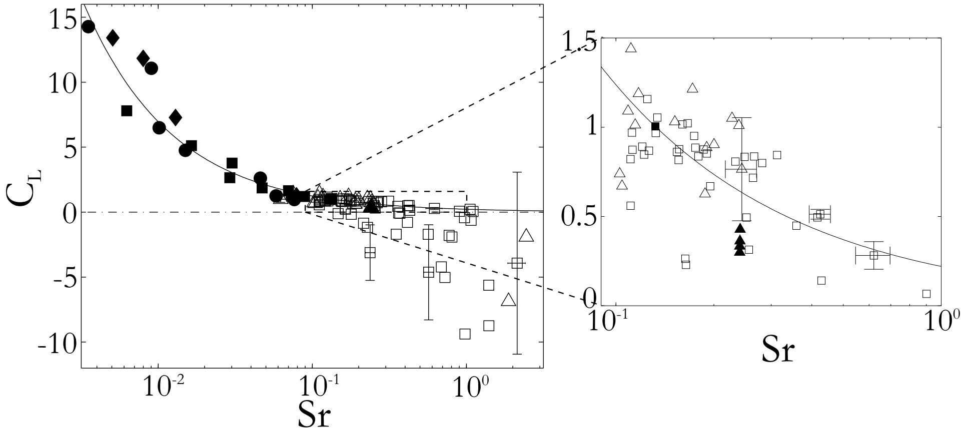

Figure 2.9: Lift coefficient C_L versus Strouhal number Sr: our data sets with a bubble aspect ratio $\chi > 1.1$ (△) and with $\chi < 1.1$ (□), Sridhar & Katz's data (■: $20 < Re < 30$, •: $50 < Re < 70$, ♦:$65 < Re < 80$), and Naciri's data (▲, taken from Sridhar and Katz [25]). Superposed is the empirical model suggested by Sridhar & Katz (eq. (2.10), solid line). The inset shows the spread of our data more clearly, including some typical error bars.

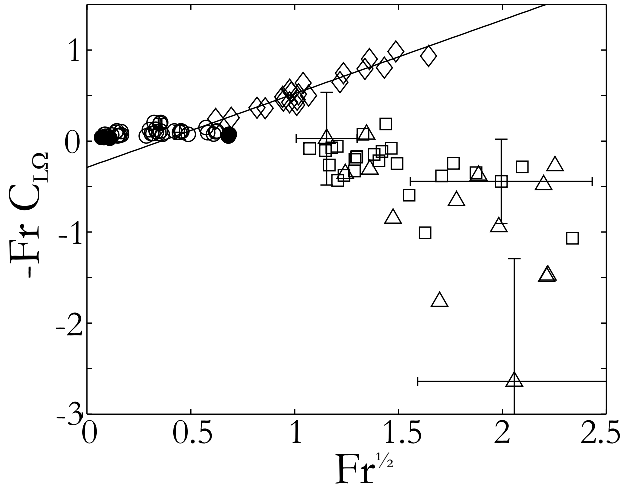

Figure 2.10: $-FrC_{L\Omega}$ versus $Fr^{1/2}$: glycerine-water results (○ for a bubble aspect ratio $\chi < 1.1$ and • for $\chi > 1.1$), results for water (□ and △ for $\chi < 1.1$ and $\chi > 1.1$ respectively) and Naciri's results (◇) taken from Fig.II.6 in Naciri [21]. Superposed is the empirical fit suggested by Naciri (2.9), which cannot describe the present data.

har and Katz [25] noted that their data for C_L did not seem to depend on Re, our measurements indicate a strong dependence on Re at low Re. Moreover the shear-induced lift coefficient C_L is found to be negative for $Re < 5$ (a Re range in which Sridhar & Katz did not measure C_L), as the rotational lift coefficient $C_{L\Omega} < -\frac{3}{4}$ in this range (cf.(2.12)). Figure 2.11 contains data from our experiments (triangles & squares) and numerical data (circles) obtained by Magnaudet and Legendre [16]. For $Re > 5$ both the experiments and the simulations are in good agreement with the high-Re theoretical prediction. In particular, for large Re they both converge to the asymptotic value of $C_{L\Omega} = -\frac{1}{4}$ corresponding to $C_L = \frac{1}{2}$. For $Re < 5$ the numerical results show a strongly decreasing trend for C_L which becomes negative for small enough Re. The experimental data show a similar but even more pronounced trend, the shear-induced lift coefficients becoming *negative* when $Re < 5$. Hence it appears that the transition between the high-Re and low-Re mechanisms for the generation of the shear-induced lift force discussed in Sec.2.2.3 occurs around $Re = 5$. This is not totally unexpected, as Magnaudet and Legendre [16] observed the same trend in a linear shear flow. More precisely they found the low-Re scaling involved in Saffman's (1965) and McLaughlin's (1991) predictions to apply for $Re < 2$, approximately, and the two regimes to match around $Re = 5$.

According to the low-Re theory, $C_{L\Omega}$ should be proportional to $(ReSr)^{-\frac{1}{2}}$ in the corresponding regime, provided $(Sr/Re)^{\frac{1}{2}}$ is much larger than unity (Gotoh [9], Herron et al. [11]). However our experimental values for the quantity $C_{L\Omega}(ReSr)^{\frac{1}{2}}$ in the range $Re < 5$ are not constant and still decrease significantly as Re goes to zero. This may be due to the fact that the ratio Sr/Re is not large enough in several cases or to the influence of the bubble wake, keeping in mind that r_e tends to zero with Re so that the incident flow "seen" by the bubble is not strictly in solid-body rotation. Finally, the experimental accuracy on r_e and φ_e may also be questioned in this regime. We plan to perform new experiments in this regime to clarify this point.

2.5 Conclusion

In conclusion, the motion of a single bubble in a solid body rotational flow was studied experimentally. Drag and lift coefficients have been obtained from the measured equilibrium position of the bubble. The dependence of the drag and lift coefficients on shear rate and Reynolds number has been studied over a wide range of Sr and Re. The two main findings of this paper are: (i) there is a significant shear dependence of the drag coefficient for strong shear and (ii) there is a remark-

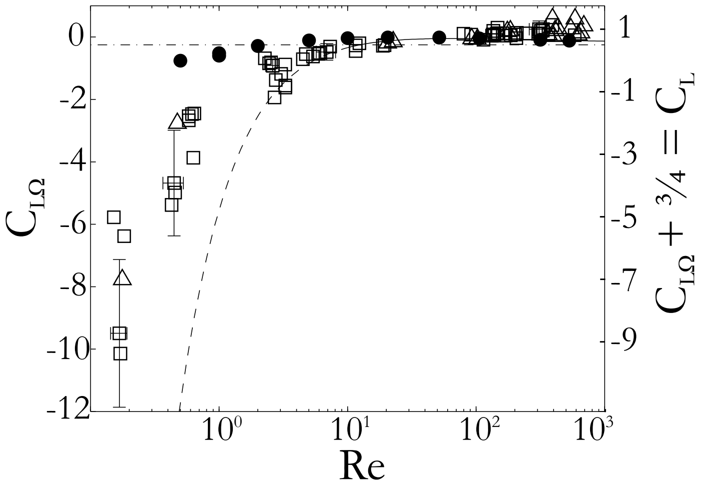

Figure 2.11: Rotational lift coefficient $C_{L\Omega}$ versus Reynolds number Re. The measured rotational lift coefficients $C_{L\Omega}$ and typical error bars are indicated by □ and △ for $\chi < 1.1$ and $\chi > 1.1$, respectively. The solid circles are results of numerical simulations from Magnaudet and Legendre [16]. The dot-dashed line is the asymptotic value $C_{L\Omega} = -1/4$ for $Re \to \infty$. The solid line (for $Re > 10$) and dotted line (for $Re < 10$) comes from (2.13) which is valid for $Re \geq 10$. The right axis shows the corresponding lift coefficient C_L, calculated with the assumption that $C_A = 1/2$.

able change of sign in the lift force in solid body rotation around $Re = 5$. The aforementioned strong shear dependence of C_D is in agreement with previous numerical predictions by Legendre and Magnaudet [13]. Even though their prediction was made for linear shear flow, it seems to be valid for the case of solid body rotation also. We find a significant dependence of the lift coefficient on Sr and Re, especially for strong shear and small Re. For $Re > 5$ we find that the total (rotational) lift coefficient $C_{L\Omega}$ is negative but its values are larger than $-\frac{3}{4}$, yielding positive values of the shear-induced lift coefficient C_L. This is in agreement with predictions from inviscid theory (Auton [2]). In contrast, for $Re < 5$ our experiments show *negative* shear-induced lift coefficients. That the lift force on a fixed sphere (solid particle or bubble) embedded in a solid-body rotation flow is negative (i.e. centripetal) at low Reynolds number is in line with Gotoh's (1990) theoretical prediction which is the counterpart of Saffman's prediction for the flow configuration considered here. Further improvements of the experimental setup will allow us to achieve more precise measurements in this low-Re range. But note again that equation (2.1) is not necessarily a good approximation for that low Re regime: First, the history force has been omitted and second, the lift force parametrization is inappropriate for small Re.

What would be desirable is to reconstruct the *whole* bubble trajectory with the help of equation (2.1) and the values obtained for the lift and drag coefficients from our analysis of the equilibrium position. Right now, there is no way to achieve this. The accuracy in C_L and C_D is simply not sufficient and additional terms in (2.1) may also play a role. In addition, in a non-stationary situation the bubble's wake and hence the forces may differ from its steady structure. Presently, in the numerical simulations these small imperfections accumulate during the spiralling process towards the equilibrium which can take minutes. Therefore, only a *local* comparison of the bubble trajectories or a comparison between bubble trajectory *characters* gives satisfactory agreement between experiment and numerics.

References

[1] J. Ashmore, C. del Pino, and T. Mullin. Cavitation in a lubrication flow between a moving sphere and a boundary. *Phys. Rev. Lett.*, 94:124501, 2005.

[2] T.R. Auton. The lift force on a spherical body in a rotational flow. *J. Fluid Mech.*, 183:199–218, 1987.

[3] T.R. Auton, J.C.R. Hunt, and M. Prud'Homme. The force exterted on a body

in inviscid unsteady non-uniform rotational flow. *J. Fluid Mech.*, 197:241–257, 1988.

[4] P. Bagchi and S. Balachandar. Shear versus vortex-induced lift force on a rigid sphere at moderate re. *J. Fluid Mech.*, 473:379–388, 2002.

[5] J. J. Bluemink, E. A. van Nierop, S. Luther, N. G. Deen, J. Magnaudet, A. Prosperetti, and D. Lohse. Asymmetry-induced particle drift in a rotating flow. *Phys. Fluids*, 17:072106, 2005.

[6] R. Clift, J. R. Grace, and M. E. Weber. *Bubbles, drops and particles*. Academics Press, New York, 1978.

[7] E. Climent and J. Magnaudet. Modifications d'une couche de bulles de mélange verticale induites par la présence de bulles. *C. R. Acad. Sci. Paris*, 326:627–34, 1998.

[8] V. Galindo and G. Gerbeth. A note on the force on an accelerating spherical drop at low-renolds number. *Phys. Fluids*, A5:3290–3292, 1993.

[9] T. Gotoh. Brownian motion in a rotating flow. *J. Stat. Phys.*, 59:371–402, 1990.

[10] S. Guet, G. Ooms, R.V.A. Oliemans, and R.F. Mudde. Bubble size effect on low liquid input drift-flux parameters. *Chem. Eng. Sci.*, 59:3315–3329, 2004.

[11] I. Herron, S. Davis, and F. Bretherton. On the sedimentation of a sphere in a centrifuge. *J. Fluid Mech.*, 68:209–234, 1975.

[12] H. Lamb. *Hydrodynamics 6th edition*. Dover Publications, New York, 1886.

[13] D. Legendre and J. Magnaudet. The lift force on a spherical bubble in a viscous linear shear flow. *J. Fluid Mech.*, 368:81–126, 1998.

[14] D. Lohse and A. Prosperetti. Controlling bubbles. *J. Phys.: Condens. Matter*, 15:S415, 2003.

[15] J. Magnaudet and I. Eames. The motion of high-Reynolds number bubbles in inhomogeneous flows. *Ann. Rev. Fluid Mech.*, 32:659–708, 2000.

[16] J. Magnaudet and D. Legendre. Some aspects of the lift force on a spherical bubble. *Appl. Sci. Res.*, 58:441–461, 1998.

[17] T. Maxworthy, C. Gnann, M. Kürten, and F. Durst. Experiments on the rise of air bubbles in clean viscous liquids. *J. Fluid Mech.*, 321:421, 1996.

[18] I. Mazzitelli, D. Lohse, and F. Toschi. The effect of microbubbles on developed turbulence. *Phys. Fluids*, 15:L5–L8, 2003.

[19] I. Mazzitelli, D. Lohse, and F. Toschi. On the relevance of the lift force in bubbly turbulence. *J. Fluid Mech.*, 488:283–313, 2003.

[20] R. Mei, J.F. Klausner, and C.J. Lawrence. A note on the history force on a spherical bubble at finite reynolds number. *Phys. Fluids*, 6:418–420, 1994.

[21] M. A. Naciri. *Contribution à l'étude des forces exercées par un liquide sur une bulle de gaz: portance, masse ajoutée et interactions hydrodynamiques*. PhD thesis, L'Ecole Central de Lyon, 1992.

[22] J.M. Rensen, D. Bosman, J. Magnaudet, C.D. Ohl, A. Prosperetti, R. Tögel, M. Versluis, and D. Lohse. Spiraling bubbles: How acoustic and hydrodynamic forces compete. *Phys. Rev. Lett.*, 86:4819–4822, 2001.

[23] P. G. Saffman. The lift on a small sphere in a slow shear flow. *J. Fluid Mech.*, 22:385, Corrigendum: **31** p. 624 1968, 1965.

[24] J. R. T. Seddon and T. Mullin. Reverse rotation of a cylinder near a wall. *Phys. Fluids*, 18:041703, 2006.

[25] G. Sridhar and J. Katz. Drag and lift forces on microscopic bubbles entrained by a vortex. *Phys. Fluids.*, 7:389–399, 1995.

[26] G.I. Taylor. The forces on a body placed in a curved of converging stream of fluid. *Proc. R. Soc. Lond. A*, 120:260, 1928.

[27] R. Toegel, S. Luther, and D. Lohse. Viscosity destabilizes sonoluminescing bubbles. *Phys. Rev. Lett.*, 96:114301, 2006.

[28] A. Tomiyama. Transverse migration of single bubble in simple shear flows. *Chem. Eng. Sci.*, 57:1849–1858, 2002.

[29] G. Tryggvason, B. Bunner, A. Esmaelli, D. Juric, N. Al-Rawahi, W. Tauber, J. Han, S. Nas, and Y.-J. Jan. A front-tracking method for the computations of multiphase flow. *J. Comp. Phys.*, 169:708–759, 2001.

[30] S. Yang and L. Leal. A note on the memory-integral contributions to the force on an accelerating spherical drop at low reynolds number. *Phys. Fluids*, A3: 1822–1824, 1991.

Chapter 3

Particle rotation[‡]

It is known that, in a linear shear flow, *fluid inertia causes a particle to spin* more slowly *than the surrounding fluid. The experiments in this chapter, performed with a sphere with fixed center, but free to rotate in a fluid undergoing* solid-body rotation *around a horizontal axis, indicate that the spin rate of the sphere can be* larger *than that of the flow when the sphere is sufficiently far from the axis. Numerical simulations at Reynolds number* $5 \leq Re \leq 200$ *confirm this observation. To gain a better understanding of the phenomenon, the rotating flow is decomposed into two shear flows along orthogonal directions. It is found numerically that the cross-stream shear has a much stronger effect on the particle spin rate than the streamwise shear. The region of low stress at the back of the sphere is affected by the shear component of the incident flow. While for the streamwise case the shift is minor, it is significant for cross-stream shear. The results are interpreted on the basis of the effect of the shear flow components on the quasi-toroidal vortex attached in the sphere's near wake. The contributions of streamwise and cross-stream shear to the particle spin can be linearly superposed for* Re *= 20 and 50.*

3.1 Introduction

The behavior of particles or bubbles in a flow is one of the most fundamental problems of fluid mechanics. While a considerable body of knowledge exists in the limits of vanishing Reynolds numbers (see e.g. Happel and Brenner [26], Kim and Karrila [33], Lamb [36]) or inviscid flow (see e.g. Auton et al. [3], Lamb

---

[‡] J.J. Bluemink, D. Lohse, A. Prosperetti and L. van Wijngaarden, *A sphere in a uniformly rotating and shearing flow*, J. Fluid Mech. **600**, 201-233 (2008).

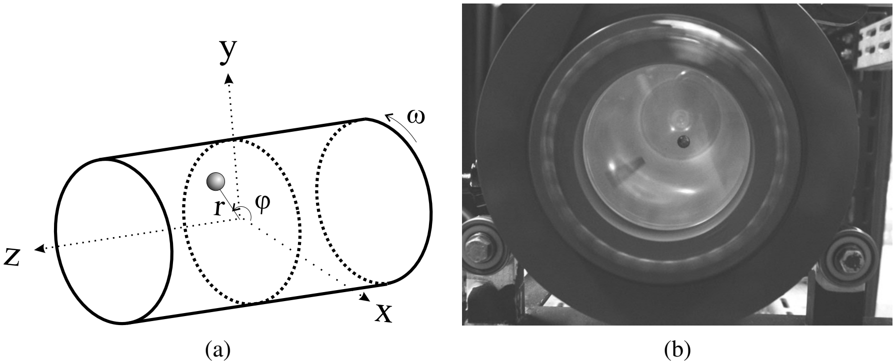

(a) (b)

Figure 3.1: Sphere in solid-body rotation: (a) geometry, gravity in y-direction, (b) a sphere (indicated by the arrow) in its equilibrium position in the small cylinder.

[36], Milne-Thompson [46]), the investigation of finite-Reynolds-number effects has been limited to simple situations such as steady uniform or shearing flows. Even for these relatively simple configurations, however, our understanding is far from complete.

The complexity of the general problem suggests that a profitable way to proceed is to consider a variety of flows with well-defined characteristics in the hope of building a broadly applicable synthesis. Rotational flows, which are studied in the present paper, are particularly interesting in view of their widespread occurrence. It appears impossible, for example, to achieve a satisfactory description of particle dispersion in turbulence, or of the behavior of fluidized beds, in the absence of a good understanding of the drag and lift forces in such flows.

Here we study the behavior of a sphere in a fluid undergoing solid-body rotation (see figure 3.1a). The center of the sphere is fixed while it is allowed to rotate in a torque-free state. Experimentally, the situation is realized by placing a buoyant sphere in a liquid-filled cylinder rotating around a horizontal axis (see figure 3.1b) and results up to Reynolds numbers $Re \simeq 800$ are shown, with

$$Re = \frac{2RU_0}{\nu}. \tag{3.1}$$

In this equation R is the sphere radius, U_0 the undisturbed flow velocity at the sphere center and ν the fluid viscosity. Numerically, we determine and explain the dependence of the particle spin rate and lift force on the Reynolds number Re up to 200 and study the effects of the individual streamwise and cross-stream components from which the motion of a fluid in solid-body rotation can be synthesized. We find that streamwise and cross-stream shear have very different effects on the particle spin. For solid-body rotation, the only other study we are aware of in which the particle is allowed to freely rotate at sizeable Reynolds number is Bagchi and Balachandar [5], whose results, however, are quite different from ours. In particular, their conclusion that the particle spin rate is never greater than that of the ambient fluid is at variance with our experiments and calculations and for the time being remains unexplained.

Earlier work on rotating flows includes Herron, Davis, and Bretherton [28] and Gotoh [25] who calculated the hydrodynamic force acting on a sphere immersed in a rotating flow at low Reynolds number. The lift force in a rotational inviscid flow – in which, of course, the flow does not induce any rotation of the sphere – has been investigated in Lighthill [39], Auton [2], Auton et al. [3] (see also Drew and Lahey [22]). For the case of bubbles, Naciri [49] and Sridhar and Katz [58] studied experimentally situations similar to the one considered here and measured a lift coefficient considerably larger than that predicted by the available theories. Similar results have more recently been reported in van Nierop et al. [64]. As discussed in that paper, in the low Reynolds number limit, the hydrodynamic force appears to be very sensitive to the flow type.

Several authors have studied the trajectory of particles in fluids in solid-body rotation. Experimental results have been reported by, for example, Roberts, Kornfeld, and Fowlis [55] and Mullin et al. [48]. Annamalai and Cole [1], Raju and Meiburg [54], Gao, Ayyaswamy, and Ducheyne [23] and Coimbra and Kobayashi [16] have studied the problem theoretically, and an analysis of the stable equilibrium points at low Reynolds number has been given by Paradisi and Tampieri [52], Coimbra and Kobayashi [16] and Kobayashi and Coimbra [34]. A brief study of the equivalent problem for bubbles was presented by Lohse and Prosperetti [41].

Our focus is on the particle spin and, therefore, quite different from that of all these authors. Furthermore, most of the previously cited theoretical papers treated the particles as points using parameterizations of the hydrodynamic force while we actually calculate it from first principles by solving the Navier-Stokes equations.

Two other classes of flows involving particle spin or fluid rotation have been studied. In one of them, the particle translates in the direction of the rotational axis of the fluid (Candelier et al. [12, 13], Childress [14], Kim and Choi [32], Wang et al. [65], Weisenborn [67]). In another group of papers (Barkla and Auchterlonie [8], Dennis et al. [21], Oesterlé and Dinh [51], Rubinow and Keller [56]) the particle spins about an axis perpendicular to the incident flow, as in the present work, but the particle angular velocity is prescribed rather than resulting from the fluid dynamic interaction as here. Generally speaking, all these papers find a strong effect of particle spin on the hydrodynamic force, and especially on the lift. However these situations are evidently different from the one considered in this paper.

Solid-body rotation can be decomposed into two shearing flows along orthogonal directions. It is therefore of interest to consider such flows. The flow field in a unidirectional simple shear is given by

$$\boldsymbol{U}(y) = 2\omega y \hat{\mathbf{e}}_x, \tag{3.2}$$

where **U** is the undisturbed fluid velocity and 2ω is the shear rate. If no external torque acts on the particle, its angular velocity Ω_p will eventually adjust so as to result in a vanishing hydrodynamic torque. Lin, Peery, and Schowalter [40] studied this situation for very low values of the Taylor number defined by

$$Ta = \frac{2R^2\omega}{\nu}. \tag{3.3}$$

This quantity may be considered as the ratio of the characteristic time for rotation to that for viscous diffusion and is used later as a dimensionless measure of the liquid angular velocity. The spin rate calculated by Lin et al. [40] is

$$\frac{\Omega_p}{\omega} = 1 - 0.3076\, Ta^{3/2} + o(Ta^{3/2}). \tag{3.4}$$

Poe and Acrivos [53] found experimentally that this expression is adequate provided $Ta < 0.1$. Mikulencak and Morris [45] investigated the same situation numerically for $0 < Ta < 100$. For $Ta > 1$ a steep decrease in the spin rate was seen with the Taylor number. Thus, the particle angular velocity decreases as the fluid inertial effects, as measured by the Taylor number, increase. Note that any difference between the particle and fluid rotation rates must be due to fluid inertia, which is of course an immediate consequence of Faxèn's second theorem which states that, at vanishing Reynolds number, the angular velocity Ω_p of a torque-free sphere is the same as the local angular velocity of the ambient fluid (see e.g. Happel and Brenner [26], Kim and Karrila [33]).

The case in which the flow incident on the particle consists of the superposition of a uniform plus a streamwise shearing flow

$$\boldsymbol{U}(y) = (\omega y - U_0)\hat{\mathbf{e}}_x, \tag{3.5}$$

where U_0 represents the uniform flow component, has been studied by, among others, Saffman [57] and McLaughlin [43] for small Reynolds numbers. Saffman [57] finds that the sphere angular velocity is not affected by the shear component to lowest order. At higher Reynolds number the numerical results of Bagchi and Balachandar [5] can be fitted by

$$\frac{\Omega_p}{\omega} = \frac{1}{2}\left(1 - 0.0364 Re^{0.95}\right) \tag{3.6}$$

for $0.5 < Re \leq 5$ and

$$\frac{\Omega_p}{\omega} = \frac{1}{2}\left(1 - 0.0755 Re^{0.455}\right) \tag{3.7}$$

for $5 \leq Re \leq 200$. Again, the particle spin rate is seen to decrease as fluid inertia increases.

In addition to the already mentioned papers by Saffman [57] and McLaughlin [43], several other authors have studied the forces on particles in linear shear flows. Dandy and Dwyer [17] calculated the force on a non-rotating particle while Bagchi and Balachandar [5] allowed the particle to rotate freely as was seen in (3.6) and (3.7). At low Reynolds number, as indicated by Mei [44], the spin rate has little effect on the lift force. This is not the case for Reynolds numbers in the intermediate range as shown e.g. by Kurose and Komori [35], who studied a particle with a prescribed spin rate.

In this paper we study the steady-state spin rate of torque-free particles immersed in a class of flows ranging from unidirectional shear to solid-body rotation. For the latter case, we present both experimental and numerical results, while only numerical means are used for the other cases. Unexpectedly, the spin rate of a spherical particle trapped in a liquid rotating in solid body motion is found to exceed the angular velocity of the liquid in a large part of the parameter range. The only other reports of spheres rotating faster than the fluid are in turbulent flows (see e.g. Mortensen et al. [47], Ye and Rocco [69]). These data however were acquired in many-particle systems and it was the mean spin that exceeded the mean angular fluid velocity. Mortensen et al. [47] ascribe this to preferential particle concentration. A somewhat surprising new result in this work is that the effects of the cross-stream shear and the streamwise shear on particle spin rate and shear stress at the particle surface can be linearly superposed for the Reynolds number range studied.

3.2 Preliminaries

In suitable parameter ranges, a buoyant spherical particle or bubble finds an equilibrium position when inserted in a fluid-filled horizontal cylinder rotating with constant angular velocity ω as in figure 3.1a (see e.g. Bluemink et al. [9], Coimbra and Kobayashi [16], Lohse and Prosperetti [41], Naciri [49], Paradisi and Tampieri [52], van Nierop et al. [64]). At this position all forces – buoyancy, drag, added mass, pressure gradient and lift – balance. While its center remains fixed, the particle is of course free to rotate.

In addition to the particle radius, R, and density, ρ_p, the equilibrium position of the particle in a rotating liquid depends on ω, the angular velocity of the fluid,

ν and ρ, the kinematic viscosity and density of the liquid, and g, the acceleration due to gravity. Two dimensionless quantities can be formed then, in addition to the Taylor number defined in (3.3). We take

$$Ga = \frac{2R\sqrt{2R(1-\rho_p/\rho)g}}{\nu}, \qquad \frac{\rho_p}{\rho}. \tag{3.8}$$

The Galilei number Ga is a Reynolds number based on the characteristic velocity induced by gravity; its use is particularly convenient as, for a given liquid and particle radius, it is a constant.

More standard dimensionless parameters, such as the Reynolds number, can be added to the above mentioned ones to characterize the flow environment seen by the particle. Although a dependent variable, the distance r_e of the equilibrium position from the axis of rotation is important for this purpose. With $U_0 = \omega r_e$ the Reynolds number defined earlier in (3.1) becomes

$$Re = \frac{2RU_0}{\nu} = \frac{2Rr_e\omega}{\nu}. \tag{3.9}$$

We also introduce a vorticity parameter

$$Sr_\omega = \frac{2\omega R}{U_0} = \frac{2R}{r_e}. \tag{3.10}$$

Lohse and Prosperetti [41] presented a simplified analysis of the problem using standard large-Reynolds-number expressions for the added mass and lift forces on a bubble (see 3.14). After adjusting for the particle density and the no-slip boundary conditions at the interface, that analysis is also applicable to a solid sphere and gives the following result for r_e

$$\frac{r_e}{2R} = \frac{2\sqrt{2}}{3}\left[\sqrt{\left(\frac{K}{C_D}\right)^4 + \left(\frac{3}{8C_D}\right)^2\left(\frac{Ga}{Ta}\right)^4} - \left(\frac{K}{C_D}\right)^2\right]^{1/2}, \tag{3.11}$$

in which C_D is the drag coefficient and $K = 2C_L - 1 - C_A$ is composed of the added mass coefficient C_A, equal to 1/2 in potential flow, and of the lift coefficient C_L, equal to 1/2 in inviscid flow (Auton [2]). Clearly, as $Ta \to \infty$, we have $r_e \to 0$, i.e. the particle moves towards the axis of rotation. If we approximate C_D by a constant, which is a rough estimate appropriate in the upper range of the Reynolds numbers encountered in the experiments described in the next section, for small values of Ta (3.11) gives

$$Re = \frac{r_e}{R}Ta = 2\frac{Ta}{Sr_\omega} \simeq \frac{2Ga}{\sqrt{3C_D}}\left[1 - \frac{4}{3C_D}\left(\frac{KTa}{Ga}\right)^2\right]. \tag{3.12}$$

This estimate shows that, asymptotically, Sr_ω increases proportionally to Ta (i.e. to ω), while the Reynolds number reaches the limiting value $2Ga/\sqrt{3C_D}$, which is readily seen to coincide with the terminal velocity of the particle in still fluid, as expected. Before this limit is reached, however, Re increases as the Taylor number decreases.

3.3 Experiment

Experiments were conducted by placing a low-density polyethylene spherical particle (density ρ_p = 920 kg m^{-3}) in a transparent liquid-filled cylinder rotating around a horizontal axis. Most of the data were taken in a 0.1 m diameter glass cylinder (see figure 3.1b) but, in order to rule out wall effects, we also took some data in a larger, 0.5 m diameter Perspex cylinder; both cylinders were 0.5 m long. The larger cylinder had a motor with a controlled feed-back loop which permitted setting the angular velocity with great accuracy.

Particles with radii R = 3.1 and 4.0 mm were used in the experiment. They were marked with paint so as to facilitate the measurement of their angular velocity from image sequences taken at a speed of 50 f.p.s. Several readings of the angular velocity of the particles and of the small cylinder were taken from each image sequence; the error bars shown in figures 3.3–3.5 represent the range of the data.

The liquids were water and a mixture of water and 75% glycerine by weight; the dynamic viscosity of the mixture was measured with a viscometer to be μ = 0.0347 kg m^{-1} s^{-1} and the density 1180 kg m^{-3}.

To be certain that the flow field as seen by the particle is solid-body rotation, sufficient time for spin-up must be allowed. In figure 3.2 the velocity profiles for different spin-up times for a cylinder with radius a and height h, according to Wedemeyer [66], are shown. In the figure v_0 indicates the velocity of the fluid and it is normalized by the velocity at the cylinder wall. The time t allowed for spin-up is written in non-dimensional form as $k\omega t$, where ω is the cylinder angular velocity and $k = 0.443\ (2a)/h\sqrt{\nu/(a^2\omega)}$. For $k\omega t$ = 0.5 the fluid in the cylinder is far from solid-body rotation, whereas for $k\omega t$ = 3 it is quite close. The lines in the figure are valid when the viscous terms are negligible, i.e. when $ka^2\omega/\nu \gg 1$. The value of $ka^2\omega/\nu$ is indeed much larger than 1, so the above estimate is valid. For a maximum error of 1% in velocity compared to the velocity field for solid-body rotation, the spin-up time t_s for a fluid in a rotating cylinder starting from rest can be estimated to be of the order of (see e.g. Wedemeyer [66])

$$t_s = \frac{10.3954}{\omega}\sqrt{\frac{a^2\omega}{\nu}}\frac{h}{2a}. \tag{3.13}$$

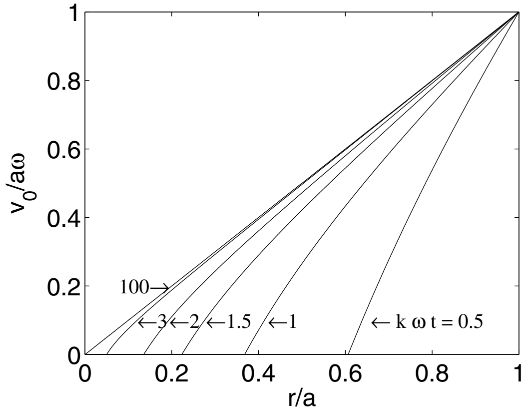

Figure 3.2: Velocity profiles for different spin-up times.

For the liquids used in this experiment, this relation gives estimates of a maximum spin-up time of 4 min in water and 6 min in the glycerin–water mixture for both cylinders. Data were taken well past these waiting periods. Furthermore, in several cases, two sets of data were taken an hour or so apart, letting the cylinder rotate in the intervening time; no differences (beyond the usual experimental fluctuations) were found.

For experiments performed in water, the Reynolds numbers were between 200 and 1000. Most of these experiments are well above the critical Reynolds number at which the flow past a rising sphere loses axial symmetry (Jenny, Dusek, and Bouchet [30], Natarajan and Acrivos [50]). Unlike the glycerin case, where the particle center remains stationary, in the water experiments we observed the particles precessing around their equilibrium position, which is probably a manifestation of a related instability. The spin rate reported was measured for this precessing particle.

The diamonds in figure 3.3 show the measured particle angular velocity Ω_p normalized by the cylinder angular velocity ω as a function of Ta. The filled symbols are data taken with the 4 mm radius sphere, while the open symbols refer to the 3.1 mm radius sphere. The difference between the two sets illustrates the effect of the parameter Ga defined in (3.8). These data clearly indicate that there is a broad range of Ta values for which the particle rotates faster than the cylinder, i.e. faster than the undisturbed flow. This is surprising, since, as we have seen in § 3.1, the known results for streamwise shear would suggest that an increase of inertial effects brings about a decrease in the particle spin rate compared to the ambient rotation. Moreover, to the best of our knowledge, hitherto no such results

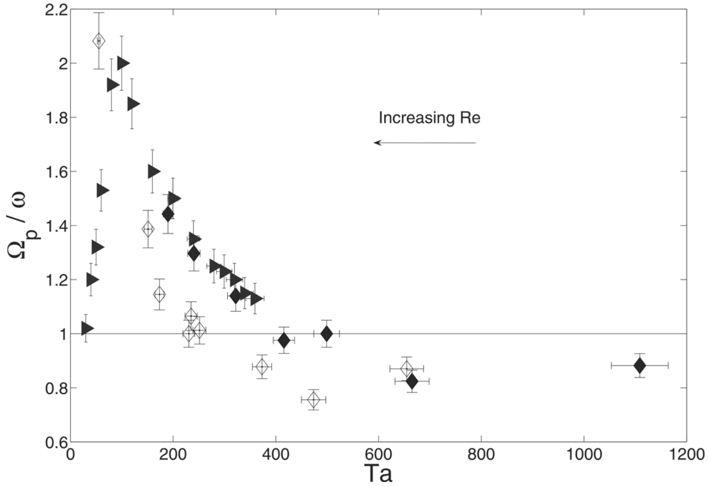

Figure 3.3: Particle spin rate Ω_p normalized by the liquid angular velocity ω versus $Ta = 2\omega R^2/\nu$ for the experiments in water. The diamonds are data from the smaller cylinder, triangles from the larger cylinder. The filled and open symbols are for particles of radius 4.0 mm and 3.1 mm, respectively. The particle Reynolds number corresponding to these data is in the range of 200 to 1000.

have been reported.

As the cylinder rotation rate is decreased, the particle equilibrium position moves away from the axis in such a way that Re increases as predicted by (3.11) and (3.12). As shown in figure 3.3, the normalized particle angular velocity increases as well. To examine the possibility of wall effects, we took data in the same Taylor-number range in the larger cylinder. These data, shown by the triangles in figure 3.3, are quite consistent with the other ones, which proves that the observed results are not wall effects. The maximum value of Ω_p/ω, about 2.1, is reached for a Reynolds number that can be estimated as 650 ± 100. It should be noted that this is smaller than the Reynolds number for the terminal velocity in still fluid which would be 709 and 1090 for the 3.1 and 4.0 mm spheres, respectively. As the Taylor number is further decreased, Ω_p/ω rapidly falls and the precession of the particle is less regular. It is speculated below in § 3.9 that these features may have some analogy with the onset of unsteadiness in the case of a sphere rising in a quiescent fluid as the Reynolds number is increased.

When the Taylor number is increased beyond 400 or so, the particle moves closer to the center, the Reynolds number decreases, and the vorticity parameter Sr_ω increases. Correspondingly, Ω_p/ω falls below 1, reaches a minimum, and then starts rising again toward 1, which is the expected normalized spin rate at very

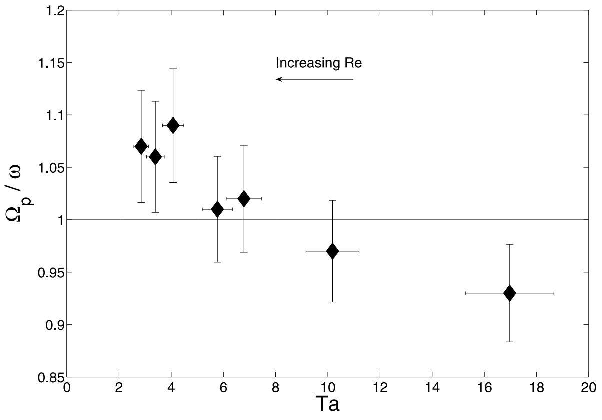

Figure 3.4: Normalized particle spin rate Ω_p/ω versus $Ta = 2\omega R^2/\nu$ for the glycerine–water mixture in the smaller cylinder; the particle radius was 4.0 mm. The corresponding Reynolds number is between 2 and 50, approximately.

large angular velocities when the particle center is essentially on the rotation axis.

For the data in figure 3.3 Sr_ω ranges between about 0.1 and 0.3 to the left of the peak and between about 0.3 and 1 in the descending part of the curve. These values are not very accurate due to the difficulty of getting an accurate reading of r_e, but they do nevertheless demonstrate the trend of the data.

Figure 3.4 shows the results obtained in the smaller cylinder with the glycerine–water mixture. The resulting Reynolds numbers were an order of magnitude smaller than with water but the effect, although reduced, is still present: as Ta decreases, the particle moves away from the axis and its normalized spin rate increases above 1. This finding suggests that the precessional motion of the sphere observed in water does not qualitatively affect the phenomenon. The diamonds in figure 3.5 show the same data plotted versus the Reynolds number. As before, a precise measurement of the equilibrium position r_e is difficult and the error bars accordingly rather large; nevertheless, the normalized particle spin rate is greater than 1 at sufficiently low rotation rates. At higher rotation rates the particle moves closer to the axis, the vorticity parameter Sr_ω increases, and Ω_p/ω falls below 1 as before. The fact that this transition from values larger than 1 to values smaller than 1 is observed for very different Reynolds numbers suggests it is mainly dependent on Sr_ω reaching a sufficiently large value, which is comparable in the two cases of water and water–glycerine.

In summary, these experiments conclusively prove that, in a portion of the

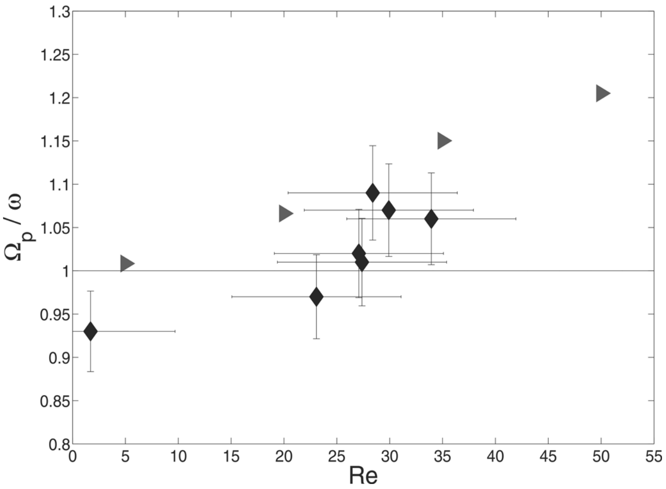

Figure 3.5: The same data for the normalized particle spin rate of figure 3.4 (diamonds) are plotted versus Re. The triangles are numerical results discussed in § 4.1.

parameter range (Re, Sr_ω), the normalized angular velocity of a particle increases beyond 1 with distance from the axis, i.e. as the flow velocity seen by the particle, and thus Re, becomes sufficiently large. This trend prevails up to $Re \sim 650$, after which the normalized particle spin rate rapidly decreases. Thus, except when the particle is very close to or very far from the cylinder axis, the particle angular velocity is higher than that of the undisturbed flow.

3.4 Numerical method

To better understand the behavior of the particle angular velocity in solid-body rotation compared to simple shearing flow we carried out numerical simulations with different types of flow, described in the next section. In this section we briefly explain our numerical method.

We used the three-dimensional Navier-Stokes solver Physalis (Zhang and Prosperetti [70]). The underlying method rests on the observation that, owing to the no-slip condition, the flow in the immediate neighborhood of a particle differs at most slightly from a rigid-body motion and can therefore be linearized about such a motion. The resulting set of equations is formally similar to the Stokes equations, for which a general solution (valid only very near the particle) can be written down in terms of an expansion in spherical harmonics with undetermined coefficients (Happel and Brenner [26], Kim and Karrila [33]). These coefficients are calculated iteratively by matching, in the immediate neighborhood of the particle, the analytic solution obtained in this fashion to a finite-difference solution. The advantage of this procedure is that it avoids the need to deal with the complex geometry of the actual particle boundary. The finite-difference solution is obtained on a standard Cartesian grid by a second-order projection method. The solution obtained has therefore a dual nature, spectral in a region with a thickness of the order of the mesh size surrounding the particle, and finite-difference further away. Useful features of the technique are that fewer nodes per particle radius are sufficient for an accurate solution and that the no-slip condition at the particle surface is satisfied exactly. Furthermore, the low-order expansion coefficients are directly proportional to the hydrodynamic force and couple acting on the particle. This property eliminates the need to calculate these quantities by integration of the fluid stress over the particle surface. For details about this method the reader is referred to Zhang and Prosperetti [70] and for applications to Zhang, Botto, and Prosperetti [71].

For reasons of computational time, most of the simulations were conducted for $Re = 20$ and $Re = 50$, and a few additional ones were carried out for $Re = 5$, 35, 100 and 200. Decreasing the Reynolds number below 5 would require a very large computational domain to avoid boundary effects, while higher Reynolds numbers require a more refined grid. We found that in the Reynolds number range between 5 and 50 it was possible to perform simulations with sufficient domain size and resolution in a reasonable amount of computing time.

The particle center was placed at the center of the computational domain which was a cuboid (see figure 3.6 for a cross-section of the domain). Unless stated otherwise, its dimensions were 20 particle radii in the x- and y-directions and at least 16 in the z-direction, parallel to the axis of rotation. For $Re = 20$, we found that doubling the domain size changed the particle spin rate by no more than 0.4%, the drag coefficient by about 1% and the lift coefficient (defined below in (3.14)) by about 3%. For Re = 5 increasing the domain size from 18 to 22 particle radii in each direction changed the drag coefficient by 1.4%, while the (much smaller) lift coefficient underwent a change of over 30%. Thus, although the results for Re = 5 may have a somewhat lower accuracy, we conclude that our domain size was sufficient for the other cases.

It has been shown in Zhang and Prosperetti [70] that, for a sphere in uniform flow, 8 nodes per particle radius give an excellent accuracy at Re = 50 and an acceptable one even at Re = 100. We have used the same number of nodes up to Re = 50. To test the resolution, for $Re = 50$ we refined the grid by a factor of 2 in each direction and found that the spin rate and the drag and lift coefficients changed by about 1% in the case of solid-body rotation. For a linear shear flow the absolute differences were comparable but, since in this type of flow the lift

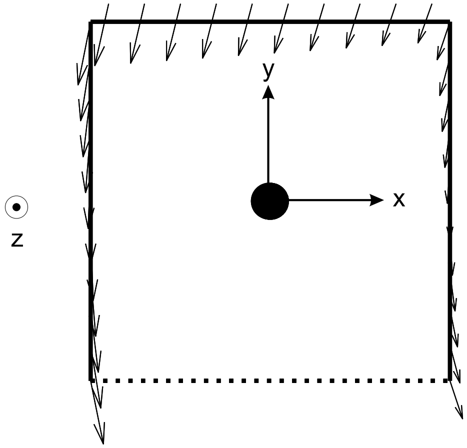

Figure 3.6: Cross-section of the computational domain. The boundaries where Dirichlet boundary conditions are applied are solid, the boundary where von Neumann boundary conditions are applied is dotted.

coefficient and spin rate are much smaller, the relative differences were up to 8% for the particle spin rates and up to 13% for the lift force, while they remained at the 1% level for the drag coefficient. Changing the resolution for the cross-stream shear and straining flow yielded differences below the ones of the linear shear flow. For the simulations where $Re > 50$, 16 nodes per particle radius were used.

The accuracy of the spectral representation of the solution in the region near the particle depends on the order N of truncation of the spherical harmonic expansion, i.e. on the number of coefficients retained in the calculation (Zhang and Prosperetti [70]). It was found that N = 1, which amounts to retaining only 10 coefficients, yields inaccurate results. For Re = 50, truncation at N = 2 (25 coefficients) or N = 3 (49 coefficients) gave a difference of 2% in the particle spin rate, 1% in the lift coefficient, and 0.2% in the drag coefficient. Therefore, the calculations were done with N = 2 and 25 coefficients.

The undisturbed flow velocity was prescribed on all the faces of the computational domain parallel to the rotation axis except the bottom one (figure 3.6). On the bottom surface the derivative of the horizontal velocity was set equal to the corresponding derivative of the undisturbed velocity (i.e. $-\alpha\omega$, see (3.15)), while the normal derivative of the normal velocity was set to zero. Periodicity conditions were imposed on the bounding planes normal to the rotation axis (z-direction). For the auxiliary pressure variable, the standard von Neumann conditions of the second-order projection method (see for example Brown, Cortez, and Minion [10], Zhang and Prosperetti [70]) were used.

3.5 Numerical results for solid-body rotation, varying Re

A first set of simulations was conducted for a particle immersed in a liquid in solid-body rotation with prescribed values of Re and Sr_ω. In this case, as in the other simulations described later, the particle center was kept fixed but the particle was allowed to freely rotate.

Although it would have been desirable to conduct a simulation releasing the particle and allowing it to find its equilibrium position, the huge amount of computational time required prevented us from doing this. Thus, the particle was placed to the left of, and at different distances from, the rotation axis (figure 3.7a), depending on the desired shear rate. In principle, for a given Reynolds number and shear rate, (3.11) can be solved to give a specific value of Ga/Ta, which suggests that the situations we simulate are physically realizable.

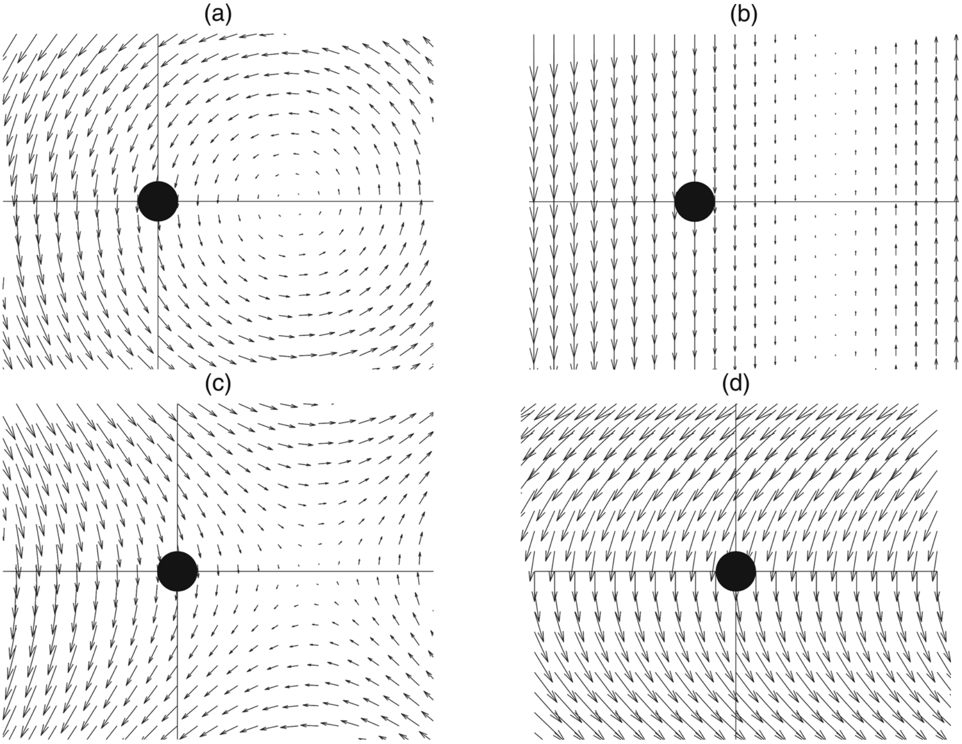

Figure 3.7: Examples of the flow fields of the family of flows (3.15): (a) solid-body rotation, α = 1, β = 1; (b) linear shear, α = 0, β = 1; (c) strain, α = -1, β = 1; (d) cross-stream shear, α = 1, β = 0.

The symbols in figure 3.8 show the drag on the sphere for different Reynolds

Drag coefficient	Re = 5	Re = 20	Re = 50
Dennis and Walker [20], uniform flow	7.21	2.73	
Standard drag curve (Clift et al. [15])	6.98	2.61	1.54
Magnaudet et al. [42]	6.92	2.71	
Bagchi [4]			1.57
Present, uniform flow	7.42	2.77	1.59
Present, non-rotating particle in solid-body rotation, Sr_ω = 0.1		2.79	1.62
Present, rotating particle in solid-body rotation, Sr_ω = 0.1	7.83	2.80	1.63
Present, rotating particle in solid-body rotation, Sr_ω = 0.04			1.59

Table 3.1: Drag coefficient, comparison of present simulations with previous results.

numbers for both rotating and non-rotating particles. The differences in the drag coefficient are so small that they are not visible here. The solid line is the standard drag curve for uniform flow, which predicts a slightly smaller drag. Numerical values are given in table 3.1 together with those of other authors and our own for uniform flow.

The results for the normalized spin rate Ω_p/ω vs. the Reynolds number are shown in figures 3.5 and 3.9. Some numerical values are given in table 3.2. All our numerical results indicate that the normalized spin rate Ω_p/ω is above 1 in the case of a fluid in solid-body rotation. Thus the particle spins faster than the surrounding fluid, just as previously seen in experiments. As mentioned before, this behavior is at variance with that reported in the simulations of Bagchi and Balachandar [5] who, as indicated in table 3.2, found a decrease in the spin rate at these Reynolds numbers. For comparison with another flow situation, table 3.2 also shows results for a linear shear flow. For this case the results of Bagchi and Balachandar [6] and our own agree.

The triangles in figure 3.5 are the normalized spin rates for some of these simulations, all with Sr_ω = 0.1. In this figure the numerical results are compared with some of the experimental results (diamonds). The influence of Sr_ω can be deduced from table 3.2. If $Sr_\omega << 1$, there is little influence of Sr_ω on Ω_p/ω as becomes evident by comparing simulations at different Sr_ω, but at the same Reynolds number. For example, decreasing Sr_ω by a factor of 1000 at Re = 20 has hardly any effect on the ratio Ω_p/ω. This indicates that the ratio Ω_p/ω is much more sensitive to Re than to Sr_ω for $Sr_\omega << 1$. However, for high values of Sr_ω the particle

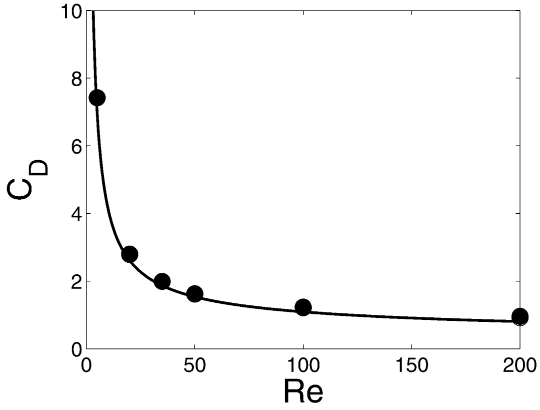

Figure 3.8: Drag coefficient for a particle in solid-body rotation, $Sr_\omega = 0.1$ (symbols), compared with the standard drag curve $C_D = (24/Re)(1+0.15Re^{0.687})$ for a uniform flow. The data points for $Re = 100$ and $Re = 200$ were calculated with doubled spatial resolution, but a smaller domain.

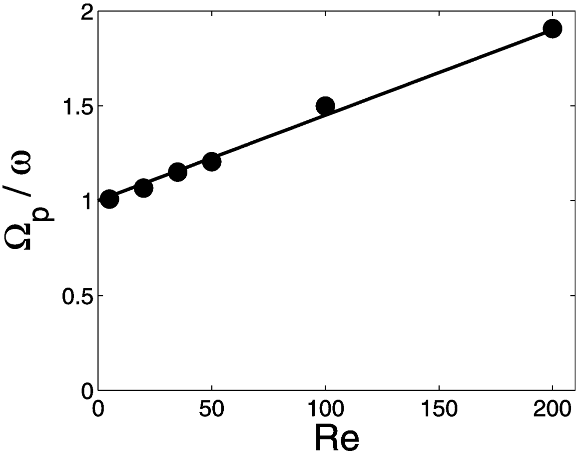

Figure 3.9: Normalized torque-free particle spin rate for a particle in solid-body rotation, $Sr_\omega = 0.1$, as a function of the Reynolds number. The data points for $Re = 100$ and $Re = 200$ were calculated with doubled spatial resolution, but a smaller domain. The solid line is a fit to the data: Ω_p/ω = 1 + 0.0045 Re.

Flow type	Re	Ω_p/ω, BB	Ω_p/ω, present results
Linear shear	20	0.35 ($Sr = 0.1$)	0.36 ($Sr = 0.05$)
Linear shear	50	0.28 ($Sr = 0.1$)	0.30 ($Sr = 0.05$)
Solid-body rotation	20		1.08 ($Sr_\omega = 1.10^{-4}$) 1.07 ($Sr_\omega = 0.1$)
Solid-body rotation	25	0.85 ($Sr_\omega = 0.04$)	1.10 ($Sr_\omega = 0.04$)
Solid-body rotation	50	0.74 ($Sr_\omega = 0.04$)	1.25 ($Sr_\omega = 0.04$) 1.24 ($Sr_\omega = 0.1$)

Table 3.2: Normalized torque-free particle spin rates, results of Bagchi & Balachandar (BB) compared with the present results.

position is near the axis, which has a strong effect on Ω_p/ω owing to the resulting strong inhomogeneity of the flow incident on the particle (see also the end of the section). The experimental data (diamonds) in figure 3.5 have in general a much higher shear rate than the numerical simulations, in particular the left-hand data points.

The triangle corresponding to Re = 5 in figure 3.5 shows an angular velocity close to the Stokes limit. The spin rate increases with Re, the behavior being comparable to that seen in the experimental data in the same figure. Figures 3.10 and 3.11 show the velocity field in the symmetry plane in the neighborhood of the particle for Re = 20 and 50, respectively. At the higher Reynolds number (figure 3.11) the wake extends to a much greater distance behind the particle but is less deflected. Also, velocities in the near-wake region are larger in the latter case.

Auton [2] expressed the force $\boldsymbol{F}_L$ on a stationary particle immersed in an inviscid rotational flow with undisturbed velocity $\boldsymbol{U}$ at the position of the particle center in the form

$$\boldsymbol{F}_L = \frac{4}{3}\pi R^3 \rho C_L \boldsymbol{U} \times (\nabla \times \boldsymbol{U}), \tag{3.14}$$

and calculated the value of the lift coefficient C_L as 1/2. As expected, owing to viscous effects and particle spin, our results, shown in table 3.3, differ from this value. The table also shows significant differences between our computations and those of Bagchi and Balachandar [5] for the present case of solid-body rotation, while the two calculations agree for linear shear.

Not unexpectedly, particle spin is found to have a much greater effect on the lift than on the drag coefficient. For example, for a non-rotating sphere at $Re =$ 20, C_L = 0.45 and C_D = 2.79 while, when the particle is allowed to rotate, C_D increases only slightly to 2.80, while C_L grows by over 40% to 0.65. These and other numerical values for Re = 50 and Sr_ω = 0.1 are given in table 3.3 and are

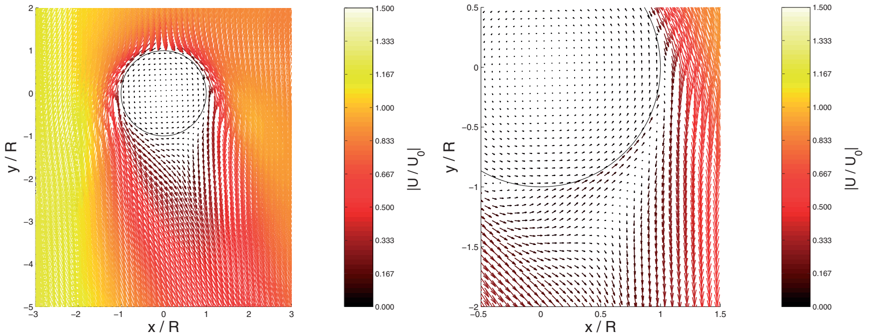

Figure 3.10: Computed velocity field in the symmetry plane for the flow around a sphere immersed in a liquid in solid-body rotation ($\alpha = 1$, $\beta = 1$, $Sr_\omega = 0.1$), $Re = 20$ (left), and a higher-resolution close up (right). The length of the arrows, which are color-coded, is proportional to the velocity. The flow parameters α and β will be explained in § 3.6.

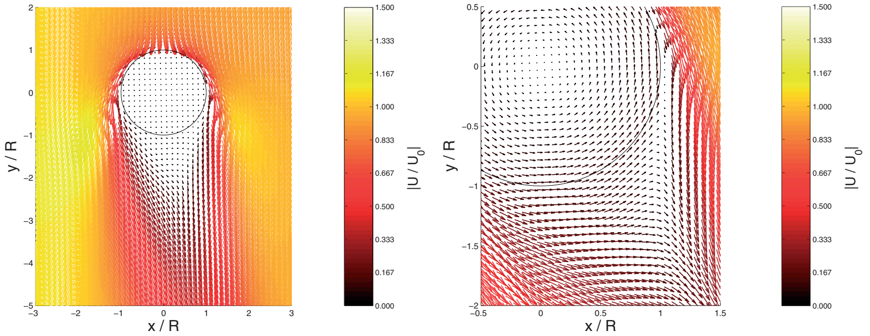

Figure 3.11: As figure 3.10 but for $Re = 50$.

shown for C_L graphically in figure 3.12 by the filled (rotating) and open (non-rotating) symbols. In both cases the lift coefficient increases with the Reynolds number. The difference between the rotating and non-rotating cases increases with Re as well. This is in line with the fact that the particle rotates faster at higher Re. The lift coefficient must go to zero as $Re \to 0$ and the computed result for $Re = 5$ does indeed indicate a strong decrease in C_L.

For Sr_ω of order 1 the normalized particle spin rate drops below 1. For $Sr_\omega = 2$, for which the axis of rotation touches the particle surface, a normalized particle spin rate of 0.93 was found on a domain of 10 particle radii in each direction. This situation is comparable to that in experiments where the particle finds its equi-

Flow type	Re	C_L, BB	C_L, present results
Linear shear, R	20	0.18 ($Sr = 0.1$)	0.19 ($Sr = 0.05$)
Linear shear, NR	20	0.04 ($Sr = 0.1$)	0.05 ($Sr = 0.05$)
Linear shear, R	50	0.11 ($Sr = 0.1$)	0.13 ($Sr = 0.05$)
Solid-body rotation, R	20		0.66 ($Sr_\omega = 10^{-4}$) 0.65 ($Sr_\omega = 0.1$)
Solid-body rotation, NR	20		0.45 ($Sr_\omega = 0.1$)
Solid-body rotation, R	25	4.29 ($Sr_\omega = 0.04$)	0.71 ($Sr_\omega = 0.04$)
Solid-body rotation, NR	25	4.14 ($Sr_\omega = 0.04$)	
Solid-body rotation, R	50	3.05 ($Sr_\omega = 0.04$)	0.90 ($Sr_\omega = 0.04$) 0.86 ($Sr_\omega = 0.1$)
Solid-body rotation, NR	50		0.64 ($Sr_\omega = 0.1$)

Table 3.3: Comparison of the results for the lift coefficient (defined in (3.14)) of Bagchi & Balachandar (BB) and the present results for rotating (R) and non-rotating (NR) spheres.

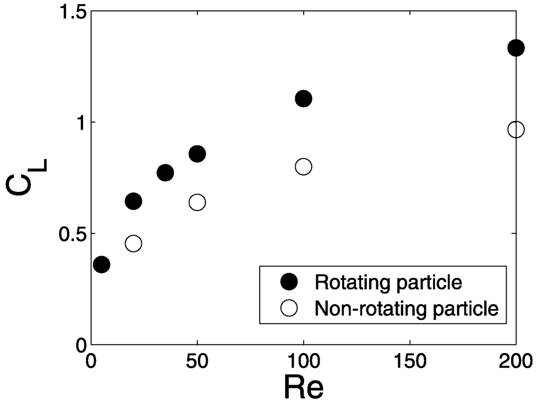

Figure 3.12: Dependence of the calculated lift coefficient defined in (3.14) on the Reynolds number ($Sr_\omega = 0.1$). The data points for $Re = 100$ and $Re = 200$ were calculated with doubled spatial resolution, but a smaller domain.

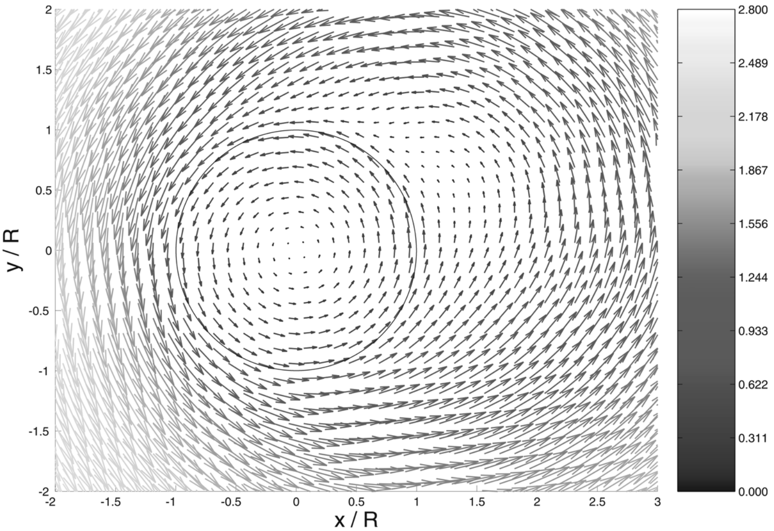

Figure 3.13: Velocity field in the symmetry plane for the flow around a sphere immersed in a liquid in solid-body rotation for a large vorticity parameter case, Sr_ω = 2, $Re = 20$. The axis of rotation is located at (x/R, y/R) = (1,0) and therefore touches the surface of the sphere.

librium close to the cylinder center. Here a low particle spin rate was found too. Figure 3.13 shows the flow around the particle for this high value of the vorticity parameter Sr_ω. The flow near the axis of rotation, located at (x/R, y/R) = (1,0), is strongly disturbed, with a drastic effect on the incident flow.

3.6 A family of flows

A solid-body rotation can be considered as the result of adding two two-dimensional shear flows in orthogonal directions (figure 3.14). As we have seen in § 3.2, when only a streamwise shear is present, the spin rate of the particle is smaller than that of the fluid, provided inertia is relevant. In contrast, at least in some parameter range, the opposite is true when both shear components are present, as found in our experiments and simulations of particles in rotating flows. To better understand the nature of these differences in behavior, we consider the following family of flows which smoothly interpolates between simple shear and solid-body rotation

$$\boldsymbol{U}(x, y) = -\alpha\omega y\hat{\mathbf{e}}_x + (\beta\omega x - U_0)\hat{\mathbf{e}}_y. \tag{3.15}$$

(For a study of the kinematics of these flows see Kobayashi and Coimbra [34].) The term $-U_0$ ($U_0 > 0$) represents a uniform flow, while α and β set the magnitude of

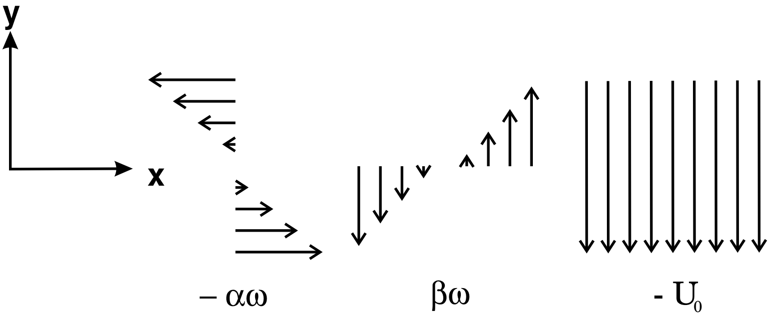

Figure 3.14: The three base flows constituting the family of flows described in § 3.6 and studied in § 3.7.

the cross-stream and streamwise shear components, respectively (figure 3.14). The vorticity and the shear rate s of this flow field are given by

$$\nabla \times \boldsymbol{U} = \omega(\beta + \alpha)\hat{\mathbf{e}}_z, \qquad s = \frac{\partial U_x}{\partial y} + \frac{\partial U_y}{\partial x} = \omega(\beta - \alpha), \tag{3.16}$$

respectively, and both are constants. The vorticity parameter Sr_ω defined in (3.10) then is

$$Sr_\omega = \frac{\omega(\beta + \alpha)R}{U_0}\,. \tag{3.17}$$

In a straining flow this is not a useful parameter since then $\beta = -\alpha$ and thus Sr_ω = 0. Therefore in addition we introduce the ratio

$$Sr = \frac{sR}{U_0} = \frac{\omega(\beta - \alpha)R}{U_0}\,, \tag{3.18}$$

which is a dimensionless measure of the shear rate. In the simulations described in the next section the particle Reynolds number is kept fixed while the parameters α and β are varied.

To investigate the effect of shear in the cross-stream direction, the streamwise shear parameter β is set to 1 while the cross-stream shear parameter α is varied between –1 and 1. When α = 1, the liquid is in solid-body rotation as in figure 3.7a. For α = 0 the sphere is in a streamwise shearing flow, with the shear in the same direction as the uniform component, see figure 3.7b. For α = –1 the flow is a combination of a pure straining and a uniform downward flow, with the particle displaced horizontally from the center of strain, as in figure 3.7c. Intermediate values of α interpolate between these situations.

To see the influence of streamwise shear, when a cross-stream shear component is also present, the parameter α is set to 1 and the parameter β is varied between –1 and 1. For β = 1 we have the same solid-body rotation as in figure 3.7a. For β = 0 we have a uniform flow with a cross-stream shear. The local incident flow field around the particle is shown in figure 3.7d. For β = –1 once again we find a combination of a uniform component and a strain, except that now the strain is in the direction opposite to that shown in figure 3.7c.

3.7 Numerical results for fixed Re, varying α and β

At steady-state, a particle immersed in the flows described in the previous section will spin with an angular velocity Ω_p such that the hydrodynamic couple to which it is subject vanishes. In the Stokes limit the angular velocity of the particle will be the same as that of the fluid so that $\Omega_p/\omega = \frac{1}{2}(\beta + \alpha)$.

In figure 3.15 the particle spin rate, normalized by ω, is shown as a function of the parameter α, with β fixed to 1, or β, with α fixed to 1. If α or β is set to 1, while the other parameter is varied, in the Stokes limit the result is independent of which parameter is held fixed and which one is varied, as indicated by the dotted line in the figure: the angular velocity of the particle increases linearly with both α and β, and therefore also with the vorticity. When inertial effects are accounted for, however, it is relevant which of the two shear components is varied. For the results shown in figure 3.15 the Reynolds number is 20. When the streamwise shear is fixed (β = 1, squares), the spin rate is below the Stokes value over most of the range except when the cross-stream component is close to 1. When the cross-stream component is fixed, however (α = 1, diamonds), the spin rate is always above the Stokes value. These results clearly show that the angular velocity of the particle more strongly depends on the cross-stream than on the streamwise shear.

The case $\alpha = 0$, $\beta = 1$ (middle square in figure 3.15) represents a linear shear flow, the shear component being in the flow direction. We find Ω_p/ω = 0.36, the decrease with respect to the Stokes limit (Ω_p/ω = 0.5) being due to inertial effects. The flow field in the symmetry plane can be seen in figure 3.24b. For the same Reynolds number, the fit (3.7) to Bagchi & Balachandar's (2002a) results predicts a normalized particle angular velocity of Ω_p/ω = 0.35, very close to our value (see table 3.2).

In the pure strain cases ($\alpha = 1$, $\beta = -1$ or $\alpha = -1$, $\beta = 1$) the particle is found to rotate with Ω_p/ω = 0.36 and –0.36, respectively, in spite of the fact that the undisturbed flow itself has no vorticity. Bagchi and Balachandar [7] considered the case of a particle moving through a straining field and also found the particle to rotate as long as neither of the principal axes of the strain was aligned

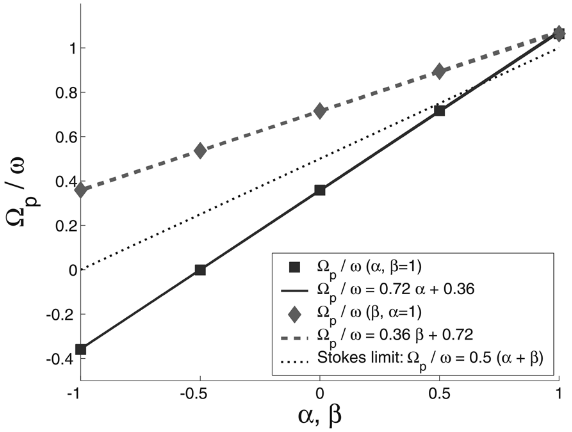

Figure 3.15: Particle spin rate normalized by ω vs. α, for β = 1 (squares), and β, for α = 1 (diamonds) for $Re = 20$; the dotted line is the Stokes result. The solid and dashed lines show the result obtained by linearly superposing the values of Ω_p/ω induced separately by each shear flow type.

with the relative velocity. This case is quite similar to our situation of a particle fixed in a straining flow to which a uniform flow is added, and indeed in our case no principal axis of the strain is aligned with the uniform flow component. The streamwise shear induces a clockwise rotation, whereas the cross-stream shear induces a counterclockwise rotation when α = 1, β = –1. The contribution of the streamwise shear component appears to be less effective, so that the resultant spin is in the direction of the cross-stream shear. The cross-section of the flow field around the particle shown in figure 3.24e indicates a deflection of the wake to the right due to the cross-stream shear. For a cross-stream shear with $\alpha = 1$, $\beta = 0$ (middle diamond in figure 3.15), we find Ω_p/ω = 0.72, which is an increase with respect to the Stokes limit (Ω_p/ω = 0.5).

To better understand these different phenomena, the effects of the two shear types were investigated separately by setting one of the parameters to 0 and varying the other one. The results are shown in figure 3.16; as before, the dotted line is the Stokes limit. Once again, the cross-stream shear gives rise to a much higher spin rate (in modulus) than the streamwise shear. The results of the cross-stream shear lie above the Stokes limit, those of the streamwise shear below. So, whereas inertial effects decrease the particle spin rate due to streamwise shear, they increase it in the presence of a cross-stream shear.

In figure 3.15, the solid line closely matching the squares shows the relation $\Omega_p/\omega = 0.36 + 0.72\,\alpha$ and is the sum of 0.36, the normalized angular velocity

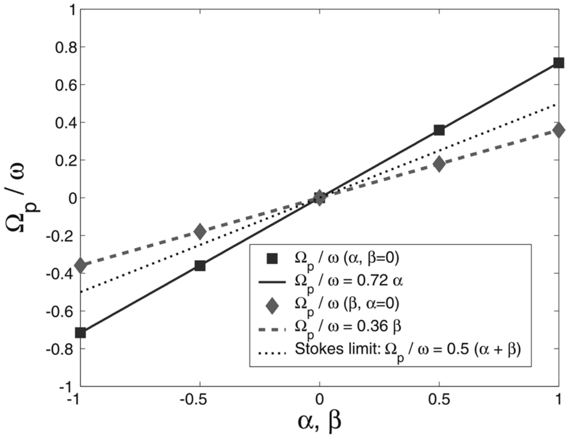

Figure 3.16: Particle angular velocity normalized by ω vs. α, for $\beta = 0$ (squares) and β, for $\alpha = 0$ (diamonds) for $Re = 20$; the dotted line is the Stokes result. The solid and dashed lines represent linear fits.

calculated for α = 0 and β = 1 (streamwise shear flow) and a linear fit to the value of Ω_p/ω calculated for β = 0 and variable α (i.e. variable cross-stream shear, see figure 3.16). Similarly, the dashed line represents the relation $\Omega_p/\omega = 0.72 + 0.36\,\beta$, which is the sum of the angular velocity calculated for α = 1 and β = 0 (cross-stream shear flow), 0.72, and a linear fit to the value of Ω_p/ω calculated for α = 0 and variable β. In table 3.4 the torque-free particle spin rates for different flow types at different Reynolds numbers are given. Apparently, one can add, resp. subtract, the particle spin rates in a cross-stream shear and a streamwise shear to find the spin rates in a solid-body rotation, resp. straining flow. It is remarkable that a linear combination very accurately reproduces the computational results in spite of the nonlinearity of the governing equations. Probably this is a consequence of the relative smallness of the shear flows with respect to the incident uniform flow in the cases studied (Sr and Sr_ω are of the order 0.1). This finding may be useful as it permits the deduction of properties of the combined flow from those of its individual components.

3.8 Shear stress

The results of the previous section show a clear distinction between the effects of the streamwise shear flow and the other types of flow on particle spin. The streamwise shear flow causes a decrease in particle spin rate with increasing Reynolds number, whereas all others show an increase (table 3.4). The increase is smallest

Flow type	α	β	Ω_P/ω	α	β	Ω_P/ω	α	β	Ω_P/ω
	$Re \to 0$			$Re = 20$			$Re = 50$		
Linear shear	0	1	0.5	0	1	0.36	0	1	0.30
Cross-stream	1	0	0.5	1	0	0.72	1	0	0.91
Solid-body rotation	1	1	1	1	1	1.07	1	1	1.20
Strain	1	–1	0	1	–1	0.36	–1	1	–0.61

Table 3.4: Results for the normalized particle angular velocity for different types of flow at Re = 20 and Re = 50 compared with the results for Stokes flow.

for a solid-body rotation, larger for the cross-stream shear and largest for straining flow.

With the coordinates as given in figure 3.17, the component of the hydrodynamic couple around the rotation axis is

$$T = a^3 \int \sigma_{r\phi} \ (\sin\theta)^2 \ \mathrm{d}\theta \, \mathrm{d}\phi \tag{3.19}$$

in which $a \sin\theta$ is the distance of the surface element $a^2 \ \sin\theta \ \mathrm{d}\theta \, \mathrm{d}\phi$ from the axis and $\sigma_{r\phi}$ the appropriate component of the viscous stress. The flow around particles prevented from rotating results in a non-zero value for this integral, while it will vanish for particles rotating in a torque-free state. It is therefore interesting to contrast the detailed distribution of $\sigma_{r\phi}$ on the particle surface in these two situations and for the different flows. (A useful feature of the Physalis method is that the values of the shear stress are proportional to the coefficients of the spherical harmonic expansion mentioned in § 3.5.)

A steady two-dimensional boundary layer separates from a fixed wall at a point of zero shear stress. In our case the boundary layer is three-dimensional and, with a freely rotating particle, on a moving boundary. Thus the situation is much more complex (Dandy and Dwyer [17], Degani, Walker, and Smith [18], Délery [19], Surana, Grunberg, and Haller [59], Van Dommelen and Cowley [63], Williams III [68]). Still, the separated flow behind the sphere will correspond to a region of low $\sigma_{r\phi}$. With reference to figure 3.17b, we define angles ϕ_1 and ϕ_2 as limiting angles of the low-shear-stress region where $|\sigma_{r\phi}/(\mu U_0/a)| <$ 0.05 on the sphere equator. The coordinate system is shown in figure 3.17a; the incident flow is in the negative y-direction.

Figure 3.18a-c displays $\sigma_{r\phi}$ on the sphere for a uniform flow with $Re = 50$. Figure 3.18b is a top view of the sphere; figure 3.18a shows contours of $\sigma_{r\phi}$ in a $(\phi\,\theta)$-plot. Another way to present this information is a Hammer–Aitoff projection

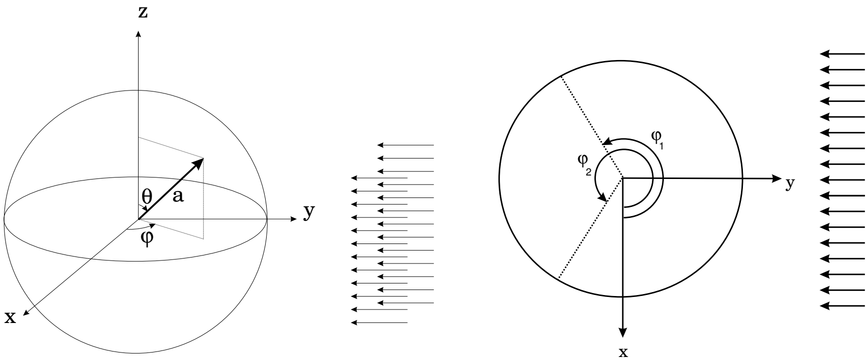

(a) (b)

Figure 3.17: (a) Coordinate system for the sphere with incoming flow, (b) top view of the sphere with the angles ϕ_1 and ϕ_2 marking the region of low shear stress, $|\sigma_{r\phi}/(\mu U_0/a)| < 0.05$.

(see e.g. Bugayevskiy and Snyder [11]), which has the advantage of preserving areas. Figure 3.18c shows this Hammer–Aitoff projection for the uniform flow at $Re = 50$; the contours in panels a, c, and d are in steps of 0.05. The incoming flow arrives at the sphere along the line $\phi = \pi/2$ where $\sigma_{r\phi} = 0$. Behind the sphere (ϕ between π and 2π), the flow separates, and here we see a large region of low shear stress, the green area.

Figure 3.18d shows $\sigma_{r\phi}$ for $Re = 20$. The region of low shear stress (green area) is smaller, indicating that the flow separates later than for $Re = 50$. Furthermore the values of $\sigma_{r\phi}$ are larger.

We now consider the situation where a solid-body rotation (in the positive z-direction, $\alpha = \beta = 1$ in (3.15)) is added to the uniform flow. Figures 3.19e and 3.19f, respectively for a non-spinning and a spinning sphere, permit a comparison of the stress distribution in the two cases. It can be seen that the region of low shear stress (the white region) is shifted somewhat clockwise for the spinning particle (figure 3.19f) compared to the non-spinning one (figure 3.19e). Both ϕ_1 and ϕ_2 decrease (compare the location of the contours near the dotted $5\pi/4$ and $7\pi/4$ lines), suggesting that the flow remains attached longer on the side of positive x (as defined in figure 3.17) and detaches at an earlier stage for negative x. Close examination of figures 3.19e and 3.19f shows that the front stagnation point moves a little counterclockwise for a spinning sphere.

In figure 3.18e and 3.18f the uniform-flow distribution is subtracted from the solid-body rotation at $Re = 20$. The less positive values of $\sigma_{r\phi} - \sigma_{r\phi,\, uniform}$ close to the dotted $5\pi/4$ and $7\pi/4$ lines suggest that the flow separates at lower

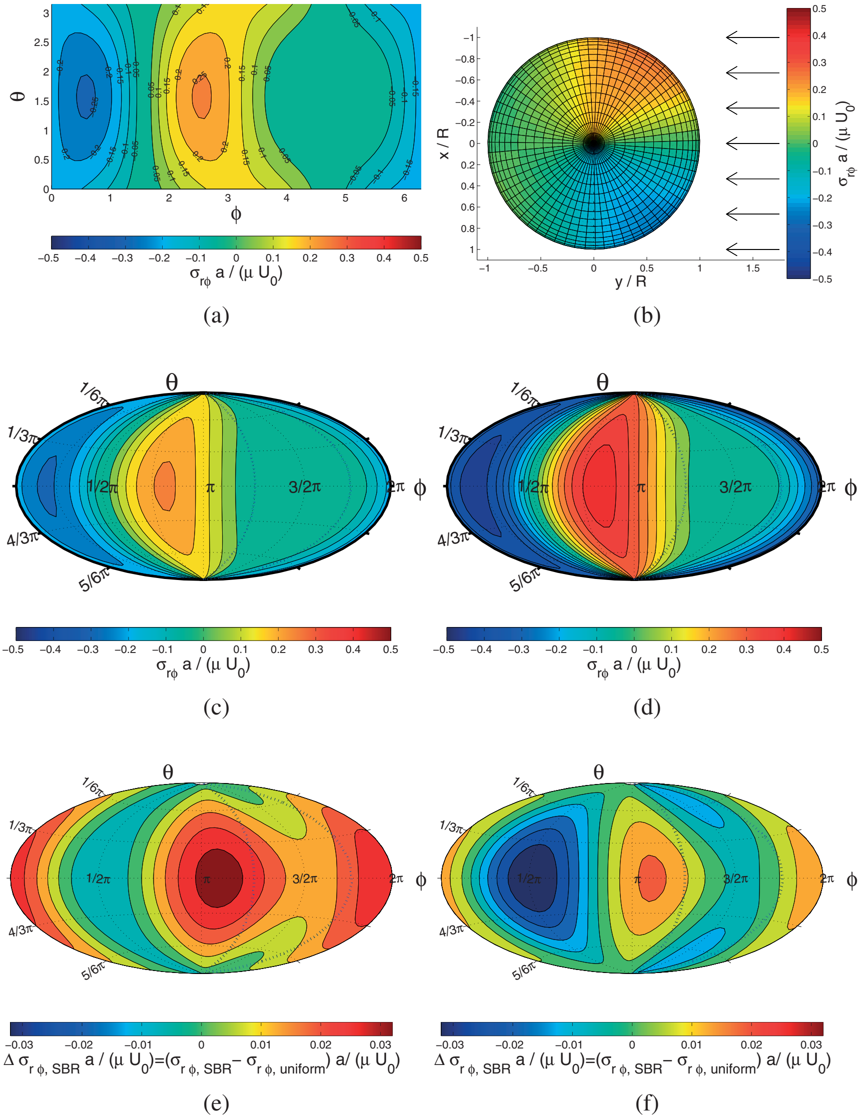

(a) (b) (c) (d) (e) (f)

Figure 3.18: $\sigma_{r\phi}$ (a) Uniform flow, $Re = 50$, $(\phi\,\theta)$-plot, (b) top view or xy-projection, (c) Hammer–Aitoff projection. (d) Uniform flow, $Re = 20$, Hammer–Aitoff projection. (e) Difference between solid-body rotation and uniform flow, $Re = 20$, non-rotating, (f) as (e) but, rotating. For the definition of ϕ and θ, see figure 3.17.

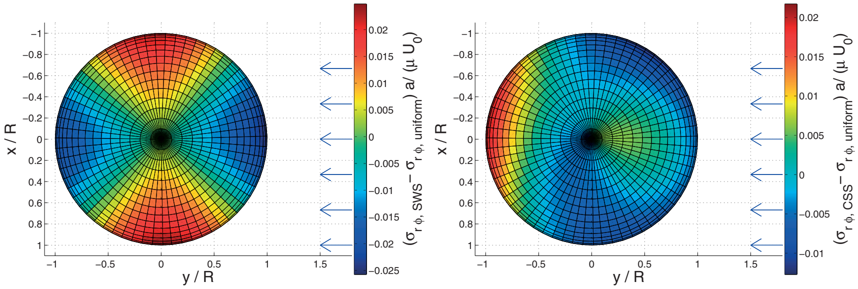

(g) (h)

Figure 3.18: (continued from the previous page) $\sigma_{r\phi}$ (g) Top view of difference between streamwise shear and uniform flow, $Re = 50$, rotating. (h) Top view of difference between cross-stream shear and uniform flow, $Re = 20$, rotating. For the definition of ϕ and θ, see figure 3.17.

ϕ-values for the spinning particle. Furthermore the front stagnation point shifts counterclockwise as before owing to the particle spin.

The plots at the left of figure 3.19 display the $(r\phi)$-component of the shear stress for a non-rotating particle in the four cases of streamwise shear, cross-stream shear, solid-body rotation and strain. The region of low shear stress is the white region. The angle ϕ_1 shifts to higher values in the sequence streamwise shear, solid-body rotation, cross-stream shear, strain. Note that this is the same order as found for the Reynolds number dependence of the particle spin. There is also a small shift in ϕ_2. A larger value of ϕ_1 indicates that the shear stress remains high along a larger fraction of the sphere surface on the positive shear stress side, which helps the particle spin. A larger ϕ_2, on the other hand, suggests an earlier separation on the side of the negative shear stress. This means that a shift of ϕ_1 and ϕ_2 in the direction of rotation favors the particle spin. When the particle is rotating as shown in the right panels of figure 3.19, the differences between the flow types become less clear, since the particle spin causes the region of low shear stress to move back. For example, the particle in a solid-body rotation spins faster than in a streamwise shear. As a result, the region of low shear shifts clockwise and ends up at almost the same location as for the streamwise shear.

In figure 3.20 the uniform flow result is subtracted from the other flow types for $Re = 20$. In the a-plots we can see that the shear stress distribution remains quite symmetric for a stream-wise shear, as is also clear from the top view in figure 3.18g.

If we add $(\sigma_{r\phi,\,sws} - \sigma_{r\phi,\,uniform}$ for a stream wise shear, figure 3.20a) and $(\sigma_{r\phi,\,css} - \sigma_{r\phi,\,uniform}$ for the cross stream shear, figure 3.20b), we obtain the result indicated in figure 3.21a, with a striking resemblance with figure 3.20c. Upon subtracting the two quantities (figure 3.21b) we find a result very close to that of figure 3.20d for the straining flow. Thus, we can simply add, or subtract, the excess $\sigma_{r\phi}$ with respect to uniform flow for streamwise and cross-stream shear to find approximately the result for solid body rotating or straining flow. For $Re = 50$ this approximation is still good (figures 3.22 and 3.23). We found earlier in § 3.7 the same additive property for the particle spin rates.

3.9 Physical considerations

In § 3.7 we have seen that a linear addition for the spin rates is possible for $Re = 20$ and $Re = 50$. The results in § 3.8 show that the same holds for the change in the $(r\phi)$-component of the shear stress due to a disturbance of the uniform flow. Furthermore, when adding a shear component to the uniform flow, a shift of the low-shear region was seen. What causes the displacement?

For a fixed, non-rotating particle the previous expression (3.19) for the torque may be written as

$$T = -\mu a^3 \int \omega_\theta \sin^2\theta \, \mathrm{d}\theta \, \mathrm{d}\phi \; . \tag{3.20}$$

When a sphere is held fixed in a steady uniform flow, an axisymmetric stationary toroidal vortex forms behind it up to a Reynolds number of about 210 (Johnson and Patel [31], Natarajan and Acrivos [50], Taneda [60]). In a uniform flow the torque is zero because of the symmetry in ω_θ. Consider now a perturbation of the incident uniform flow in the form of a strain field such as the one shown in figure 3.7c. This flow, by itself, has no vorticity. Since, as we have seen, the particle rotates in this situation, a non-zero hydrodynamic couple must exist if the particle is prevented from rotating. Since the perturbation carries no vorticity, the hydrodynamic couple must be due to the distortion of the unperturbed vorticity. The strain alters the symmetry of the ω_θ distribution on the particle surface. It is instructive to consider in this light the different flow situations studied in the previous sections. The left-hand column in figure 3.24 shows a sketch of the flow type and the right-hand column is the velocity field in the symmetry plane of the sphere perpendicular to the axis of rotation. The sketches in the central column give a qualitative illustration of how the toroidal vortex behind a sphere in steady uniform flow (shown at the top) may be expected to be modified by the addition of various disturbances to the base uniform flow.

The central sketch in figure 3.24b shows the modification of the toroidal vortex due to a streamwise shear flow component. The vortex is tilted by the flow. The effect of this on the shift of the wake is not clearly visible in the figure. The effect

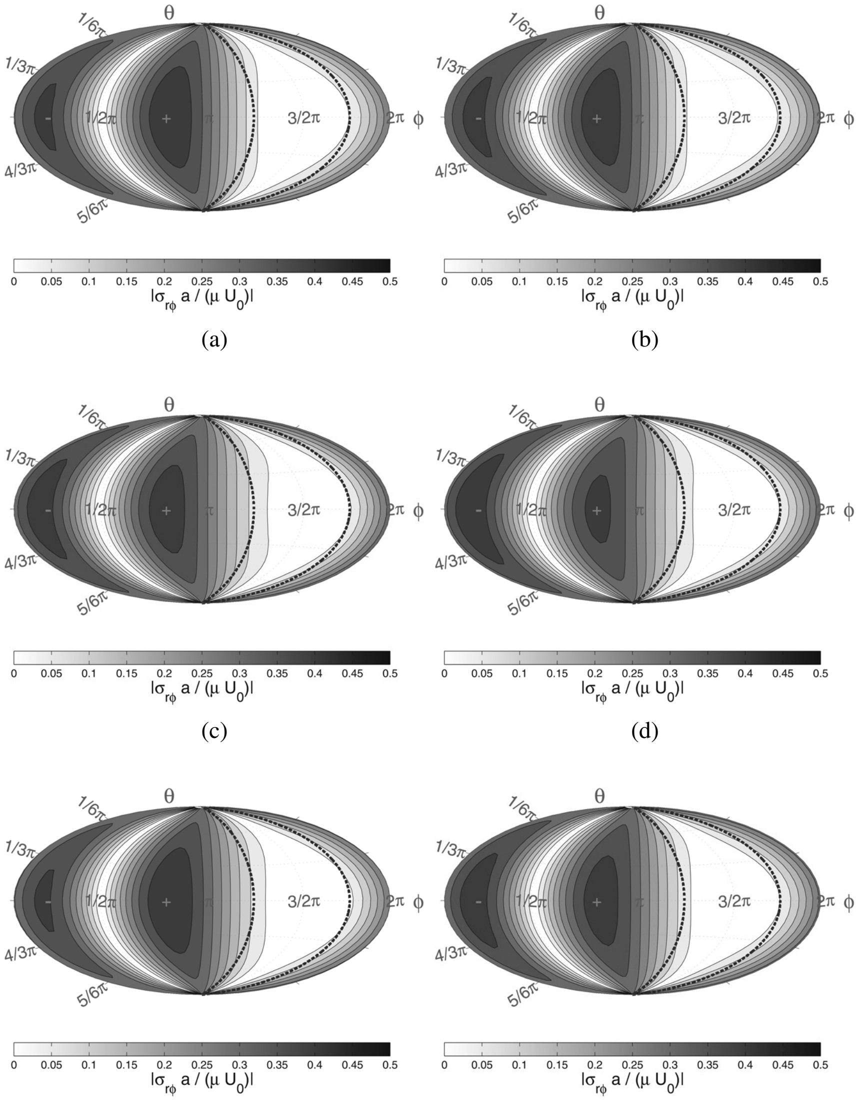

(a) (b)

(c) (d)

(e) (f)

Figure 3.19: $|\sigma_{r\phi}|$, $Re = 20$. (a) Streamwise shear ($Sr = 0.05, Sr_\omega = 0.05$), non-rotating, (b) rotating. (c) Cross-stream shear ($Sr = 0.05, Sr_\omega = 0.05$), non-rotating, (d) rotating. (e) Solid-body rotation ($Sr = 0, Sr_\omega = 0.1$), non-rotating, (f) rotating. For the definition of ϕ and θ, see figure 3.17.

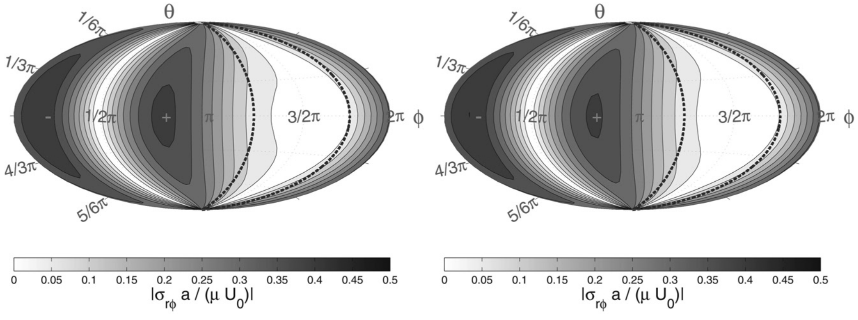

(g) (h)

Figure 3.19: (continued from the previous page) $|\sigma_{r\phi}|$, $Re = 20$. (g) Strain ($Sr = 0.1, Sr_\omega = 0$), non-rotating, (h) rotating. For the definition of ϕ and θ, see figure 3.17.

of a cross-stream shear is much larger. As sketched in figure 3.24(c–e), a cross-stream shear flow tends to displace the toroidal vortex sideways instead of merely tilting it (which is the result of a streamwise shear). The pictures in the right-hand column show that, accordingly, the wake is bent much more strongly. When the cross-stream shear is combined with the streamwise shear to result in a solid-body rotation (figure case 3.24d), the two effects sketched separately in figures 3.24b and c act together and result in the spin rate for a particle in solid-body rotation. Since, with increasing Re, the strength of the toroidal vortex increases, it is reasonable to conclude that the magnitude of the spin will also increase, as indeed found up to a maximum Reynolds number in the data shown in figure 3.3. In the pure straining flow case of figure 3.24e, the streamwise shear opposes the particle spin induced by the cross-stream shear, but the sideways displacement of the vortex ring is more powerful and the particle still spins, though with a lower angular velocity.

The results of figures 3.15 and 3.16 show that shear flow in the cross-stream direction increases the particle spin much more than streamwise shear flow. Harper and Chang [27] investigated a particle moving through a shear field in an arbitrary direction. In their case as well one can see from their lift coefficient that the cross-stream shear has a stronger effect than a streamwise one. This seems to be a general feature of the type of flows investigated in the present parameter range.

Apart from displacing the wake, the shift of the vortices will change the location of the region of low shear, so instead of looking at the wake displacement, we may also look at the angles ϕ_1 and ϕ_2 discussed in § 3.8 to obtain an idea of this shift. Here one should remember that there are two competing effects for a

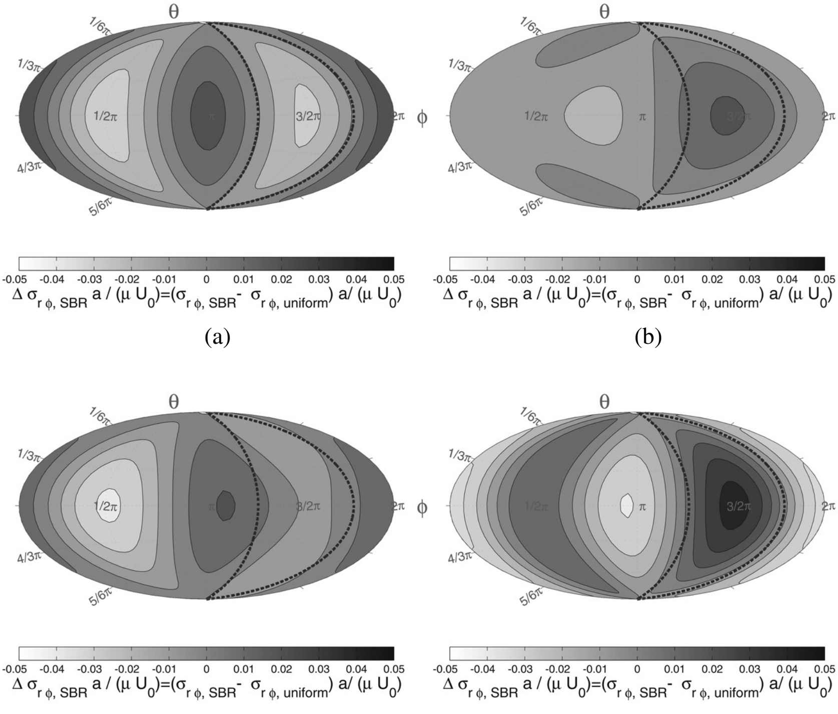

(a) (b)

(c) (d)

Figure 3.20: Differences in $\sigma_{r\phi}$ with uniform flow, $Re = 20$, rotating particle: (a) streamwise shear shear, (b) cross-stream shear, (c) solid-body rotation, (d) strain. For the definition of ϕ and θ, see figure 3.17.

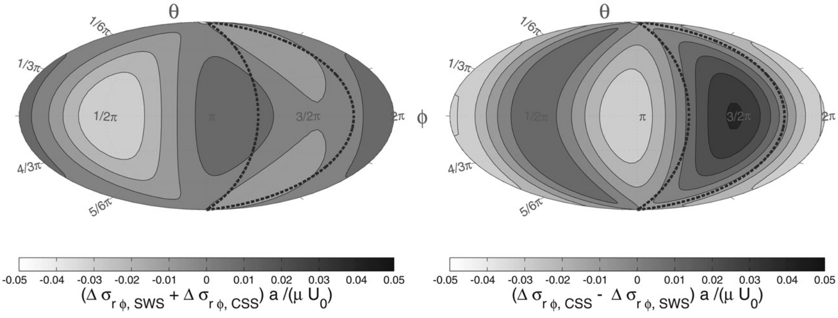

(a) (b)

Figure 3.21: Differences in $\sigma_{r\phi}$ of a streamwise and a cross-stream shear: (a) added, (b) subtracted. $Re = 20$. For the definition of ϕ and θ, see figure 3.17.

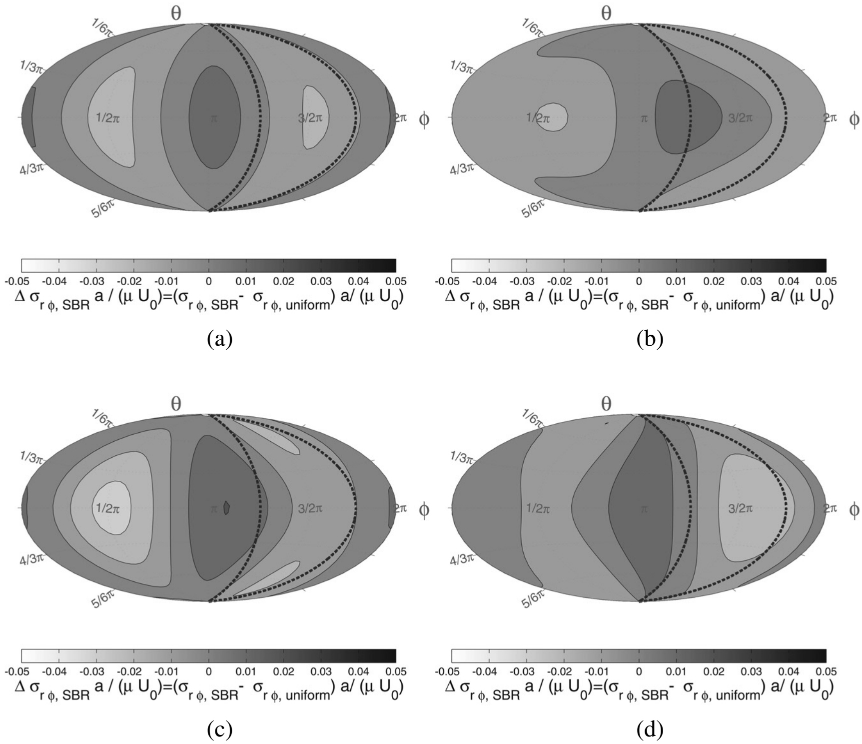

(a) (b)

(c) (d)

Figure 3.22: Differences in $\sigma_{r\phi}$ with uniform flow, $Re = 50$, rotating particle: (a) streamwise shear shear, (b) cross-stream shear, (c) solid-body rotation, (d) strain. For the definition of ϕ and θ, see figure 3.17.

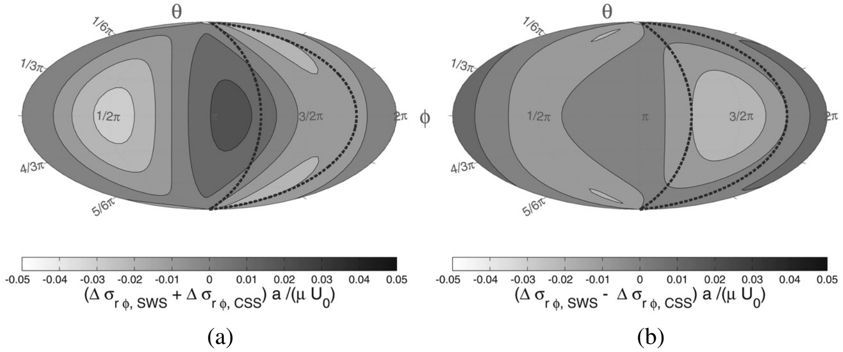

(a) (b)

Figure 3.23: Differences in $\sigma_{r\phi}$ of a streamwise and a cross-stream shear: (a) added, (b) subtracted. $Re = 50$. For the definition of ϕ and θ, see figure 3.17.

rotating sphere: the shear components shift the angles ϕ_1 and ϕ_2 counterclockwise (compare figure 3.19a, c, e, and g with 3.18d), while the particle spin shifts them in clockwise direction (compare figure 3.19a, c, e, and g with b, d, f, and h). From studying the non-rotating cases, we know that the shears increase the angles ϕ_1 and ϕ_2 (though the increase in the latter is minor compared to the increase in the former). This implies a shift of the left stagnation point downward and the right stagnation point slightly upwards in figure 3.24. For the rotating cases the angles are shifted back a little, but in general ϕ_1 is increased. This suggests that the flow remains attached along a larger region on the left-hand side of the sphere than on the right-hand side of the sphere.

So by what mechanism is the particle spin rate decreased for a linear shear and increased for the other flow types? Consider a particle in a uniform flow with its distribution of surface shear, figure 3.18d. The torque on the particle is zero. Addition of a linear shear, always keeping the particle from rotating, causes a change in this distribution of surface stress, figure 3.19a, but the shift of the low-shear-stress region is not large. There is now a torque on the particle which must be externally opposed in order to prevent particle spin. If we take this torque away, only a relatively small spinning rate is sufficient to relax the torque on the particle to zero. When cross-stream shear, strain or solid-body rotation are added to the uniform velocity, there is a much larger displacement of the low-shear-stress regions, see the large shift in ϕ_1 in figure 3.19 c, e and g. The reason for this larger shift in ϕ_1 lies in the sideways displacement of the toroidal vortex, due to the cross stream shear component. A larger spinning rate of the sphere is now needed to relax the torque on the particle to zero.

As the Reynolds number rises, the strength of the vortices will increase. However, owing to stronger convective effects the wake is less deflected. The two competing effects on the wake (increased vortex strength and diminished wake deflection) are reflected in the shear stress values. As the Reynolds number increases, the absolute value of the shear stress decreases (compare figures 3.18c and 3.18d). The differences with uniform flow remain, however, comparable for Re = 20 and Re = 50 (figures 3.20 and 3.22). Relatively, the difference with uniform flow is larger for higher Reynolds number. So even though the shear stress decreases for higher Reynolds number, the effective difference with uniform flow increases and the flow effects on the spin rate will increase with the Reynolds number.

What happens in the highest Reynolds number range investigated in the present experiments with water? Uniform flow past a sphere has been studied extensively and exhibits a complex behavior. The linear stability analysis of Natarajan and Acrivos [50] reveals a first regular bifurcation to a steady non-axisymmetric flow at $Re \simeq 210$, followed by a Hopf bifurcation at $Re \simeq 270$. These results have been confirmed by Ghidersa and Dusek [24] and Thompson, Leweke, and Provansal

[61]. The computations of Johnson and Patel [31] accounting for a finite deviation from axisymmetric flow confirm the steadiness of a non-axisymmetric regime below $Re \simeq 270$, where they find a transition to organized periodic vortex shedding, a result also found by Tomboulides and Orszag [62]. It is interesting to note that the results of Johnson and Patel [31] clearly show the presence of a strong toroidal vortex structure behind the sphere even beyond transition to the unsteady regime after the second bifurcation. Computations by Lee [37] and Lee and Wilczak [38] also suggest that a non-axially-symmetric vortex structure persists up to a Re in the range 350 to 400, while the flow becomes unsteady for $Re > 400$. On the basis of experimental evidence, Taneda [60] states that a similar structure, possibly oscillating, persists until $Re \simeq 400$. He reports a major transition for Re between 400 and 1000 where the more-or-less persistent vortex structure behind the sphere is replaced by unsteady horseshoe-shaped vortex loops. According to Tomboulides and Orszag [62], a chaotic regime sets in for $Re \simeq 500$. The details of some of these conclusions must be modified in the case of free spheres (Jenny et al. [29, 30]), but the general picture of a first regular bifurcation, followed by a Hopf one, a markedly unsteady and eventually a chaotic regime remains essentially unchanged.

There does not appear to be any information on how these features are modified in a rotating flow, but for a linear shear flow the results of Lee and Wilczak [38] show that the same features exist, although the onset threshold is lowered. It may be reasonable to expect that, in our case, the features of a uniform flow qualitatively survive, with different onset thresholds. Therefore, the difference between the steady position of the particle center observed in the glycerine–water mixture and the small precessing motion found in pure water (see § 3.3) may be caused by what in a uniform flow would be the loss of axial symmetry and onset of unsteadiness. Similarly, the steep fall of the rotational velocity when the Reynolds number exceeds a value of $\sim$650 (to the left of the sharp peak in figure 3.3) might be due to the collapse and disappearance of the vortex structure which, as argued before, may very well be the ‘engine’ on which the fast spin relies.

(a) uniform flow

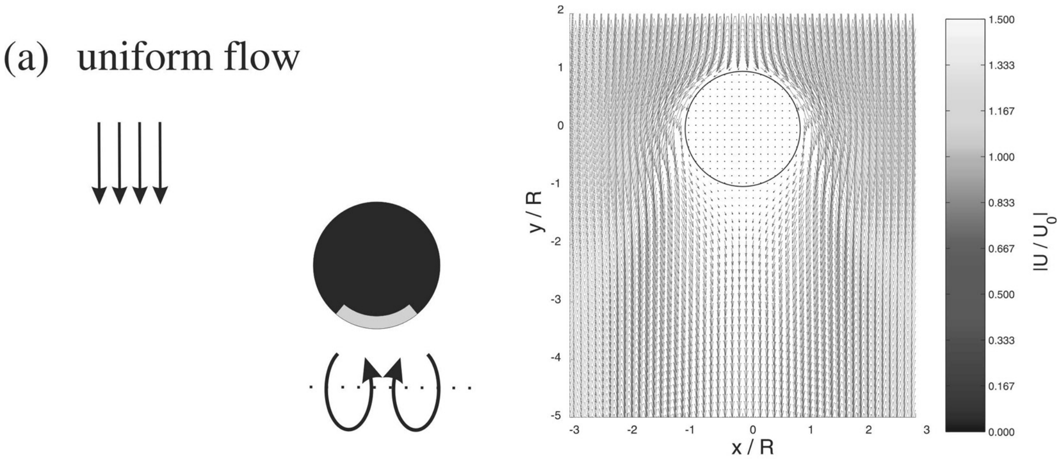

(b) linear shear

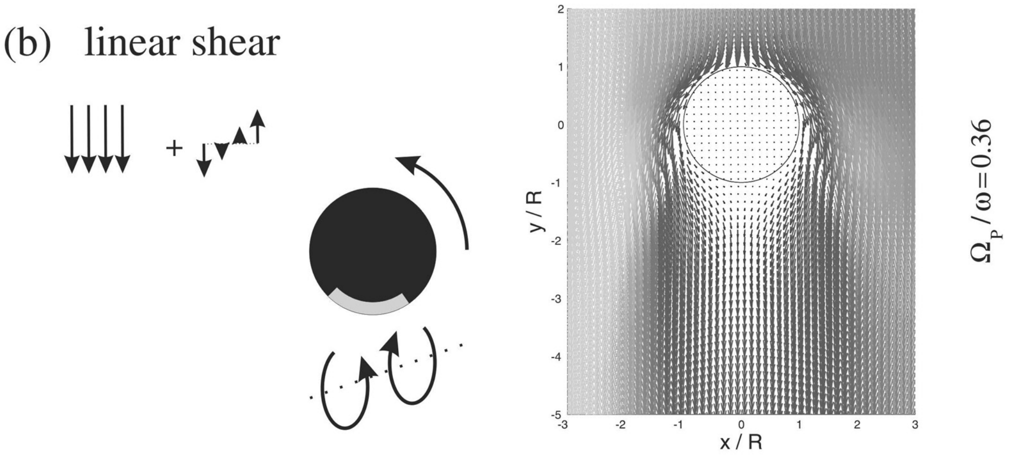

(c) cross-stream shear

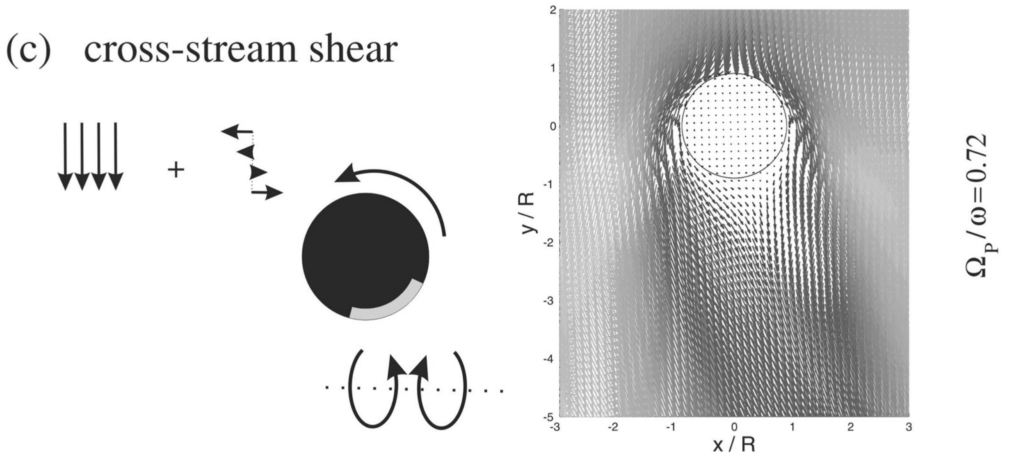

(d) solid body rotation

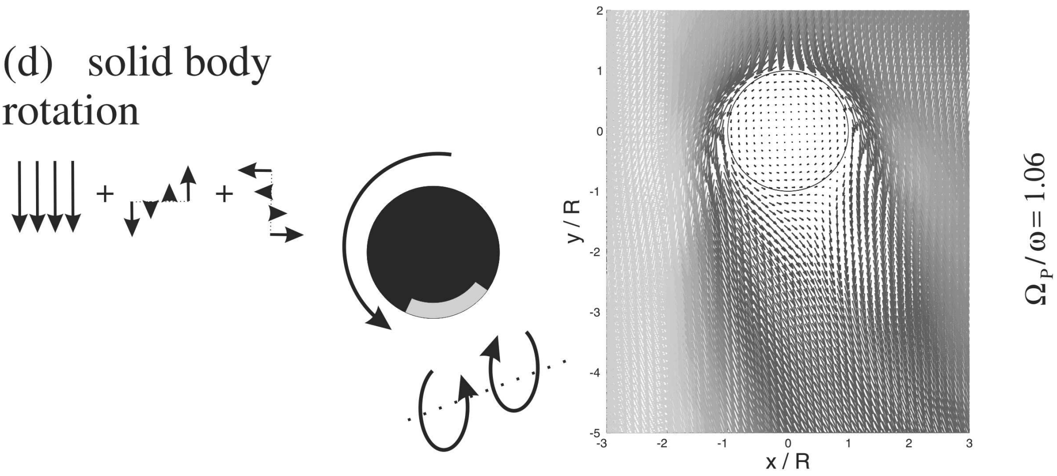

(e) straining flow

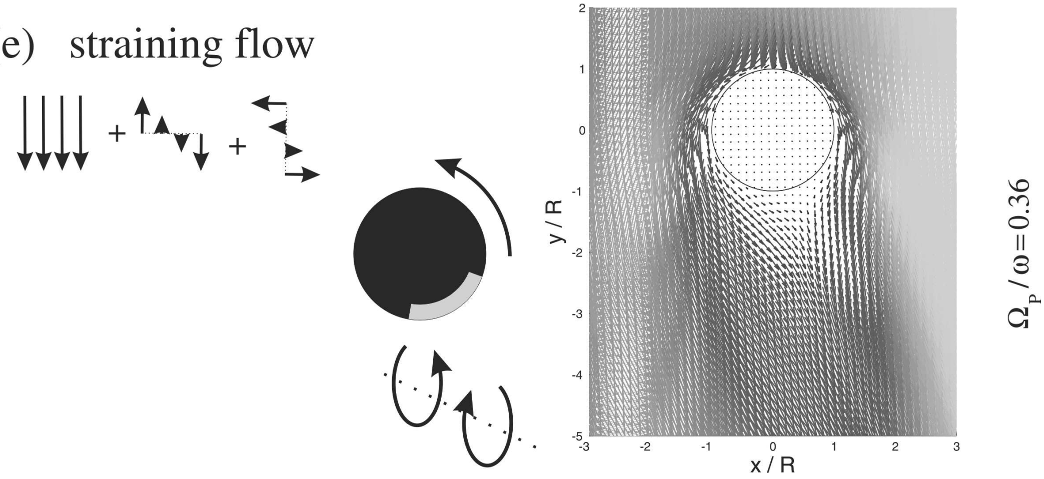

Figure 3.24: Illustration of the proposed mechanism underlying the effects described in this work. The left-hand column shows the components of the flow in which the sphere is immersed. The middle column is a sketch of the displacement of the toroidal vortex and the low shear stress region behind the sphere due to the shear components of the flow. The right-hand column shows the calculated velocity field in the symmetry plane of the sphere in the corresponding flow, all for $Re = 20$. (a) Uniform flow, α = 0, β = 0; (b) linear shear flow, α = 0, β = 1; (c) cross-stream shear flow, α = 1, β = 0; (d) solid-body rotation, α = 1, β = 1; (e) pure strain, α = 1, β = -1.

3.10 Summary

Whereas inertial effects cause a particle to spin more slowly than the fluid in a streamwise shear, we have found that, in the presence of a significant cross-stream shear component of the flow, the particle spins faster than the fluid due to a strong deflection of the wake. Unexpectedly, in the parameter range we have investigated, we found that the spin rates produced by the streamwise and cross-stream shear can be added to give a very close approximation to the spin rate calculated when both shear components are present simultaneously.

Combining the two types of shear into a solid-body rotation gives a result in which the spin rate is larger than that of the ambient fluid. The fact that, in a solid-body rotation, the particle spins faster than the fluid has been confirmed by experiment and simulation. The difference between the influence of the two shear types yields the particle spin rate in a strain flow combined with a uniform flow.

A study of the shear stress on the particle surface suggests the location of the separation lines. In view of the complexity of three-dimensional separation on a moving wall, we have not attempted to determine precisely the position on these lines. We have simply identified the region of low shear stress behind the particle. When a cross-stream shear is present this region moves counterclockwise with respect to the uniform flow. For a rotating particle, the low-shear region to some extent moves back clockwise.

A tentative explanation for the phenomenon is based on the different modifications of the vortex structure behind the sphere caused by the different flows. The cross-stream shear causes a sideways displacement of the vortex structure and a shift in the low-shear region. Since the strength of this vortex increases with Re, so does the effect. This trend abruptly breaks down at $Re \sim 650$, where the particle spin rate starts to decrease until ultimately falling below that of the fluid. We have suggested that this qualitative change may be due to the destabilization and disappearance of the vortex structure behind the sphere.

The particle spin has a clear effect on the lift coefficient in the intermediate-Reynolds-range. We have computed that, in a solid-body rotation at $Re = 20$ and 50, the lift coefficient is 47% and 34%, respectively, larger for a rotating than for a non-rotating sphere.

References

[1] P. Annamalai and R. Cole. Particle migration in rotating liquids. *Phys. Fluids*, 29:647–649, 1986.

[2] T. R. Auton. The lift force on a spherical body in a rotational flow. *J. Fluid Mech.*, 183:199–218, 1987.

[3] T. R. Auton, J. C. R. Hunt, and M. Prud'homme. The force excerted on a body in inviscid unsteady non-uniform rotating flow. *J. Fluid Mech.*, 197: 241–257, 1988.

[4] P. Bagchi. *Particle dynamics in inhomogeneous flows at moderate-to-high Reynolds number*. PhD thesis, University of Illinois, 2002.

[5] P. Bagchi and S. Balachandar. Shear versus vortex-induced lift force on a rigid sphere at moderate Re. *J. Fluid Mech.*, 473:379–388, 2002.

[6] P. Bagchi and S. Balachandar. Effect of free rotation on the motion of a solid sphere in linear shear flow at moderate Re. *Phys. Fluids*, 14:2719–2737, 2002.

[7] P. Bagchi and S. Balachandar. Inertial and viscous force on a rigid sphere in straining flows at moderate Reynolds numbers. *J. Fluid Mech.*, 481:105–148, 2003.

[8] H. M. Barkla and L. J. Auchterlonie. The Magnus or Robins effect on rotating spheres. *J. Fluid Mech.*, 47:437–447, 1971.

[9] J. J. Bluemink, E. van Nierop, S. Luther, N. Deen, J. Magnaudet, A. Prosperetti, and D. Lohse. Asymmetry-induced particle drift in a rotating flow. *Phys. Fluids*, 17:072106, 2005.

[10] D. Brown, R. Cortez, and M. Minion. Accurate projection methods for the incompressible Navier-Stokes equations. *J. Comput. Phys.*, 168:196–216, 2001.

[11] L. M. Bugayevskiy and J. P. Snyder. *Map Projections - A Reference Manual.* Taylor & Francis, London, 1995.

[12] F. Candelier, J. R. Angilella, , and M. Souhar. On the effect of the Boussinesq-Basset force on the radial migration of a stokes particle in a vortex. *Phys. Fluids*, 16:1765–1776, 2004.

[13] F. Candelier, J.-R. Angilella, and M. Souhar. On the effect of inertia and history forces on the slow motion of a spherical solid or gaseous inclusion in a solid-body rotation flow. *J. Fluid Mech.*, 545:113–139, 2005.

[14] S. Childress. The slow motion of a sphere in a rotating, viscous fluid. *J. Fluid Mech.*, 20:305–314, 1964.

[15] R. Clift, J. R. Grace, and M. E. Weber. *Bubbles, Drops and Particles*. Academic Press, New York, 1978.

[16] C. F. M. Coimbra and M. H. Kobayashi. On the viscous motion of a small particle in a rotating cylinder. *J. Fluid Mech.*, 469:257–286, 2002.

[17] D. S. Dandy and H. A. Dwyer. A sphere in shear flow at finite Reynolds number: effect of shear on particle lift, drag, and heat transfer. *J. Fluid Mech.*, 216:381–410, 1990.

[18] A. T. Degani, J. D. A. Walker, and F. T. Smith. Unsteady separation past moving surfaces. *J. Fluid Mech.*, 375:1–38, 1998.

[19] J. M. Délery. Robert Legendre and Henri Werlé: Toward the elucidation of three-dimensional separation. *Annu. Rev. Fluid Mech.*, 33:129–154, 2001.

[20] S. C. R. Dennis and J. D. A. Walker. Calculation of the steady flow past a sphere at low and moderate Reynolds numbers. *J. Fluid Mech.*, 48:771–789, 1971.

[21] S. C. R. Dennis, S. N. Singh, and D. B. Ingham. The steady flow due to a rotating sphere at low and moderate Reynolds numbers. *J. Fluid Mech.*, 101: 257–279, 1980.

[22] D. A. Drew and R. T. Lahey. The virtual mass and lift force on a sphere in rotating and straining inviscid flow. *Intl J. Multiphase Flow*, 13:113–121, 1987.

[23] H. Gao, P. S. Ayyaswamy, and P. Ducheyne. Dynamics of a microcarrier particle in the simulated microgravity environment of a rotating-wall vessel. *Microgravity Sci. Technol.*, 10:154–165, 1997.

[24] B. Ghidersa and J. Dusek. Breaking of axisymmetry and onset of unsteadiness in the wake of a sphere. *J. Fluid Mech.*, 423:33–69, 2000.

[25] T. Gotoh. Brownian motion in a rotating flow. *J. Statist. Phys.*, 59:371–402, 1990.

[26] J. Happel and H. Brenner. *Low Reynolds Number Hydrodynamics*. Prentice Hall, Englewood Cliffs, 1965.

[27] E. Y. Harper and I-Dee Chang. Maximum dissipation resulting from lift in a slow viscous shear flow. *J. Fluid Mech.*, 33:209–225, 1968.

[28] I. H. Herron, S. D. Davis, and F. P. Bretherton. On the sedimentation of a sphere in a centrifuge. *J. Fluid Mech.*, 68:209–234, 1975.

[29] M. Jenny, G. Bouchet, and J. Dusek. Nonvertical ascension or fall of a free sphere in a newtonian fluid. *Phys. Fluids*, 15:L9–L12, 2003.

[30] M. Jenny, J. Dusek, and G. Bouchet. Instabilities and transition of a sphere falling or ascending freely in a newtonian fluid. *J. Fluid Mech.*, 508:201–239, 2004.

[31] T. A. Johnson and V. C. Patel. Flow past a sphere up to a Reynolds number of 300. *J. Fluid Mech.*, 378:19–70, 1999.

[32] D. Kim and H. Choi. Laminar flow past a sphere rotating in the streamwise direction. *J. Fluid Mech.*, 461:365–386, 2002.

[33] S. Kim and S. Karrila. *Microhydrodynamics*. Butterworth-Heinemann, Boston, 1991.

[34] M. H. Kobayashi and C. F. M. Coimbra. On the stability of the Maxey-Riley equation in nonuniform linear flows. *Phys. Fluids*, 17:113301, 2005.

[35] R. Kurose and S. Komori. Drag and lift forces on a rotating sphere in a linear shear flow. *J. Fluid Mech.*, 384:183–206, 1999.

[36] H. Lamb. *Hydrodynamics, 6th Edn.* Dover, New York, 1932.

[37] S. S. Lee. A numerical study of the unsteady wake behind a sphere in a uniform flow at moderate Reynolds numbers. *Comput. Fluids*, 29:639–667, 2000.

[38] S. S. Lee and J. M. Wilczak. The effects of shear flow on the unsteady wakes behind a sphere at moderate Reynolds numbers. *Fluid Dyn. Res.*, 27:1–22, 2000.

[39] M. J. Lighthill. Drift. *J. Fluid Mech.*, 1:31–53, 1956.

[40] C. J. Lin, J. H. Peery, and W. R. Schowalter. Simple shear flow round a rigid sphere: inertial effects and suspension rheology. *J. Fluid Mech.*, 44:1–17, 1970.

[41] D. Lohse and A. Prosperetti. Controlling bubbles. *J. Phys.: Condens. Matter*, 15:S415–S420, 2003.

[42] J. Magnaudet, M. Rivero, and J. Fabre. Accelerated flows past a rigid sphere or a spherical bubble. *J. Fluid Mech.*, 284:97–135, 1995.

[43] J. B. McLaughlin. Inertial migration of a small sphere in linear shear flows. *J. Fluid Mech.*, 224:261–274, 1991.

[44] R. Mei. An approximate expression for the shear lift force on a spherical bubble at finite Reynolds number. *Intl J. Multiphase Flow*, 18:145–147, 1992.

[45] D. R. Mikulencak and J. F. Morris. Stationary shear flow around fixed and free bodies at finite Reynolds number. *J. Fluid Mech.*, 520:215–242, 2004.

[46] L. M. Milne-Thompson. *Theoretical hydrodynamics*. Macmillan, London, 1968.

[47] P. H. Mortensen, H. I. Andersson, J. J. J. Gillissen, and B. J. Boersma. Particle spin in a turbulent shear flow. *Phys. Fluids*, 19:078109, 2007.

[48] T. Mullin, Y. Li, C. del Pino, and J. Ashmore. An experimental study of fixed points and chaos in the motion of spheres in a stokes flow. *IMA J. of Appl. Maths*, 70:666–676, 2005.

[49] M. A. Naciri. *Contribution à l'étude des forces exercées par un liquide sur une bulle de gaz: portance, masse ajoutée et interactions hydrodynamiques*. PhD thesis, L'Ecole Central de Lyon, 1992.

[50] R. Natarajan and A. Acrivos. The instability of the steady flow past spheres and disks. *J. Fluid Mech.*, 254:323–344, 1993.

[51] B. Oesterlé and T. Bui Dinh. Experiments on the lift of a spinning sphere in a range of intermediate Reynolds numbers. *Exps. Fluids*, 25:16–22, 1998.

[52] P. Paradisi and F. Tampieri. Stability analysis of solid particle motion in rotational flows. *Nuovo Cimento C*, 24c:407–420, 2001.

[53] G. G. Poe and A. Acrivos. Closed-streamline flows past rotating single cylinders and spheres: inertia effects. *J. Fluid Mech.*, 72:605–623, 1975.

[54] N. Raju and E. Meiburg. Dynamics of small, spherical particles in vortical and stagnation point flow fields. *Phys. Fluids*, 9:299–314, 1997.

[55] G. O. Roberts, D. M. Kornfeld, and W. W. Fowlis. Particle orbits in a rotating liquid. *J. Fluid Mech.*, 229:555–567, 1991.

[56] S. I. Rubinow and J. B. Keller. The transverse force on a spinning sphere moving in a viscous fluid. *J. Fluid Mech.*, 11:447–459, 1961.

[57] P. G. Saffman. The lift on a small sphere in a slow shear flow. *J. Fluid Mech.*, 22:385–400; and Corrigendum, **31** p. 624 (1968), 1965.

[58] G. Sridhar and J. Katz. Drag and lift forces on microscopic bubbles entrained by a vortex. *Phys. Fluids.*, 7:389–399, 1995.

[59] A. Surana, O. Grunberg, and G. Haller. Exact theory of three-dimensional flow separation. Part 1. Steady separation. *J. Fluid Mech.*, 564:57–103, 2006.

[60] S. Taneda. Visual observations of the flow past a sphere at Reynolds numbers between 10^4 and 10^6. *J. Fluid Mech.*, 85:178–192, 1978.

[61] M. C. Thompson, T. Leweke, and M. Provansal. Kinematics and dynamics of sphere wake transition. *J. Fluids Struct.*, 15:575–585, 2001.

[62] A. G. Tomboulides and S. A. Orszag. Numerical investigation of transitional and weak turbulent flow past a sphere. *J. Fluid Mech.*, 416:45–73, 2000.

[63] L. L. Van Dommelen and S. J. Cowley. On the Lagrangian description of unsteady boundary layer separation. Part 1. General theory. *J. Fluid Mech.*, 210:593–626, 1990.

[64] E. A. van Nierop, S. Luther, J. J. Bluemink, J. Magnaudet, A. Prosperetti, and D. Lohse. Drag and lift forces on bubbles in a rotating flow. *J. Fluid Mech.*, 571:439–454, 2007.

[65] Y. Wang, X. Lu, and L. Zhuang. Numerical analysis of the rotating viscous flow approaching a solid sphere. *Intl J. Numer. Meth. Fluids*, 44:905–925, 2004.

[66] E. H. Wedemeyer. The unsteady flow within a spinning cylinder. *J. Fluid Mech.*, 20:383–399, 1964.

[67] A. J. Weisenborn. Drag on a sphere moving slowly in a rotating viscous fluid. *J. Fluid Mech.*, 153:215–227, 1985.

[68] J. C. Williams III. Incompressible boundary-layer separation. *Annu. Rev. Fluid Mech.*, 9:113–144, 1977.

[69] J. Ye and M. C. Rocco. Particle rotation in a Couette flow. *Phys. Fluids A*, 4: 220–224, 1992.

[70] Z. Zhang and A. Prosperetti. A second-order method for three-dimensional particle simulation. *J. Comput. Phys.*, 210:292–324, 2005.

[71] Z. Z. Zhang, L. Botto, and A. Prosperetti. Microstructural effects in a fully-resolved simulation of 1,024 sedimenting spheres. In *IUTAM Symposium on Computational Approaches to Multiphase Flow*, volume 81 of *Fluid Mechanics and Its Applications*, 2006.

Chapter 4

Particles in a rotating flow[‡]

In chapter 2 we studied a bubble in solid body rotation. In chapter 3 we considered the spin rate of a particle and its effect on the lift force, mainly numerically. We observed that in solid body rotation the sphere spin rate increases with the particle Reynolds number and affects the lift coefficient. In this chapter a freely rotating sphere in a solid body rotating flow is investigated experimentally. When the density of the sphere is smaller than that of the surrounding fluid, the sphere reaches an equilibrium position in the experimental setup. From this position, drag and lift coefficients are determined over a large range of particle Reynolds numbers ($2 \leq Re \leq 1060$*). The sphere spin rate is recorded. The wake behind the sphere is visualized and appears to deflect strongly when the sphere is close to the cylinder center. In fluids with low viscosity, high sphere spin rates are observed. By comparing numerical results for a fixed, but freely spinning with a fixed non-spinning sphere, the effect of the sphere spin on the lift coefficient is determined. The combination of these results allows for a parametrization of the lift and drag coefficients of a freely rotating sphere as function of the Reynolds number, the particle spin and the location of the particle with respect to the cylinder center.*

4.1 Introduction

The motion of particles in flows is of interest for many chemical, mechanical and environmental engineering applications. Solid particles are often modelled as spheres. Their motion is dictated by drag and lift forces for most flow types.

[‡] To be published as J.J. Bluemink, D. Lohse, A. Prosperetti, and L. van Wijngaarden, *Drag and lift forces on particles in a rotating flow*.

Moreover, understanding sphere behavior can help to understand the behavior of bubbles with surfactants, since they tend to behave more like spheres due to the fact that the zero-shear stress boundary condition on the bubble surface does not apply and a no-slip boundary condition becomes more appropriate as a result of the surfactants. Therefore, in this chapter we discuss the same system as in chapter 2 [24], but instead of considering a bubble, we consider a particle. To the best of our knowledge there are no results available for a sphere in this system in the intermediate Reynolds number range. For a review of the literature in the low-Reynolds number range see § 3.1.

Because of the differences between particles and bubbles as discussed in § 1.2.2, we expect to find different parameterizations for the lift and drag coefficients. Moreover, the equilibrium positions will be less stable since the particle density is quite close to the fluid density for the particles studied. We also expect a qualitative difference in the particle trajectories since a freely rising light sphere displays path instability and will not follow a rectilinear path for a sufficiently high Reynolds number [5, 6, 8, 25]. Bubbles behave in the same way as already noted by Leonardo da Vinci [20]. However the onset is for much larger Reynolds numbers if the bubble is spherical. By analyzing the vorticity field behind a bubble Mougin and Magnaudet [18] showed that the path instability of a bubble is a result of instabilities in the wake. We may expect that the same holds for a particle. In a uniform flow the wake behind a particle is steady and axisymmetric up to $Re \approx 212$. From $212 < Re < 274$ the wake is still steady, but non-axisymmetric, though there is planar symmetry. For $Re > 274$ the wake becomes unsteady and somewhere between $Re = 350$ and 420 the planar symmetry of the wake is lost. From $Re = 800$ the wake displays small scales due to a Kelvin-Helmholtz instability of the separating shear layer [23]. For a more elaborate review of the literature on this topic see § 3.9. For freely moving drops the wake was studied experimentally by Magarvey and Bishop [14, 15]. Instabilities in the wake for spheres fixed in a uniform flow have been investigated in detail numerically [for example 7, 11] and experimentally. In the experimental system we study a free sphere which remains in place mainly due to a balance between buoyancy and drag. It therefore mimics a free rise in a fluid with rotation. The behavior of freely rising and falling spheres described by Jenny et al. [5, 6] is of interest for this situation. In the numerical simulations discussed in this chapter the particle is fixed and therefore not freely rising. Since the numerical simulations are in the regime $Re \leq 200$ and thus below the critical Reynolds number where the particle trajectory of a freely rising sphere deviates from a straight vertical line, we expect no difference between the experimental and numerical results in this regime. When reaching Reynolds numbers above 200 we may expect the dynamics of the particle to change drastically as a result of path instability.

4.2 Direct numerical simulations

4.2.1 Control and response parameters

To simulate a solid body rotation we fix a particle in a domain in which the undisturbed flow is given by (3.15) with the prefactors α and β set equal to 1. The relevant dimensionless numbers in the numerical simulations are the particle Reynolds number Re as defined in (3.1) and the vorticity parameter Sr_ω as defined in (3.10). The vorticity parameter indicates the position of the particle with respect to the axis of rotation. In a linear shear flow the vorticity parameter has the same value as the dimensionless shear rate Sr, defined in (3.18).

As response parameters we will consider the lift and drag coefficients and the particle spin rate. The particle is allowed to spin freely and adopts its torque-free spin rate as discussed in chapter 3 [3]. The drag coefficient C_D and the lift coefficient C_L are obtained by balancing the forces in (1.1) for the x– and y–directions defined by (3.15)

$$\boldsymbol{F}_y = (\rho_p - \rho)V\mathbf{g} + \frac{1}{2}C_D\rho\pi R^2\boldsymbol{U}^2, \tag{4.1}$$

$$\boldsymbol{F}_x = \rho V C_L \boldsymbol{U} \times (\nabla \times \boldsymbol{U}) + \rho V(C_A + 1)\boldsymbol{U}\cdot\nabla\boldsymbol{U}, \tag{4.2}$$

where ρ_p and ρ are the sphere and fluid densities, V and R the sphere volume and radius, C_A the added mass coefficient ($C_A = 1/2$ for a sphere), $\mathbf{g}$ is the acceleration due to gravity and $\boldsymbol{U}$ the undisturbed fluid velocity. The history force vanishes, since the sphere is fixed and the drag and lift coefficients are calculated after a steady state has been reached.

4.2.2 Previous work

Most DNS results for lift and drag have been obtained for particles in a linear shear flow. Dandy and Dwyer [4] simulated a fixed non-rotating sphere in a linear shear flow at different shear rates and found that the lift coefficient is insensitive to Re for $40 \leq Re \leq 100$. As indicated in chapter 3 the particle spin rate influences the lift force, so it is of interest to study a spinning sphere. Lin, Peery, and Schowalter [13] calculated for a simple shear that the torque-free spin rate of a sphere decreases with increasing inertial effects (see also (3.4)). Rubinov and Keller [21] calculated lift and drag of a spinning sphere in a uniform flow at small Reynolds number, accurate in terms of $O(Re)$. They found for the lift, to this order, $\rho\pi R^3\Omega \times U$, which gives, with our definition of C_L (see 3.14) or (4.2)), for the spin-induced lift $C_{L,Mg}$ (a Magnus-like lift)

$$C_{L,Mg} = \frac{3}{8}\frac{\Omega_P}{\omega}. \tag{4.3}$$

Kurose and Komori [9] simulated a rotating sphere in a linear shear flow and considered the effects of fluid shear and particle spin rate for $1 \leq Re \leq 500$. They found a change in the sign of the lift coefficient for non-rotating spheres at $Re = 60$, with the lift force acting from the low-fluid-velocity side to the high fluid-velocity-side below $Re = 60$. Furthermore they found that the lift and drag coefficients are affected by the fluid shear and particle spin. At high Reynolds numbers they could not separate the lift force into a part due to shear and a part due to sphere spin, in their view since the flow separation is strongly affected by both shear and rotation. It should be noted that their sphere spin rate was imposed. Bagchi and Balachandar [2] allow the sphere to rotate freely (in such a way that it reaches a torque-free spin rate) and in contrast found that they could decouple the Magnus-like lift (due to particle spin) and the shear-induced lift in the range $0.5 \leq Re \leq 200$, i.e.,

$$C_L(Re, Sr, \Omega_P) = C_L(Re, Sr = 0, \Omega_P) + C_L(Re, Sr, \Omega_P = 0). \tag{4.4}$$

Here $C_L(Re, Sr, \Omega_P)$ is the lift coefficient of a freely spinning sphere in a shear flow with dimensionless shear rate Sr, $C_L(Re, Sr = 0, \Omega_P)$ the lift coefficient of a sphere in a uniform flow with imposed spin rate Ω_P (the torque-free spin rate that the sphere would attain in a shear flow with Sr) and $C_L(Re, Sr, \Omega_P = 0)$ the lift coefficient of a non-spinning sphere in a shear flow with Sr. They approximated the Magnus-like lift due to the shear-induced spin by

$$C_L(Re, Sr = 0, \Omega_P) \approx 0.55 \frac{3}{8} \frac{\Omega_P}{\omega}. \tag{4.5}$$

As indicated by Bagchi and Balachandar [2] this decoupling is possible when the particle spins freely. The lift effects behave linearly in this case up to a much higher Reynolds number. They expect the decoupling to be valid over a Reynolds range much wider than they considered.

Bagchi and Balachandar [1] also simulated a sphere rotating freely in a solid body rotating fluid. However, as shown in chapter 3, their results for particle rotation and their lift coefficients are different from the results we find.

4.2.3 Results: DNS results for solid body rotation

Numerical results for light particles in solid body rotation were obtained with the DNS method Physalis [26], a combination of a finite difference and a spectral method [see 26]. For details on resolution and domain size, see § 3.4. Both non-rotating spheres and freely rotating spheres were simulated.

Figure 4.1 shows the drag and lift coefficients as function of the Reynolds number, with the vorticity parameter $Sr_\omega = 0.1$. The numerical data for the drag coefficient (figure 4.1a) show good agreement with the standard drag curve, even though the flow is not uniform. For $Re = 100$ and 200 the data deviate slightly, possibly because the simulations are somewhat under-resolved for these Reynolds numbers.

The lift coefficient is much more sensitive to numerical details than the drag coefficient. Since there are not many data points with which we can compare our results for a sphere in this rotating system, a finite volume code, called "Jadim" [12, 17], was used to validate the Physalis results by simulating non-rotating spheres. For details on the method, see [12, 17]. $100 \times 56 \times 34$ nodes were used. Both methods yield comparable results for the lift coefficient of a non-rotating sphere (open symbols in figure 4.1b), indicating that the Physalis results for non-rotating spheres are reliable. The Physalis data for a non-rotating sphere were fitted by:

$$C_{L,nrs} = 0.51 \log_{10} Re - 0.22 \qquad \text{for} \qquad 5 \leq Re \leq 200, \tag{4.6}$$

with $C_{L,nrs}$ the lift coefficient for a non-rotating sphere.

For freely rotating spheres the lift coefficient is higher because a Magnus-like contribution is added due to the sphere spin. The normalized spin rate as a function of Re is fitted as in figure 3.9

$$\frac{\Omega_P}{\omega} = 1 + 0.0045\ Re \qquad \text{for} \qquad Re \leq 200. \tag{4.7}$$

Adding the Magnus-like lift to the lift coefficient for non-rotating spheres should result in the lift coefficient for spinning spheres, if the effects behave linearly as indicated in (4.4). In a similar fashion as (4.5) the data in figure 4.1b show that a good fit for the spinning spheres is obtained if a contribution for the Magnus-like lift of

$$C_L(Re, Sr_\omega = 0, \Omega_P) \approx 0.5 \frac{3}{8} \frac{\Omega_P}{\omega} \approx \frac{3}{16} \frac{\Omega_P}{\omega} \qquad \text{for} \qquad Re \leq 200 \tag{4.8}$$

is added. The lift coefficient then depends on Re as

$$C_L = C_{L,nr} + \frac{3}{16} \frac{\Omega_P}{\omega} = 0.51 \log_{10} Re - 0.22 + \frac{3}{16}(1 + 0.0045 Re). \tag{4.9}$$

The thick solid line in figure 4.1b represents (4.9). The thinner line above is the same fit with (4.5) instead of (4.8) to model the contribution of the Magnus-like lift. The numerical data for a freely rotating sphere in figure 4.1b show good agreement with (4.9). We can therefore conclude that in the range $5 \leq Re \leq 200$ and for sufficiently low Sr_ω the effects of the Magnus-like lift and the lift induced by the flow can be decoupled in the same fashion as (4.4) for this rotating system. We also find that the factor with which the Magnus-like lift should be multiplied before it is added to the flow-induced lift is very close to that found by Bagchi and Balachandar [2] for the linear shear flow.

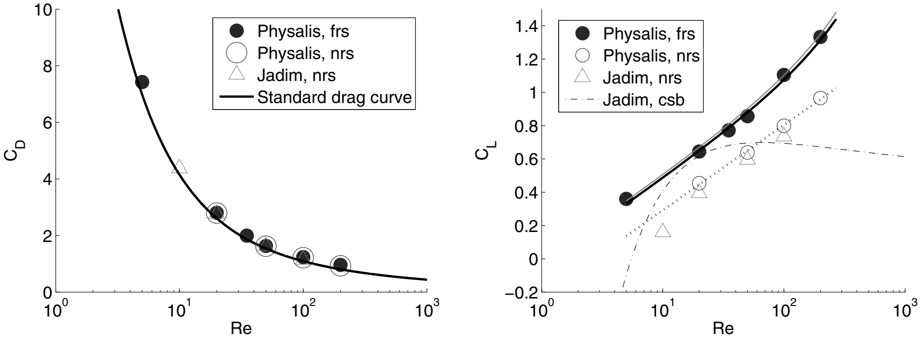

(a) (b)

Figure 4.1: Numerical results for C_D and C_L obtained with two different numerical codes. $Sr_\omega = 0.1$ for all cases. The abbreviations 'frs', 'nrs' and 'csb' stand for freely rotating sphere, non-rotating sphere and clean spherical bubble. (a) Drag coefficient versus Reynolds number. (b) Lift coefficient versus Reynolds number. The dotted line is the fit (4.6) through the Physalis data of a non-rotating sphere. The solid line is the combination (4.9) of the previous fit (4.6) and the contribution due to the Magnus-like lift (4.8). The thinner line just above is a similar combination of fits with the prefactor (4.5) of Bagchi and Balachandar [2] for the Magnus-like lift. The fit for a clean spherical bubble is taken from [16].

The dash-dotted line in figure 4.1b represents a fit of the data of Magnaudet and Legendre [16] for a clean spherical bubble in solid body rotation. It is clear that these curves show a completely different trend. Since the bubble cannot deform this difference is solely due to the difference in boundary conditions at the surface.

4.3 Experiments

4.3.1 Control parameters

The governing parameters of the experimental system (the same as in chapter 2, but now for a particle instead of a bubble) are the gravitational acceleration **g**, the liquid viscosity ν, the liquid density ρ, the particle density ρ_p, the particle radius R and the cylinder angular velocity ω. Three dimensionless groups can be formed from these parameters

$$Ta = \frac{2R^2\omega}{\nu}, \qquad Ga = \frac{2R\sqrt{2R(1-\rho_p/\rho)g}}{\nu}, \qquad \frac{\rho_p}{\rho}, \tag{4.10}$$

in which Ta is the Taylor number, Ga the Galileo number and ρ_p/ρ the density ratio. Note that the Galileo number and the density ratio are the dimensionless control parameters in the system of a freely falling and rising sphere studied by Jenny et al. [5, 6]. Their observations may thus be relevant for our system.

The outputs of the experimental system are the equilibrium position of the sphere (r_e, ϕ_e) and its spin rate Ω_P. The equilibrium position allows us to determine the lift and drag coefficient. The spin rate is measured since it has a significant influence on the lift coefficient as was shown in chapter 3 and in § 4.2.3.

The relationship between the equilibrium position of the sphere and the lift and drag coefficient is obtained by solving the equation of motion (2.1) for particles. We find in close correspondence to (2.14) and (2.15)

$$\tan\phi_e = \frac{8}{3}\frac{R}{C_D r_e}(2C_L - 1 - C_A), \tag{4.11}$$

$$r_e = -\frac{g(\rho-\rho_p)\sin\phi_e}{\rho\omega^2(2C_L - 1 - C_A)}. \tag{4.12}$$

The difference between (2.14), (2.15) and (4.11), (4.12) is that for a solid sphere the densities of the fluid and the sphere play an important role, since the sphere density ρ_p is non-zero.

Equations (4.11) and (4.12) can be solved to see the effect of the control parameters on the equilibrium radius r_e of the particle. If the drag coefficient is estimated by $C_D = 24/Re$, r_e can be expressed as:

$$r_e = \frac{R^2(\rho-\rho_p)g}{\rho\omega\sqrt{81/4\nu^2 + R^4\omega^2(2C_L - 1 - C_A)^2}}. \tag{4.13}$$

For very viscous fluids, $\nu >> R^2\omega$, we find that the distance of the particle from the cylinder center depends on the cylinder rotation rate as

$$\frac{r_e}{R} \sim \frac{(1-\rho_p/\rho)gR}{9/2\nu}\frac{1}{\omega}, \tag{4.14}$$

whereas for fluids with a low viscosity

$$\frac{r_e}{R} \sim \frac{(1-\rho_p/\rho)g}{R(2C_L - 1 - C_A)}\frac{1}{\omega^2}. \tag{4.15}$$

The dependence of the drag coefficient C_D and the lift coefficient C_L on r_e and ϕ_e is (rewriting (4.11) and (4.12))

$$C_L = \frac{1}{2}\left[1 + C_A - \frac{\rho - \rho_p}{\rho}\frac{g\sin\phi_e}{r_e\omega^2}\right]. \tag{4.16}$$

$$C_D = -\frac{8}{3}\frac{\rho - \rho_p}{\rho}\frac{R_b}{r_e^2 w^2} g\cos\phi_e. \tag{4.17}$$

The undisturbed velocity at the particle center is

$$U_0 = \omega r_e. \tag{4.18}$$

As a result the equilibrium radius r_e enters the Reynolds number and the Froude number

$$Re = \frac{2RU_0}{\nu} = \frac{2Rr_e\omega}{\nu}, \qquad Fr = \frac{U_0^2}{2Rg} = \frac{r_e^2\omega^2}{2Rg} \tag{4.19}$$

and a vorticity parameter

$$Sr_\omega = \frac{2\omega R}{U_0} = \frac{2R}{r_e}. \tag{4.20}$$

4.3.2 Experimental setup

In an experiment a sphere is inserted in a horizontal cylinder filled with a liquid. The cylinder has a radius is 250 mm and a length of 500 mm. Its wall and end caps are made of 15 mm thick Plexiglas. Two steels rods support the cylinder, a third rod is mounted above it. The rods have a rubber coating such that there is no slip between the rods and the Plexiglass wall when rotating. One of the rods is connected to an AC servo motor by a belt and drives the rotation. The cylinder rotates anti-clockwise with frequencies between 0 and 2 Hz, the rotation rate can be set precisely. The cylinder can be pivoted to an almost upright position for filling purposes. For the definition of the coordinates see also figure 3.1a. The cylinder is set into rotation and some time is allowed to reach a steady-state.

The sphere position is determined by making a shadow on a screen (an opal diffusing glass plate of 200 mm by 250 mm). For this purpose a narrow laser beam is widened into a parallel beam with a diameter of about 8 cm. The beam passes through the cylinder, creating a bright spot on the screen located at the other side of the cylinder (figure 4.2). A grid with 1 cm spacing is attached to the screen. The shadow of the particle on the grid is recorded with a camera with a frame rate of 50 frames per second. The camera is connected to a computer. The position of the particle's shadow with respect to the grid is determined by image analysis. The

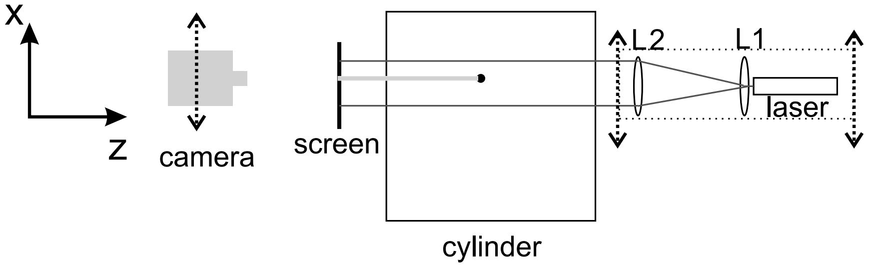

Figure 4.2: Top view of the optical parts of the experimental setup. L1 is a lens with f = 10 mm, L2 with f = 1000 mm.

cylinder center is determined by recording marks on the end caps of the cylinder for the duration of a full rotation. The marks trace a circle during the full rotation and the centers of the circles are determined by image analysis to obtain the centers of the end caps with respect to the grid. Measuring the location of the sphere along the cylinder axis and linear interpolation between the centers of the end caps provides the position of the cylinder center at the axial plane of the sphere, thus correcting for misalignment between the laser and cylinder axis.

To cover a wide range of Reynolds numbers, nine mixtures of glycerin and water with different viscosities were prepared. Table 4.1 shows the different liquids, together with the mass percentage of glycerin. It also shows the kinematic viscosity, the fluid density and the Reynolds range covered by each liquid. For the viscosity measurement several U-tube and Ubbelohde viscometers were used. For the density measurement a pycnometer was used. For some liquids two different viscosities are indicated in table 4.1. This is a result of measuring at different temperatures. The temperature was monitored and recorded during the experiment and the viscosity of the fluid was determined at the same temperature.

To obtain a minimum excursion around the equilibrium position, a sphere with a density much lower than water is the best choice. However, such spheres are generally hollow and have an unequal mass distribution or they are manufactured in such a way that the sphericity is not assured. To have good sphericity and mass distribution, low-density polyethylene (LDPE) spheres with a density ratio of $\rho_p/\rho_{water} \approx$ 0.93 were used. For the viscous fluids ρ_p/ρ is smaller than for water (since these fluids have a higher density). As a result the equilibrium position is more stable for the lower numbered liquids in table 4.1. The sphere radius is 3.969 mm. To determine the spin rate, the sphere is marked and its spin is recorded by a video camera. For the experiments in water (liquid 9 in table 4.1) the behavior of a second sphere with a radius of 3.175 mm was studied. However the spin rates were not measured. Measurements for this sphere are indicated by open triangles

Liquid #	% glycerin (by weight)	ν $\mathrm{mm}^2\ \mathrm{s}^{-1}$	ρ_l $\mathrm{g\ cm}^{-3}$	Re-range	Symbol in figures
1	89	170.1	1.232	1.8 - 1.9	□
2	85	91.1, 86.0	1.222	5.2 - 5.5	▲ and △
3	80	55.2	1.211	11.0 - 11.5	■
4	75	28.1	1.194	24.7 - 29.9	◊
5	68	15.4	1.174	59.9 - 68.0	►
6	60	9.3	1.154	107 - 127	♦
7	48	4.5, 4.8	1.121	234 - 297	▼ and ▽
8	30	2.3	1.071	450 - 574	★
9	0	0.98	0.997	687 - 1060	◄ and ◁

Table 4.1: Properties of the experimental liquids.

pointing to the left ($\triangleleft$).

The experimental procedure consists of filling the tank with one of the fluids of table 4.1 and inserting the sphere. Bubbles initially remaining in the cylinder are removed by tilting the tank somewhat and rotating it slowly. The bubbles drift to the front side of the cylinder where they can be removed at an air-inlet by adding fluid. When the tank is completely filled with fluid, the cylinder is tilted back to its horizontal position and set into rotation. Waiting times of 10 minutes up to 1 hour (for the highly viscous fluids) may be needed for spin up of the fluid (see also § 3.3) and to allow a particle to reach its equilibrium position and torque-free spin rate.

An analysis of the systematic error by means of error propagation of the errors in r_e, ϕ_e, ρ_b, R, ρ_l, ν and ω, shows that for the liquids with high viscosity the measurement uncertainty of the lift coefficient is very high. The error in the measurement of the position is estimated to be one millimeter in the x-direction and half a millimeter in the y-direction for the experiments where the particle displays only tiny excursions from its equilibrium position. For the measurements where the sphere moves around its equilibrium position, the error in position was estimated to be a few millimeters in both directions. An error in the angle $\Delta\phi_e$ propagates strongly in the error of the lift coefficient. The error in the drag coefficient depends more strongly on the relative error in the radial distance from the cylinder center $\Delta r_e/r_e$. In table 4.2 an indication of the measurement uncertainty for each liquid is shown. The values are a good representation for the measurement uncertainty of most data points. However, those data points for which the radius of the trajectory executed by the sphere is large and for which simultaneously the particle equilibrium position is located close to the cylinder center, may have larger uncertainties.

Liquid #	Re	Sr_ω	C_D	C_L
1	4%	2%	5%	>100%
2	3%	1%	4%	50%
3	4%	1%	4%	20%
4	4%	2%	5%	10%
5	4%	1%	3%	10%
6	10%	1%	3%	10%
7	4%	1%	4%	10%
8	4%	2%	4%	10%
9	3%	2%	4%	10%

Table 4.2: Order of magnitude of the uncertainties for the different liquids.

4.3.3 Results: Particle trajectories

Figures 4.3, 4.4, 4.5 and 4.6 show particles trajectories in liquids 4, 7, 8 and 9. For the definition of the xy-plane, see figure 3.1a. In the figures the cylinder rotation frequency f_c and the Reynolds number Re are indicated for each trajectory. Figure 4.3 is a typical representation of the behavior of the sphere in liquids 1–6. In these liquids the sphere remains more or less steady in its equilibrium position. In some cases it makes a larger excursion around its equilibrium. However, the trajectory it traces is very regular and this suggests that the sphere has not yet settled into its equilibrium position. A longer waiting time should have been allowed for these cases.

Figure 4.4 represents the trajectories in liquid 7 and shows the transition of the sphere resting in its equilibrium position (for the higher cylinder frequencies) to a somewhat erratic path around it (for the lower cylinder frequencies). For $Re \leq 274$ the trajectories are regular and most of the time the radius of the trajectory is much smaller than the particle radius. For $Re \geq 283$ the trajectories become irregular and their radii are larger. Allowing a longer waiting time has no effect on the trajectory, the path remains erratic. The qualitative change in trajectories occurs between Re = 274 and Re = 283. Since this is close to the critical Reynolds number (where a particle in a quiescent fluid stops rising in a rectilinear motion and starts displaying spiralling or zigzagging motion), the change in trajectories is most likely connected to path instability (see § 4.1).

For liquids 8 and 9 ($Re \geq 450$) (figures 4.5 and 4.6) Re is everywhere above the critical Reynolds number. Indeed, we observe that the particle is no longer fixed

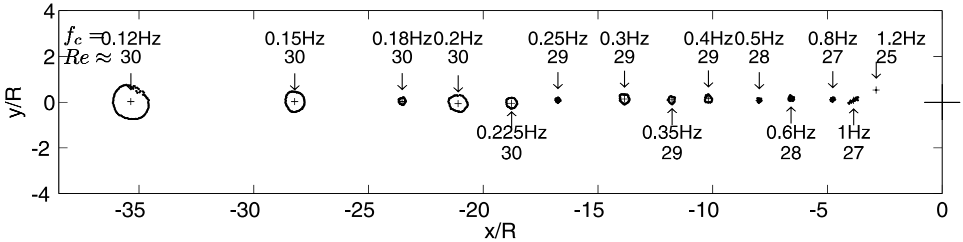

Figure 4.3: Particle trajectories for a sphere in liquid 4 (table 4.1) in the xy-plane. The cross at (0,0) is the cylinder center. The position is normalized by the radius of the sphere. For each trajectory the cylinder rotation frequency f_c and the Reynolds number Re are indicated.

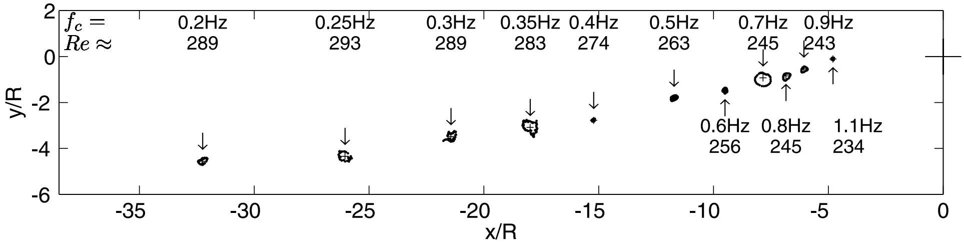

Figure 4.4: As figure 4.3 but for liquid 7.

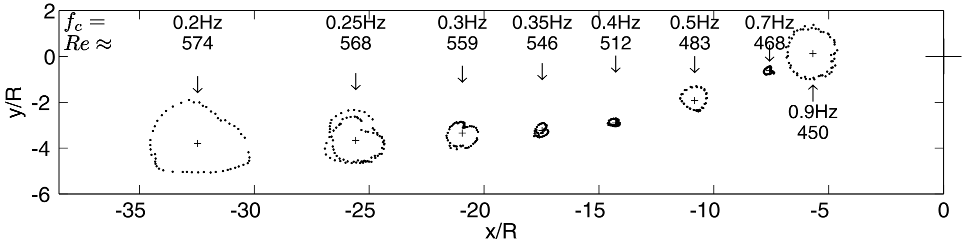

Figure 4.5: As figure 4.3 but for liquid 8.

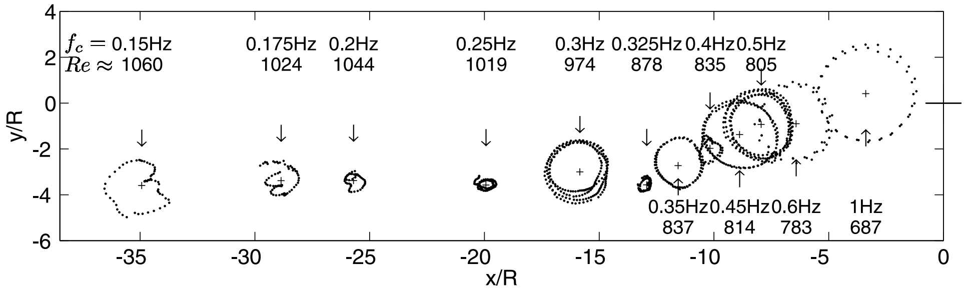

Figure 4.6: As figure 4.3 but for liquid 9.

at an equilibrium position, but moves in an erratic way around it. The motion in the z– (axial) direction is minor compared to that in the xy–plane. In a quiescent fluid the deviation from the rectilinear rising motion due to path instability is oriented in the plane perpendicular to the gravitational acceleration (here the y-direction). For the present rotating system, the sphere motion is not mainly oriented in the plane perpendicular to the gravitational acceleration nor in the plane perpendicular to the centripetal acceleration. It is principally in the xy–plane shown in figures 4.5 and 4.6, i.e. the plane spanned by the gravitational and the centripetal acceleration.

When the sphere is close to the cylinder center (i.e. the vorticity parameter is high) its trajectory is no longer erratic but forms a regular reproducible circle. When the particle is traced for several periods, the path it follow overlays itself. The circle travelled by the particle has a very large radius. We define the effective equilibrium position as the center of the trajectory. This center is determined by taking the average over a complete cylinder rotation (the time needed for a full cylinder rotation equals the time needed for the sphere making a full circle around its effective equilibrium position, i.e. the cylinder rotation frequency and the sphere excursion frequency are the same for the regular trajectories). The averaging over the sphere trajectory is appropriate for the small trajectories or the trajectories that are located sufficiently far from the cylinder center. However, for the large circular trajectories close to the cylinder center it is unclear what flow field is seen by the particle. As a result the data with a high vorticity parameter are less reliable.

4.3.4 Results: PIV images of the wake of the sphere

The particle behavior discussed in § 4.3.3 may be a result of the wake structures behind the sphere. Since the sphere is held in its equilibrium position merely by a balance of forces, the situation is similar to a freely rising sphere. We expect to encounter the analogs of path and wake instability as discussed in § 4.1. However, due to the rotation, the instabilities may be different from a freely rising sphere in a quiescent fluid. It is therefore of interest to study the wake behind the sphere in the solid body rotating flow.

Sakamoto and Haniu [22] studied the wake of a fixed particle in a linear shear flow. They found that at the appearance of vortex shedding vortex loops are detached always on the high fluid velocity side. In contrast to a uniform flow without shear, where the detachment point of the vortex loop alternates. They attribute this one-sided detachment of the vortex loops to the faster growth of the vortex on the high-fluid-velocity side compared to that on the low-fluid-velocity side. As a result the vortex on the high-fluid-velocity side continues to grow while taking in the vorticity of the surrounding shear layer. Furthermore they noted that the vortex shedding frequency increases with the shear when $Sr > 0.05$. The Reynolds number above which vortex shedding occurs is lowered by shear.

The flow around a sphere in solid body rotation is not symmetric and contains higher fluid velocity on one side of the sphere as in linear shear flow. We may therefore expect also in solid body rotation changes regarding the onset of instability as well as changes in vortex shedding frequency.

To visualize the flow around the particle, the fluid (water) was seeded with hollow glass spheres with a diameter of 15 μm. The wake of a sphere in the xy-plane was visualized by standard PIV measurements at cylinder rotation frequencies of 0.2 Hz, 0.5 Hz and 1.0 Hz. The resulting flow fields (indicated by arrows) and vorticity fields (indicated by colors) can be seen in figures 4.7, 4.8 and 4.9. Vortices appear to be shed on both sides, but the shedding on the high-fluid-velocity side is more pronounced. From the PIV results we cannot conclude with certainty that vortex shedding occurs solely in the xy–plane. However, since the circling motion in the xy–plane discussed in § 4.3.3 is much more pronounced than the motion in the z–plane, we may expect that the vorticity of the flow causes the shedding to occur mainly in one plane, instead of varying in orientation.

In figure 4.10 the shedding process can be seen in more detail. We see the first image reproduced in the fourteenth, indicating that the shedding process has a frequency of about 4 Hz. The first vortex is shed from the low-fluid-velocity side (image 10) and the one at the high-fluid-velocity side follows directly after (image 13). The shedding process is less clear for the higher cylinder frequencies. For the cylinder frequency (f_c) of 0.5 Hz it was estimated to be 3.85 Hz. The Strouhal number is defined as

$$St = \frac{2Rf}{U_0}, \tag{4.21}$$

where f is the vortex shedding frequency. For a cylinder rotation frequency of 0.5 Hz $St = 0.4$, whereas for $f_c = 0.2$ Hz, the same shedding frequency yields $St = 0.15$. This indicates a decrease of St with decreasing f_c and increasing Re (since

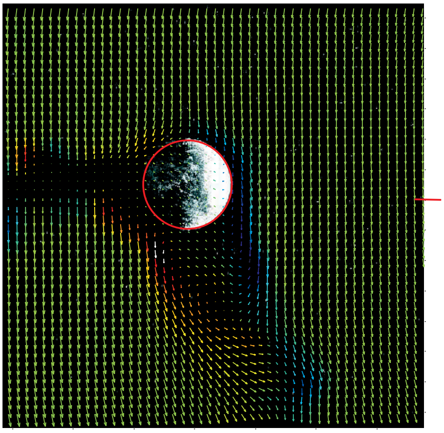

Figure 4.7: Flow field (indicated by arrows) and vorticity (indicated by colors, green represents zero vorticity). The red line indicates the vertical position of the cylinder center, the center is out of sight for this image. The high fluid velocity side is on the left side of the sphere. The sphere diameter is 6 mm, the cylinder rotation frequency is 0.2 Hz. $Re \approx 900$, $Sr_\omega \approx 0.05$. The vortex shedding frequency is about 4 Hz.

Re increases with decreasing f_c ((4.15), (4.18) and (4.19)). In a uniform flow St increases with Re. However, in our rotating system, the vorticity parameter decreases with increasing Re. The high dimensionless vorticity at lower Re is probably the cause of a higher value of St for $f_c = 0.5$.

The differences with Sakamoto and Haniu [22] with respect to the detachment location of the vortices may be a result of the fact that our particle is not truly fixed. Due to the sphere spin, there is a higher relative velocity on the low velocity side, which may destroy the one-sided vortex shedding. An other difference with the linear shear flow is the cross-stream shear component present in the solid body rotation. As was shown in chapter 3 this component can change the behavior of the sphere drastically.

Another interesting aspect of figures 4.7, 4.8 and 4.9 is the deflection of the wake. The sphere may interact with its own wake when the wake is advected downstream and reaches the top of the sphere after one revolution of the cylinder, see figure 4.11a. In this case it is as if there is a sphere located upstream of the sphere under consideration as shown at the right of figure 4.11a. Wake interaction may arise provided that the wake has not diffused completely after one rotation and it is not deflected substantially towards the cylinder center.

We address first the wake diffusion and estimate for which set of parameters

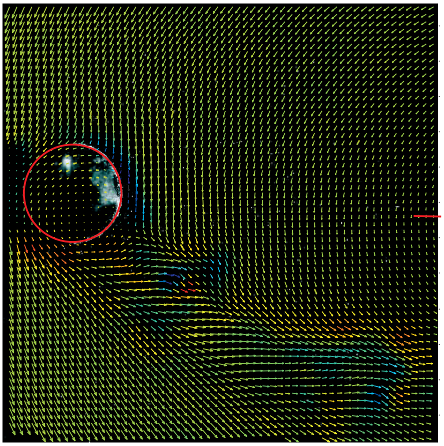

Figure 4.8: As figure 4.7 but now for a sphere diameter of 8 mm and at a cylinder rotation frequency of 0.5 Hz. $Re \approx 600$, $Sr_\omega \approx 0.33$. The vortex shedding frequency is about 3.8 Hz.

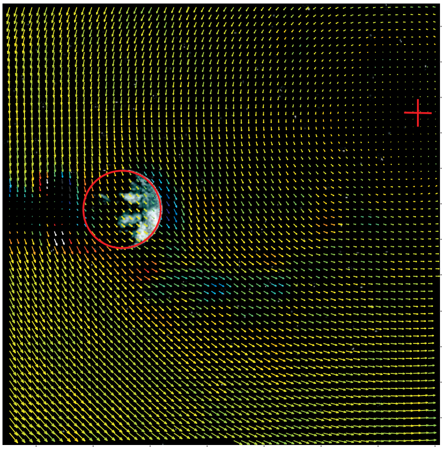

Figure 4.9: As figure 4.7 but at a cylinder rotation frequency of 1.0 Hz. $Re \approx 360$, $Sr_\omega \approx 0.67$. The vortex shedding frequency could not be determined. The red cross indicates the cylinder center.

the wake length is such that it can interact with the sphere in the next revolution. The velocity defect v_s in the wake is [10]

$$v_s = \frac{F_D}{4\pi\rho\nu s}, \tag{4.22}$$

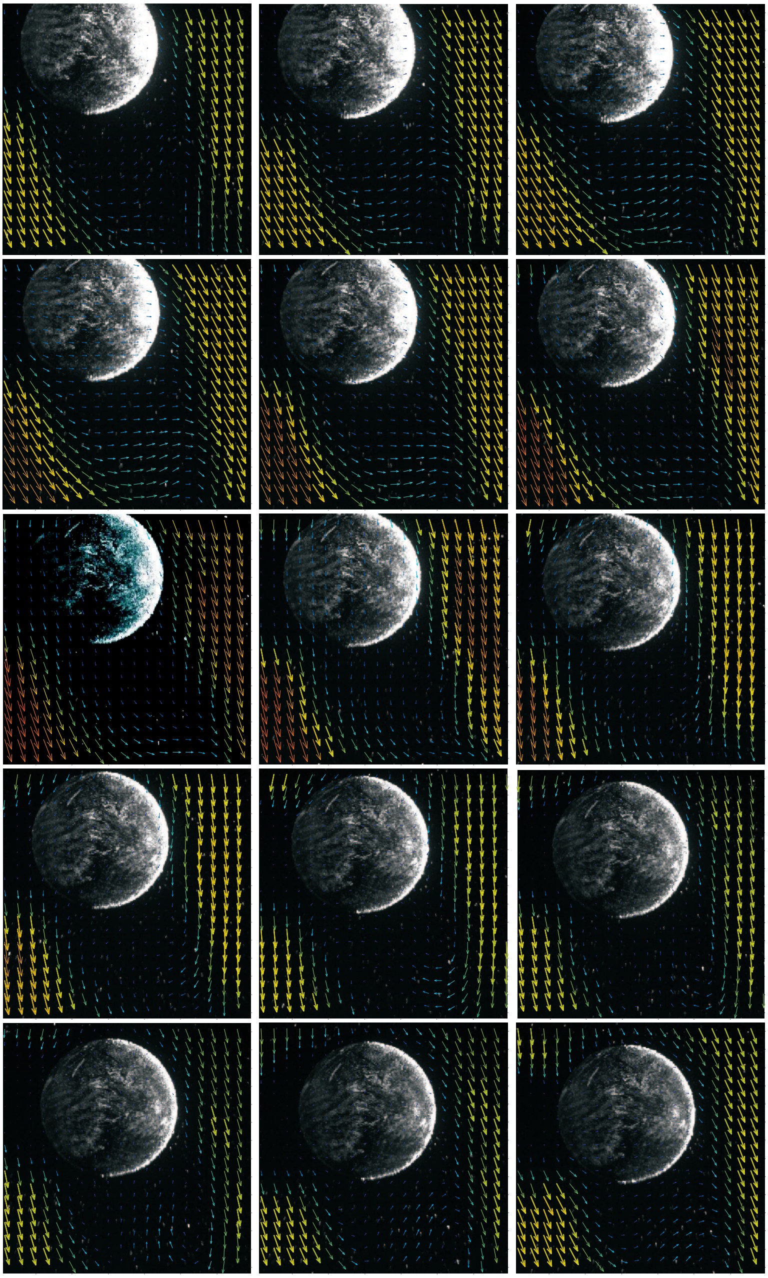

Figure 4.10: Sequence of PIV images for $f_c = 0.2$ Hz, 6 mm diameter LDPE sphere. The arrows indicate the flow field, the color of the arrows is a measure of the magnitude of the velocity. From the second to the last image one cycle is completed, consecutive frames are 0.02 s apart. The vortex shedding frequency is about 4 Hz.

where s is the coordinate in the direction of the wake and F_D the drag force. After a full rotation $s = 2\pi r_e$ and for no wake interaction the velocity defect should be much less than the velocity of the undisturbed incident flow ωr_e. This holds when

$$\frac{C_D}{16\pi}\frac{R^2\omega}{\nu} \ll 1. \tag{4.23}$$

As a result we may expect wake interaction due to the rotation of the fluid when

$$\frac{\omega R^2}{\nu} \sim O(1). \tag{4.24}$$

For the last 4 liquids in table 4.1 $\frac{\omega R^2}{\nu} \geq 1$ for most rotation rates and thus wake interaction as indicated in figure 4.11a may be present.

Although the wake may survive a full cylinder revolution, it will reach the top of the sphere only in some cases. This is due to the pressure gradient caused by the cylinder rotation which deflects the wake towards the cylinder center. From the momentum equation in radial direction ($\frac{\partial p}{\partial r} = \rho \frac{u_\theta}{r}$, with p the pressure and r and θ the radial and tangential directions) we see that to maintain the pressure gradient, the trajectory of the retarded fluid in the wake adopts a smaller radius. As a result the wake is deflected towards the cylinder center. In figure 4.11 on the left side a sketch of this deflection for different sphere positions is shown. For a sphere far away from the cylinder center as in figure 4.7 (and sketch in figure 4.11b), the Reynolds number is high and the wake is long. It is not deflected very strongly. In figure 4.8 (sketch in figure 4.11c) we see a stronger deflection. For even higher rotation rates, figure 4.9 (and sketch in figure 4.11d) shows that the wake is very strongly deflected toward the center of the cylinder.

At the right of figure 4.11 the effect of the wake on the sphere in the next revolution is sketched. Case (a) is hypothetical: the wake survives a full rotation and is not deflected at all. As a result the sphere feels its own wake as if it were the wake of a sphere upstream of it. In case (b) the wake also survives a full revolution, but now is slightly deflected. As a result the sphere will not feel its own wake. For a higher cylinder frequency as in (c) the wake is deflected more. The wake is shorter because the particle Reynolds number is lower at higher rotation frequencies. However, the path over which the wake may decay is also shorter. It is as if the two spheres in the representation at the right of figure 4.11 were closer. In this case interaction occurs. For the last situation the deflection is too strong for interaction. What determines the limits between the different cases is unclear. Above discussion serves merely to indicate possible wake-interaction scenarios, relevant for the interpretation of some of the data in the next sections.

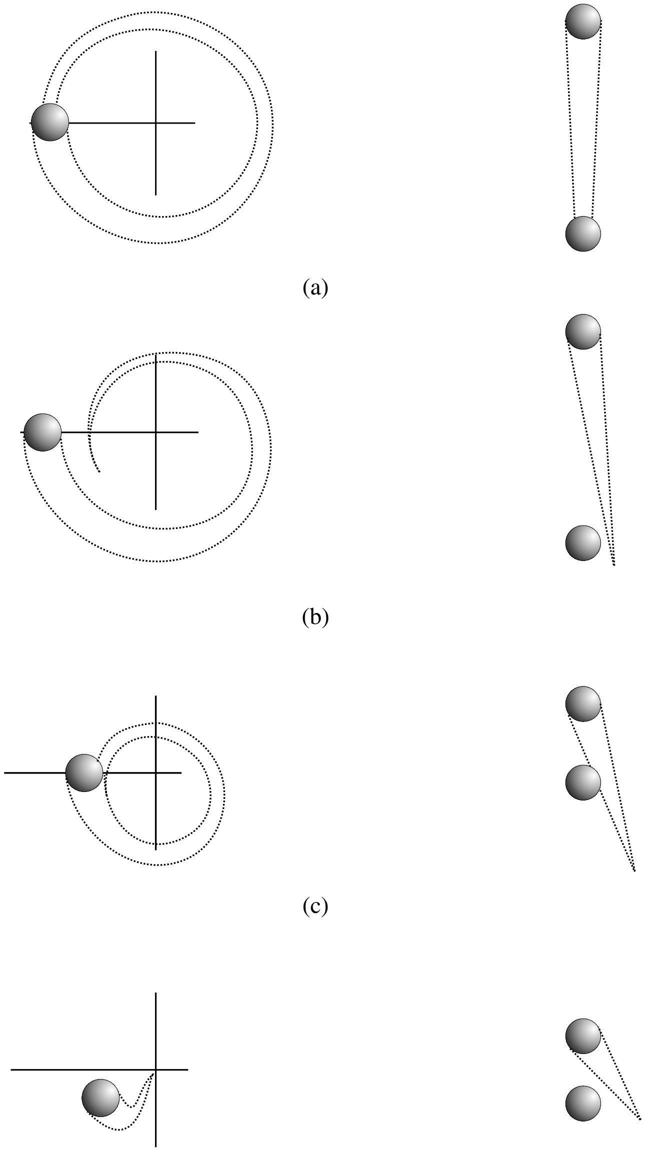

(a)

(b)

(c)

(d)

Figure 4.11: Left: sketch of the wake behind the sphere. (a) The trajectory of the wake for the hypothetical case where no deflection of the wake occurs. Particle equilibrium position (b) far from the cylinder center, (c) at intermediate distance and (d) close to the cylinder center. The crossing of the solid lines denotes the cylinder center. Right: resulting wake interaction after one revolution of the cylinder.

4.3.5 Results: Dependence of lift and drag on the control parameters

This section discusses the dependence of the equilibrium position (r_e, ϕ_e), the drag and lift coefficients and the normalized particle spin rate on the system's control parameters defined in (4.10). In the figures in this and the next section, results for the different liquids can be recognized by the symbols in the last column of table 4.1.

Figure 4.12 shows the dependence of the equilibrium position of the particle on the Taylor number Ta. For each liquid the viscosity is constant and an increase in Ta indicates a higher rotation frequency of the cylinder. As the cylinder rotation rate increases, the radial distance of the particle decreases and the particle finds its equilibrium closer to the cylinder center (figure 4.12a). The equilibrium angle ϕ_e is very close to π for $Ta < 1$ (i.e. for the more viscous fluid mixtures). For liquids 6–9 we see an increase with Ta at first and as Ta increases further, the angle decreases quite sudden for all liquids. However, the peaks for the different liquids do not occur at the same value of Ta.

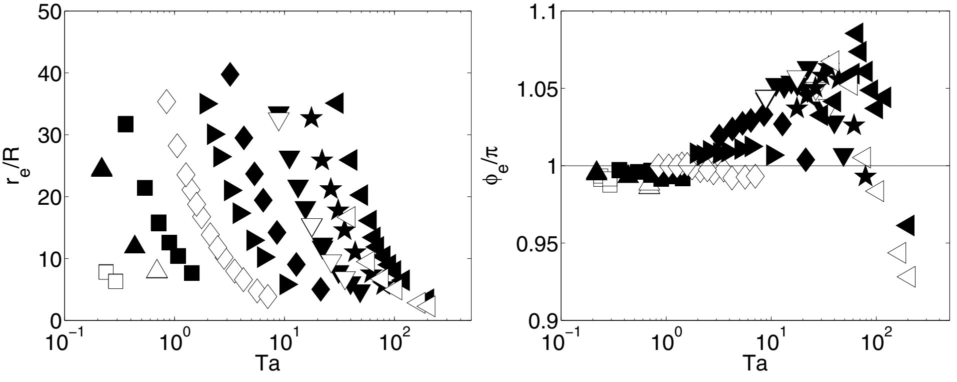

(a) (b)

Figure 4.12: Radial distance of the particle center (a) and angle of line between cylinder center and particle center with respect to the horizontal (b) as a function of Ta.

From (4.16) and (4.17) we see that r_e and ϕ_e are related to the lift and drag coefficients. Therefore we inspect in figure 4.13 the effect of Ta on the lift and drag coefficients, as well as on the particle spin rate. The drag coefficient decreases for each liquid in figure 4.13a since the viscosity decreases. However each liquid data set shows a spread over a large range of Ta and a relatively small range of C_D. The lift coefficient as function of Ta is shown in figure 4.13b and the normalized

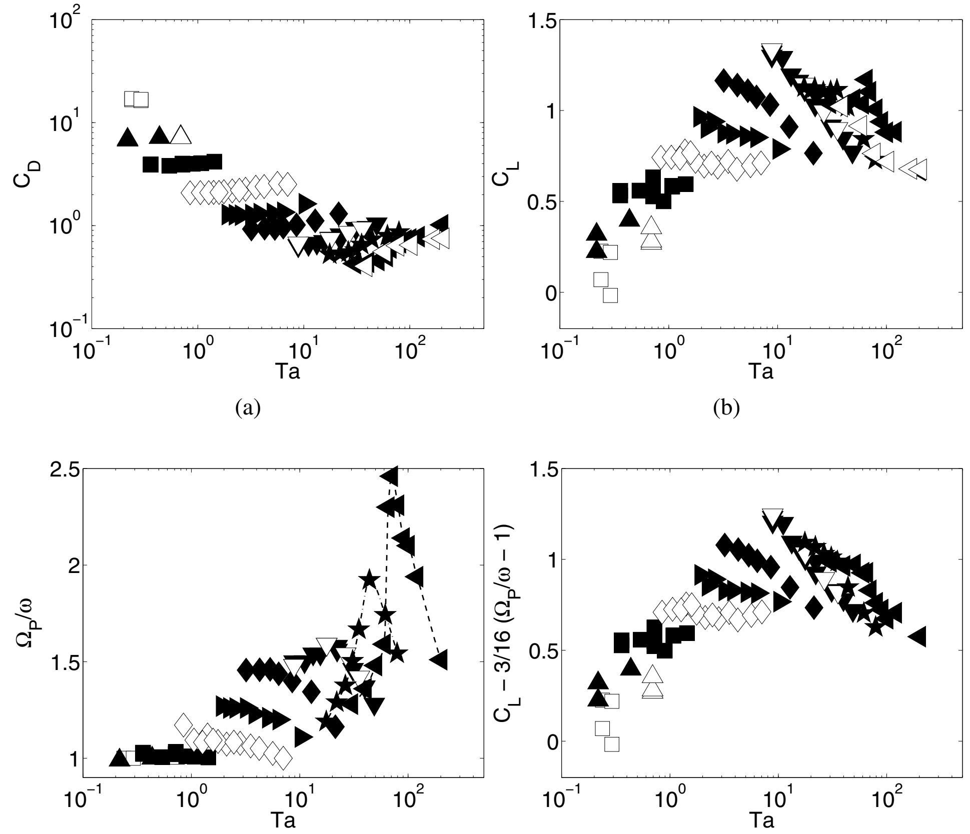

(a) (b)

(c) (d)

Figure 4.13: Drag coefficient (a), lift coefficient (b), normalized particle spin rate (c), and lift coefficient corrected for spin (d) as function of Ta. Dashed and dashed-dotted lines are to guide the eye for the data of liquids 8 and 9.

particle spin rate in figure 4.13c. The normalized particle spin rate shows peaks for liquids 7–9. A relatively small normalized sphere spin rate is observed when Ta (and consequently the cylinder rotation rate) is small for these liquids (note that Ω_P/ω is always above one in this setup unlike some of the data taken in the smaller setup discussed in § 3.3). As a result the particle is located far away from the cylinder center. As the cylinder rotation rate increases and the particle equilibrium position is located closer to the center, the spin rate increases. It then decreases for even higher cylinder rotation rates. This behavior may be a result of the scenarios described in the previous section and sketched in figure 4.11. For sufficiently low

Ta the ratio in (4.24) is small. The particle finds its equilibrium far from the cylinder center. The wake can diffuse over a long trajectory before it reaches the particle again after one rotation and will not interact with the particle. As Ta increases, the particle equilibrium position is located more towards the cylinder center. Now the sphere may interact with the wake as shown at the right side of figure 4.11c. One side of the particle is in the wake, the other in the undisturbed flow. As a result a large torque acts on the sphere. Since the particle reaches a torque-free state, the spin rate will be very high under these circumstances. As Ta increases further and the particle is located even closer to the cylinder center, the wake deflection may be so strong that the particle cannot interact with its wake any more (figure 4.11d). As mentioned before, for spheres very close to the cylinder center the incident flow is unknown, since the incoming flow seen by the particle is disturbed by its own presence.

A high spin rate of the sphere affects the measured lift coefficient. We define an excess spin as

$$\Omega_P/\omega - 1, \tag{4.25}$$

since for Stokes flow the normalized spin rate Ω_P/ω is 1. In figure 4.13d the lift coefficient is corrected for the particle spin, assuming that the extra part of the lift coefficient due to the spin is given by (4.8). By subtracting the part of the lift coefficient due to excess spin we find the corrected lift coefficient $C_L - 3/16(\Omega_P/\omega - 1)$. The high peaks in figure 4.13b are now lowered by this correction. The effect on the lift due to the spin has only been demonstrated for $5 \leq Re \leq 200$. However, we apply (4.8) to the complete experimental data range to see whether it is valid over a wider range. In figure 4.13 we see that the corrected lift coefficients for the liquids with low viscosity fall better onto a straight line than the non-corrected lift coefficients.

Figure 4.14 shows the dependence of the equilibrium position of the particle on the Galileo number Ga defined in (4.10). For each liquid the Galileo number is a constant and the figure shows the spread of r_e and ϕ_e. The effect of Ga on the lift and drag coefficient and the particle spin rate is shown in figure 4.15.

Figure 4.15a shows a decrease of the drag coefficient with Ga. Since the Galileo number is comparable to a Reynolds number (in Ga the velocity is based on the terminal rise velocity, in Re on the undisturbed velocity at the sphere center) this is according to expectation. The lift coefficient in figure 4.15b shows an increasing trend with Ga up to $Ga \approx 206$. After that C_L decreases. This indicates that the highest lift coefficients in liquids 8 and 9 are smaller than in liquid 7. As indicated by Jenny et al. [6] we expect the critical Galileo number for which the particle trajectory becomes unstable to be between 175 and 180 for our density ratios ($\rho_p/\rho \approx 0.9$). The particles in liquids 1–6 should all have axisymmetric wakes. Liquid 7 ($Ga \approx 206$) is in the periodic zigzagging regime. Liquids 8 and 9 are in three-dimensional chaotic regime. The transition to an unsteady wake coincides with a decrease of the lift coefficient. Figure 4.15c indicates that the spread of the rotation rates in the same liquid increases with Ga. Whereas the envelope of the highest values of C_L shows an indentation for liquid 8 in figure 4.15b, this is removed when correcting the lift coefficient for the excess particle spin (figure 4.15d).

In figures 4.16 and 4.17 the results are plotted as function of the density ratio ρ_p/ρ. They show trends similar to those in figures 4.14 and 4.15. As the viscosity of the liquids in table 4.1 decreases, the density ratio increases towards one. For a density ratio larger than one, the equilibrium position is no longer stable, so we can expect that the equilibrium positions become less stable for the less viscous liquids. The effect on the particle trajectories can be seen in figures 4.3–4.6, where the excursions around the equilibrium position are larger as the viscosity decreases. Figure 4.17 shows the trend of the lift and drag coefficient as a function of the density ratio. However, for each liquid both the density ratio and the Galileo number vary. The behavior shown in the figure can thus be a result of a different Galileo number instead of a different density ratio. In fact, the data for the smaller sphere in liquid 9 (◁) fall onto the same range of values of C_D and C_L as the data in liquid 8 (★). The two liquids have a different value for the density ratio, but the same Galileo number. Thus the Galileo number is a more appropriate parameter to describe the results. Apparently, the viscosity is important to describe the drag and lift trends. The representation of the equilibrium position, drag and lift coefficient and spin rate in terms of Ga, Ta and ρ_p/ρ has not revealed simple relationships. From (3.11) we expect

$$\frac{r_e}{R} \sim \frac{Ga}{Ta}. \qquad (4.26)$$

This ratio does not contain the fluid viscosity. In figure 4.18 the equilibrium position as a function of Ga/Ta is shown. The data for r_e/R collapse more onto one curve than when plotted as individual functions of Ta or Ga. However, for increasing values of Ga/Ta the spread becomes extensive. The viscosity influences the results via the drag and lift coefficient. Comparing the results in this section, the equilibrium angle ϕ_e is best described by the Taylor number as in figure 4.12.

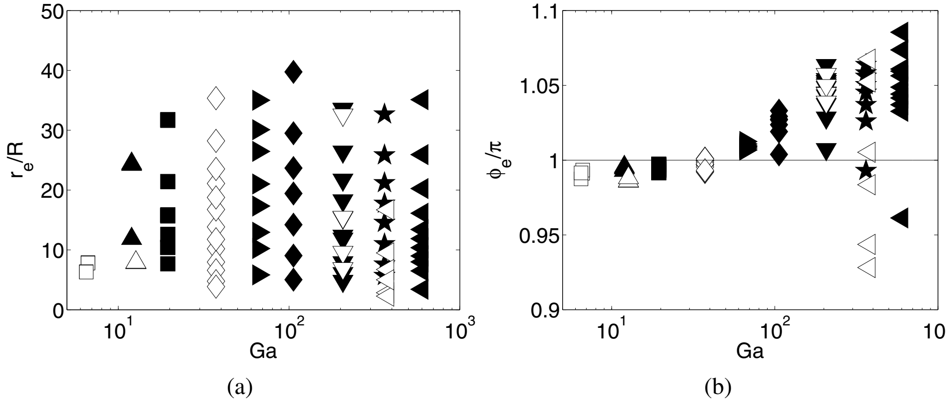

(a) (b)

Figure 4.14: As figure 4.12 but as a function of Ga.

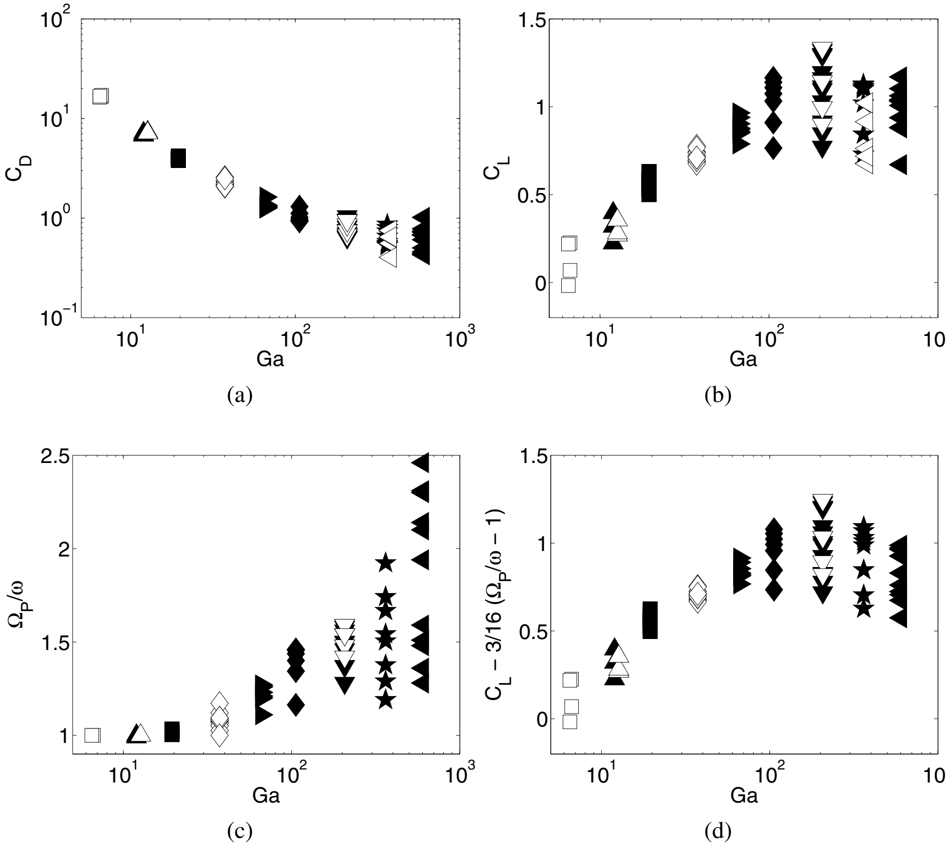

(a) (b)

(c) (d)

Figure 4.15: Drag coefficient, lift coefficient and normalized particle spin rate as function of Ga.

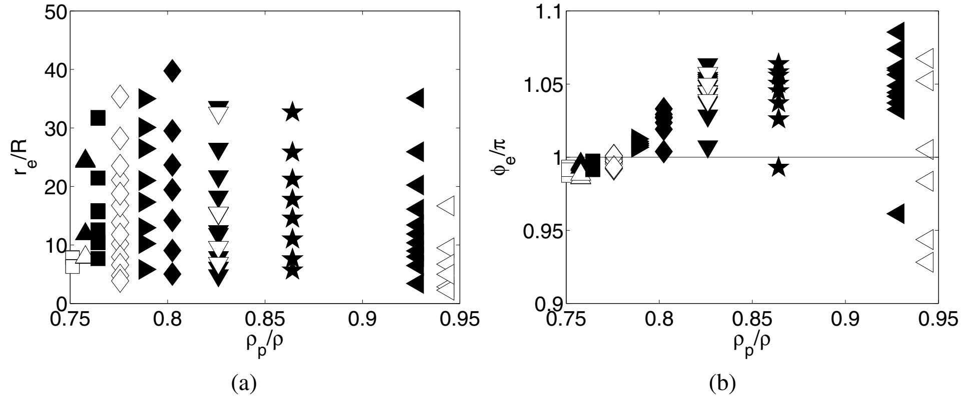

Figure 4.16: As figure 4.12 but as a function of the density ratio ρ_p/ρ.

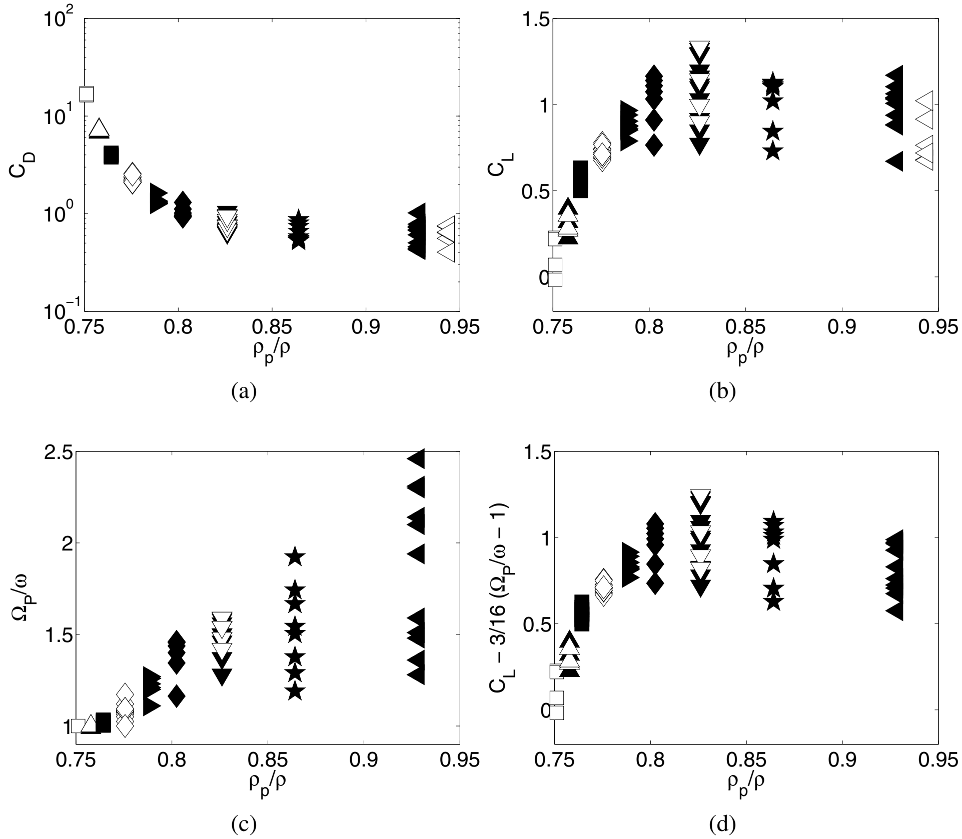

Figure 4.17: Drag coefficient, lift coefficient and normalized particle spin rate as function of the density ratio ρ_p/ρ.

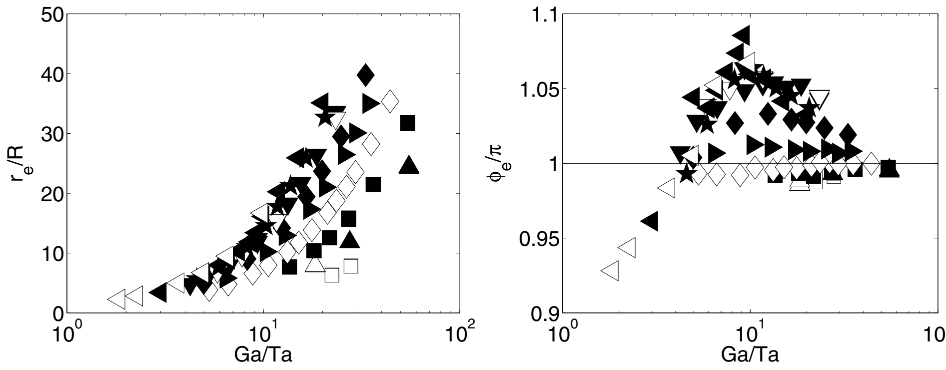

(a) (b)

Figure 4.18: As in figure 4.12 but now as a function of Ga/Ta.

4.3.6 Results: Dependence of lift and drag on other parameters

In figures 4.15a and 4.17a we found some collapse of the drag coefficient onto a curve for the Galileo number and the density ratio. The lift coefficient and the sphere spin rate cannot be represented as functions of one of the parameters Ta, Ga and ρ_p/ρ alone. In this section we will inspect different representations of drag, lift and particle spin. We include in our analysis the measured r_e/R of the system, which is a function of Ta, Ga and ρ_p/ρ. The equilibrium position appears in the definition of the Reynolds number Re, the Froude number Fr (4.19) and dimensionless vorticity Sr_ω (4.20). The dimensionless vorticity is the normalized velocity difference over the sphere and therefore resembles a dimensionless shear rate. Since in the literature lift and drag coefficients are frequently represented as functions of the Reynolds number and the dimensionless shear rate these are obvious choices. The Froude number balances the centripetal acceleration with the gravitational acceleration and has been indicated as a relevant parameter by Naciri [19] for a bubble in a horizontally rotating system. We will therefore also study the effect of Fr on the lift and drag coefficients and the particle spin.
The effect of Fr is shown in figure 4.19. The drag coefficients fall onto one line, except for the data in liquids 8 and 9 (figure 4.19a). The lift coefficients in figure 4.19b are compared to the parametrization for bubbles by Naciri [19]. Clearly, his parametrization in (2.9) is not valid for solid spheres. The particle spin cannot be represented as function of Fr (figure 4.19c). However, we can correlate the high spin rates to the peaks in the lift coefficient. Subtracting the contribution to the Magnus-like lift (4.8) due to the excess spin yields the corrected lift coefficient, figure 4.19d. The data are fitted as a linear function of Fr

$$C_L - \frac{3}{16}(\frac{\Omega_P}{\omega} - 1) = 2.52\ Fr + 0.30. \tag{4.27}$$

This fit describes the dependence of C_L on Fr for most data reasonably well. Again we find that the correction of the lift due to excess particle spin improves the collapse of the data onto a single curve.

We now consider the dependence on the Reynolds number and the vorticity parameter. For the first three liquids in table 4.1 the Reynolds number is more or less constant. This is a direct result of substituting (4.14) in the definition of the Reynolds number (4.19) and remembering that the viscosity and particle radius are constant in each liquid. For fluids with a low viscosity the radial distance decreases with the square of the cylinder rotation rate (4.15) and thus the Reynolds number is modified by varying the rotation rate of the cylinder. As a result, both the Reynolds number and the vorticity parameter depend on the cylinder rotation rate for the less viscous fluids and cannot be varied independently. From linear shear flow results

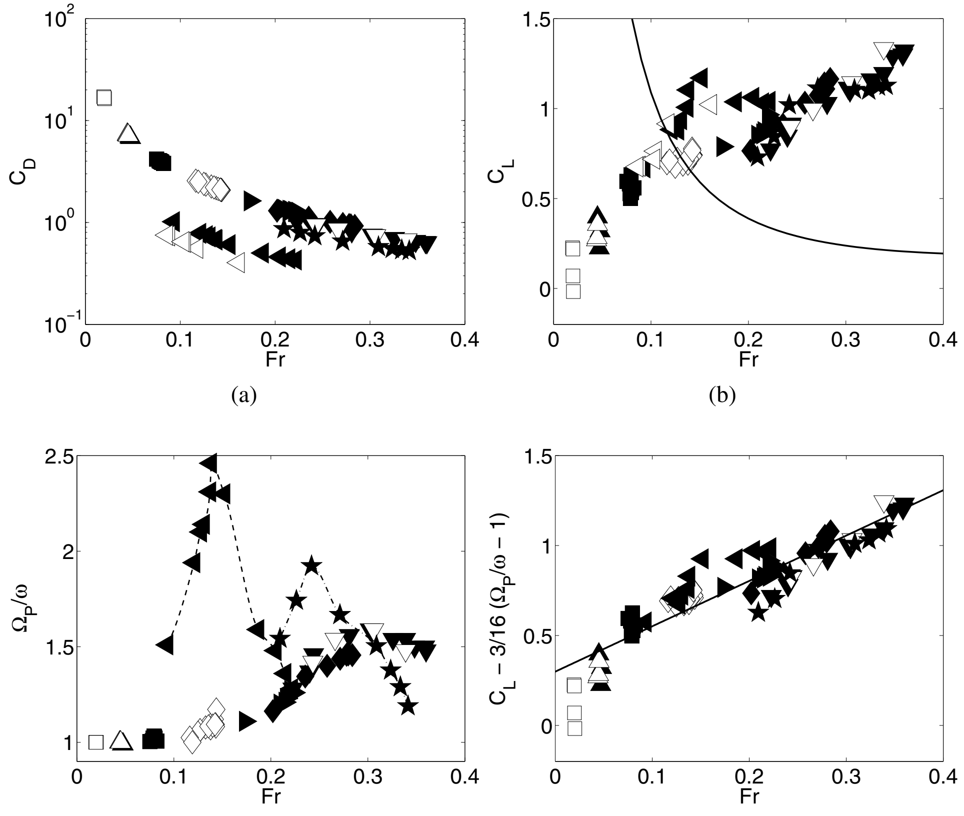

(a) (b)

(c) (d)

Figure 4.19: Drag coefficient, lift coefficient and normalized particle spin rate as function of Fr. The solid line in figure 4.19b is the parametrization of the lift coefficient for bubbles according to Naciri [19] as indicated in (2.9). The solid line in figure 4.19d is a fit to the corrected lift coefficient data (4.27).

we know that the shear rate has an effect on the drag and lift coefficient. We may expect similar behavior for our vorticity parameter. Moreover, the vorticity parameter indicates the proximity of the sphere to the cylinder center. As indicated in § 4.3.4 the distance between the sphere and the cylinder center affects the wake-interaction behavior. In an attempt to register both the Reynolds number effects and the effects due to the vorticity, we plot the results as a function of the Reynolds number, indicating the vorticity parameter by a color in figure 4.20.

In figures 4.20 and 4.21 the experimental and numerical data are compared. The numerical data points from figure 4.1 are represented by (blue) circles. Figure 4.20 displays all experimental data, whereas in figure 4.21 only data points for which $Sr_\omega \leq 0.1$ are shown. This is to allow for an adequate comparison between numerical and experimental results, since for the numerical results $Sr_\omega = 0.1$.

In figures 4.20a and 4.21a the experimentally determined drag coefficients are compared with the standard drag curve and the numerical data. It is clear from figure 4.20a that as the vorticity parameter increases, the drag coefficient generally increases. For the experimental data with $Sr_\omega \leq 0.1$ there is an excellent agreement of the experimental data with the standard drag curve, as shown in figure 4.21a.

Figures 4.20b and 4.21b show the lift coefficient. The solid line represents the fit to the numerical data (4.9). Figure 4.21b shows that the experimental data with $Sr_\omega \leq 0.1$ and $Re < 200$ fall onto (4.9), apart from the data around $Re = 5$. As indicated in table 4.2 the measurement uncertainty of C_L is high at $Re = 5$. Figure 4.20b indicates that an increase in Sr_ω generally results in a decrease in C_L. Up to liquid 7 (▼, ▽) C_L increases, in liquids 8 and 9 the values of C_L decrease. Figure 4.20b shows a small increase in C_L for liquid 9 (◀,◁) with respect to liquid 8 (★). In this liquid we observe high sphere spin rates and thus can expect a strong Magnus-like effect, increasing C_L. When we correct the C_L for excess spin as described in § 4.3.6 we find the results indicated in figures 4.20d and 4.21d. Now the decrease of the corrected lift coefficient for higher Reynolds numbers is smooth. It is of course not clear whether it is valid to assume the same effect of particle spin on the lift coefficient as in (4.8) in this Reynolds range, since we have no numerical data to validate this. However, these corrected results indicate a trend in the lift coefficient that is well worth exploring.

In figures 4.20b–4.20e and 4.21b–4.21d the dotted line at $Re = 212$ indicates the transition in a uniform flow where the wake becomes non-axisymmetric. The dashed-dotted line at $Re = 274$ indicates the transition where the wake becomes unsteady. The dashed lines in figures 4.21b and 4.21d are fits through the average values of Re and C_L in liquids 7, 8 and 9. The number of data points used to determine these fits is of course insufficient to allow more than an indication of a trend. However, it is interesting to see where this trend crosses the numerical fit (4.9) for $Re \leq 200$. In figure 4.21b the cross-over is close to $Re = 212$ (the Reynolds number at which in a uniform flow the wake loses its axisymmetry), in figure 4.21d it is close to $Re = 274$ (the Reynolds number at which in a uniform flow the wake becomes unsteady). Since $Sr_\omega \leq 0.1$ in this figure, we can expect a behavior similar to that in a uniform flow. Observing the Reynolds number at which C_L starts to decrease, it is probable that some change in the wake structure of the sphere causes the decrease of C_L (see also the discussion of C_L as function of Ga in § 4.3.5).

Figures 4.20f and 4.21c compare the experimentally observed sphere spin rate ratio (Ω_P/ω) to the numerical data and show again good agreement for $5 \leq Re \leq 127$ and $Sr_\omega \leq 0.1$. The solid lines in these figures represent the fit to the numerical data (4.7). The experimental data follow the fit well up to liquid 6. The data in liquid 7 show a sudden decrease compared to the numerical trend (figures 4.20c, 4.20e and 4.21c). Since these data are beyond the Reynolds number at which the transition to the non-axisymmetric wake occurs, the decrease in Ω_P/ω may be a consequence of a change in the wake structure behind the sphere as well.

For liquids 7, 8 and 9 the experimental data show effects that are not seen in the lower Reynolds range: for high Sr_ω, Ω_P/ω is low, followed by a peak in each liquid as the Sr_ω decreases, after which Ω_P/ω decreases (figure 4.20e). In figure 4.22 the spin rate is plotted as a function of the vorticity parameter (indicating the distance to the cylinder center). For liquid 7 the peak in the spin rate is around $Sr_\omega = 0.13$, $Re = 274$. For liquids 8 and 9 the peak is around $Sr_\omega = 0.18$. For the last two liquids wake interaction (as described in the scenarios in § 4.3.4 and sketched in figure 4.11) is considered to be the cause of the high Ω_P/ω data points. The interaction depends on the wake length and the proximity to the cylinder center and thus on Re and Sr_ω. For liquid 7, the peak occurs for lower Sr_ω. Here, instead of wake interaction, wake instability may be the cause of the decrease in Ω_P/ω. The initial increase of Ω_P/ω may be due to the increase in Reynolds number. The spin rate then decreases when the wake behind the particle becomes unsteady. This is supported by the value of Re at which the decrease in Ω_P/ω occurs ($Re = 274$, where in a uniform flow the wake becomes unsteady) as well as by the relatively moderate decrease in Ω_P/ω compared to that in liquids 8 and 9. The particle spin rates in figure 4.21c show a large spread for liquids 8 and 9 even though $Sr_\omega \leq 0.1$. It appears that Sr_ω is a much more relevant parameter to describe the sphere spin than Re for the liquids in the range $Re > 200$.

To evaluate the effect of the vorticity parameter Sr_ω on the data we normalize each data point by the value we find at the same Re and for no Sr_ω (in the case of the drag coefficient) or small Sr_ω (in the case of the lift coefficient). For the drag, we do this by normalizing the drag coefficients by the value of the standard drag curve at the corresponding Reynolds number. Figure 4.23a shows the result for liquids 1–6 plotted versus Sr_ω. It also shows an error estimate. Because it contains not only the error in the drag coefficient, but also in the Reynolds number, the error bars are rather large. The overall trend shows a linear increase of $C_D/C_{D,standard}$ with Sr_ω. Figure 4.23b shows the normalized drag coefficient for the data in liquids 7–9. Again $C_D/C_{D,standard}$ increases with Sr_ω, however for liquids 8 and 9 there is a sudden strong increase in the normalized drag coefficient around Sr_ω = 0.15. Comparing figure 4.23b with figure 4.22 shows that this rise occurs for the data for which the particle spin is strongly enhanced. As discussed above this is due to wake interaction which changes the incident flow; thus, we are considering here data with a disturbed incident velocity. However, the wake interacting with the sphere is expected to result in a decreased drag (a shielding effect). Therefore the increase of the drag coefficient cannot be the result of the disturbance of the flow field but is a result of the increase of the sphere spin. Moreover, the rise in the drag coefficient is strongest for liquid 9, where also the spin rates rise strongest. The linear shear flow results of Bagchi and Balachandar [2] show that in their case the drag is not significantly influenced by the sphere spin. However the spin of the sphere normalized by the rotation of the flow is always below one in the case of a linear shear flow. We find values of Ω_P/ω around 2.5 for liquid 9 and around 2 for liquid 8. Apparently, such high particle spin rates affect the drag coefficient. After the steep increase in drag coefficient, C_D appears to rise linearly with Sr_ω; however the data of different liquids no longer collapse onto the same line. Figure 4.22 shows that for the higher values of Sr_ω, liquid 9 displays higher values of particle spin. This may be the cause of the higher C_D values of liquid 9.

Figure 4.23c shows the lift coefficients normalized by the value of the lift coefficient for low Sr_ω obtained by fitting the numerical data (4.9) as a function of Sr_ω for $Re < 130$. No apparent effect of Sr_ω is clear from this figure. For the data with higher Reynolds numbers, we have no prediction of what the lift coefficient should be for low Sr_ω, however we can use the fit of the average of the experimental data with low Sr_ω and high Re (the dashed line in figure 4.21b) to normalize C_L. Figure 4.23d shows this normalized lift coefficient as a function of Sr_ω for $Re > 200$. In this range we see a clear trend: the lift coefficient decreases with the shear rate up to $Sr_\omega = 0.4$. After that the curve flattens. For liquid 9 we see a anomaly for the data that have high particle spin rates. The trend of the lift decreasing with Sr_ω is even more apparent if we study the lift coefficient, corrected by the particle spin (figure 4.23e). The corrected lift coefficients are now normalized by the fit through the average of the corrected lift coefficients with low Sr_ω and high Re (the dashed line in figure 4.21d). The anomaly has now disappeared and the data collapse onto the same line.

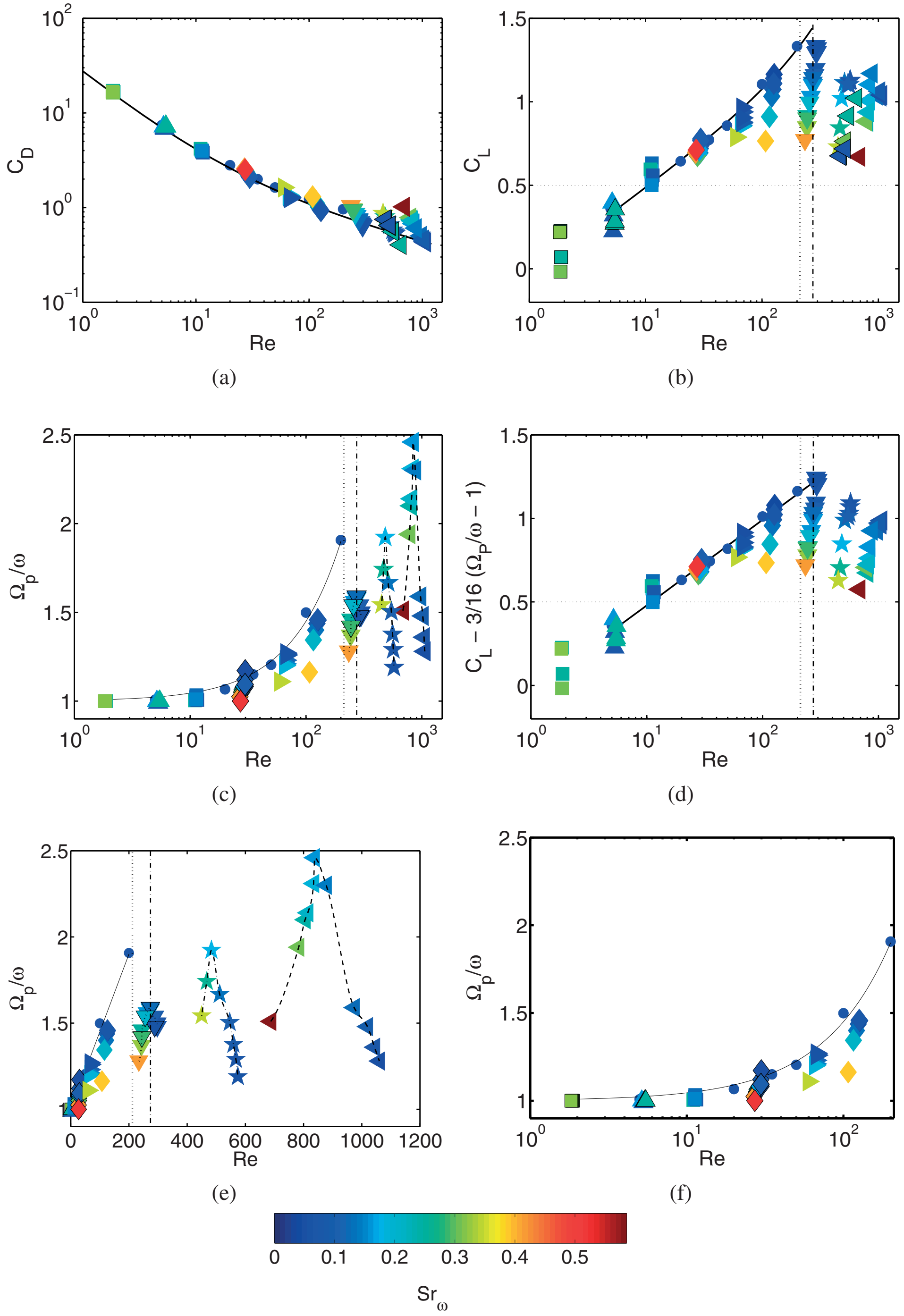
C_D
10^{2}
10^{1}
10^{0}
10^{-1}
Re
(a)
C_L
1.5
1
0.5
0
10^{0}
10^{1}
10^{2}
10^{3}
Re
(b)
Ω_p/ω
2.5
2
1.5
1
Re
(c)
$C_L - 3/16\ (\Omega_p/\omega - 1)$
Re
(d)
Ω_p/ω
0
200
400
600
800
1000
1200
Re
(e)
Ω_p/ω
Re
(f)
0
0.1
0.2
0.3
0.4
0.5
Sr_ω

Figure 4.20: (on the previous page) Drag coefficient, lift coefficient and normalized particle spin rate as function of Re. The spheres represent the numerical results. The solid line in (a) represents the standard drag curve. The solid line in (b) represents the fit to the numerical data of the lift coefficient (4.9). The solid lines in (c), (e) and (f) represent the fit to the normalized spin rates from the numerical data (4.7). The solid line in (d) represents the fit to the numerical data of the lift coefficient (4.9) with 0.0045 Re subtracted. The vertical dotted line at $Re = 212$ marks the transition to a non-axisymmetric wake, the vertical dashed-dotted line at $Re = 274$ the transition to a unsteady wake, both in case of a uniform flow. The other lines function again as guides to the eye.

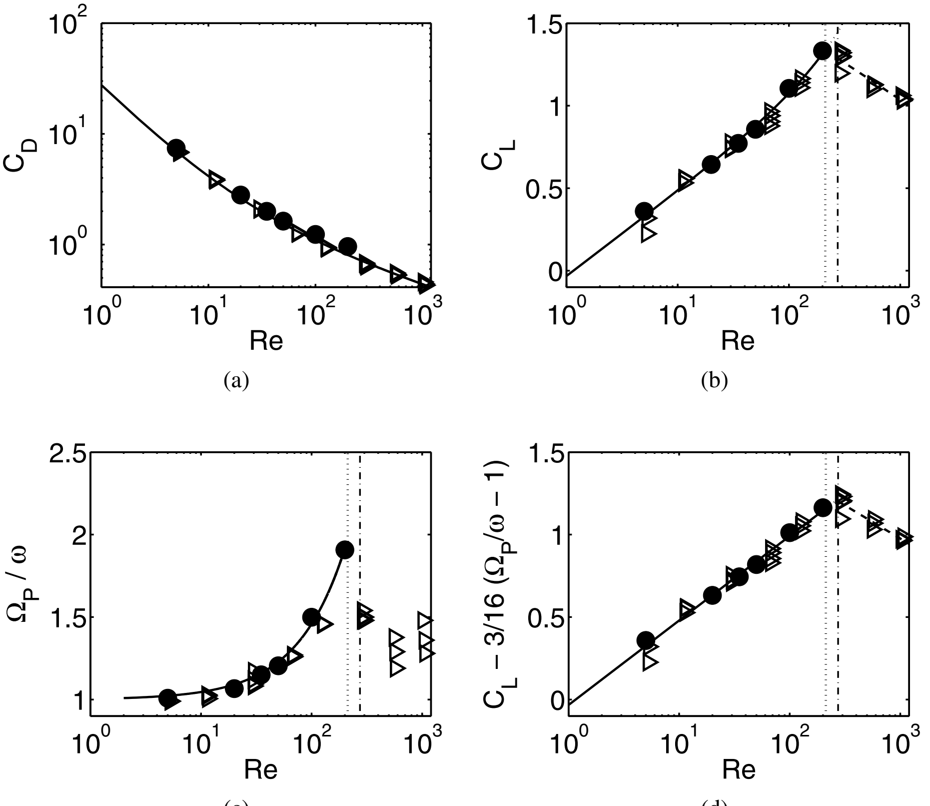

(a) (b)

(c) (d)

Figure 4.21: Drag coefficient, lift coefficient and normalized particle spin rate as function of Re, for $Sr_\omega \leq 0.1$. Circles are numerical data, open triangles are experimental data. The solid line in (a) represents the standard drag curve. The solid line in (b) represents the fit to the numerical data of the lift coefficient (4.9) for $Re < 200$. The dashed line is a fit to the average values per liquid: $C_L = -0.45\ {}^{10}\log Re + 2.37$ for $Re > 212$. The solid line in (c) represents the fit to the normalized spin rates from the numerical data (4.7). The solid line in (d) represents the fit to the numerical data of the lift coefficient (4.9) with $0.0045\ Re$ subtracted. The dashed line is again a fit to the average values per liquid: $C_L - 3/16\ (\Omega_P/\omega - 1) = -0.40\ {}^{10}\log Re + 2.18$ for $Re > 274$. The vertical lines are as in figure 4.20.

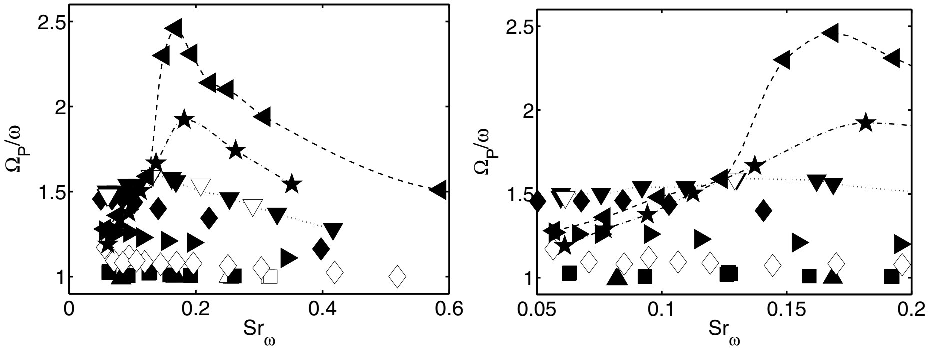

(a) (b)

Figure 4.22: Normalized particle spin rate as function of the vorticity parameter. Enlarged plot on the right-hand side.

Figure 4.23: (on the next page) Drag coefficient normalized by the standard drag coefficient and lift coefficient normalized by (4.9) in (c), and by the fits from figure 4.21b and 4.21d through the average values of data with $Sr_\omega \leq 0.1$ in (d) and (e). For (a) and (c) $Re < 130$, for (b), (d) and (e) $Re > 200$. Solid lines are fits to the data. In (a) $C_D/C_{D,standard} = 0.34 Sr_\omega + 1$, in (b) $C_D/C_{D,standard} = 0.77 Sr_\omega + 1$. In (d) $C_L/C_{L,fit} = -0.77 Sr_\omega + 1$, in (e) $(C_L - 3/16(\Omega_P/\omega - 1))/C_{L,fit} = -1.46 Sr_\omega + 1$.

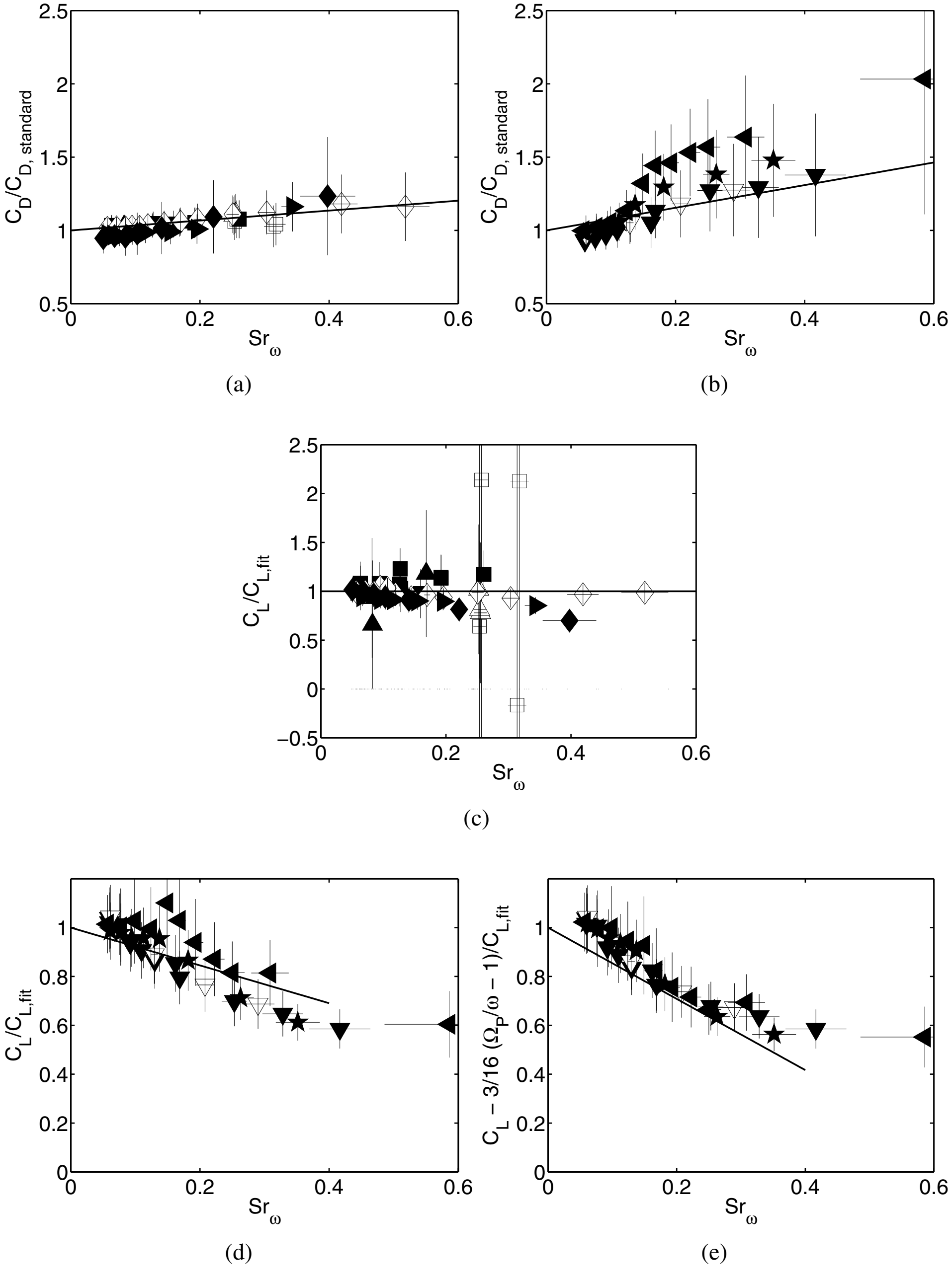
$C_D/C_{D,\,standard}$
Sr_ω
2.5
2
1.5
1
0.5
0
0.2
0.4
0.6
$C_L/C_{L,fit}$
−0.5
0.8
0.6
0.4
0.2
$C_L - 3/16\ (\Omega_P/\omega - 1)/C_{L,fit}$

(a)

(b)

(c)

(d)

(e)

4.4 Conclusion

In this study we obtained experimentally and numerically drag and lift coefficients for a sphere in a solid body rotating flow. The numerical data are in the regime $5 < Re \leq 200$. The experimental data span a much wider range: $0.1 < Re \leq 1060$.

The Reynolds number, the vorticity parameter and, for the experimental data, the Froude number are all relevant dimensionless numbers for modelling the forces on a sphere in this type of flow.

For $Sr_\omega \leq 0.1$ and $5 < Re < 1060$ the experimental results for the drag coefficient show an excellent agreement with the standard drag curve. For higher shear rates the drag increases linearly with Sr_ω.

Regarding the lift coefficient several conclusions can be drawn:

(1) For $Sr_\omega = 0.1$ and $5 < Re < 200$ the results of the numerical simulations for non-rotating and freely rotating spheres suggest that the lift coefficient can be decoupled in a flow-induced part and a part due to the sphere spin (the Magnus-like lift).

(2) Both numerical simulations and experiments indicate a logarithmic increase of the flow-induced lift coefficient with the Reynolds number for a freely rotating sphere in a solid body rotation flow in the range $Sr_\omega \leq 0.1$ and $5 < Re < 200$. The vorticity parameter has no substantial effect on C_L if $Re < 130$. Contrary to the results for bubbles in chapter 2 no negative lift coefficients were observed for a spinning sphere. The normalized particle spin rate rises linearly with Re and shows good agreement with the numerical data up to $Re \sim 130$ provided $Sr_\omega \leq 0.1$.

(3) By introducing the Froude number it is possible to realize a collapse of the lift coefficients unto a straight line.

For higher Re the dynamics becomes different. The excursion of the sphere around its equilibrium position becomes larger. The experimentally determined drag coefficients still follow the standard drag curve for data with $Sr_\omega \leq 0.1$. However, the lift coefficient now decreases as function of Re. It also decreases with Sr_ω and the decrease is linear after the lift coefficients have been corrected for particle spin. The sphere spin rate for data with $Sr_\omega \leq 0.1$ no longer increases linearly with Re. These differences in behavior of the lift coefficient and the sphere spin rate are attributed to changes in the structure of the wake behind the sphere.

The three experimental data sets in the higher Reynolds regime all display a peak in the spin rate. We ascribe this to the particle interacting with its own wake. PIV images have shown that the wake is bent towards the cylinder center. If the particle is close to the center, one side may be in the wake and this will result in a high particle spin. As the particle moves away from the cylinder center, there is no longer interaction with the wake and the particle spin rate decreases. If the particle is very close to the center the incident flow is completely disturbed and the spin rate is lowered.

References

[1] P. Bagchi and S. Balachandar. Shear versus vortex-induced lift force on a rigid sphere at moderate Re. *J. Fluid Mech.*, 473:379–388, 2002.

[2] P. Bagchi and S. Balachandar. Effect of free rotation on the motion of a solid sphere in linear shear flow at moderate Re. *Phys. Fluids*, 14:2719–2737, 2002.

[3] J. J. Bluemink, D. Lohse, A. Prosperetti, and L. van Wijngaarden. A sphere in a uniformly rotating or shearing flow. *J. Fluid Mech.*, 600:201–233, 2008.

[4] D. S. Dandy and H. A. Dwyer. A sphere in shear flow at finite Reynolds number: effect of shear on particle lift, drag, and heat transfer. *J. Fluid Mech.*, 216:381, 1990.

[5] M. Jenny, G. Bouchet, and J. Dušek. Nonvertical ascension of fall of a free sphere in a newtonian fluid. *Phys. Fluids*, 15:L9–L12, 2003.

[6] M. Jenny, J. Dušek, and G. Bouchet. Instabilities and transition of a sphere falling or ascending freely in a newtonian fluid. *J. Fluid Mech.*, 508:201–239, 2004.

[7] T. A. Johnson and V. C. Patel. Flow past a sphere up to a Reynolds number of 300. *J. Fluid. Mech.*, 378:19–70, 1999.

[8] D. G. Karamanev, C. Chavarie, and R. C. Mayer. Dynamics of the free rise of a light solid sphere in liquid. *AIChE Journal*, 42:1789–1792, 1996.

[9] R. Kurose and S. Komori. Drag and lift forces on a rotating sphere in a linear shear flow. *J. Fluid Mech.*, 384:183–206, 1999.

[10] L. D. Landau and E. M. Lifshitz. *Fluid Mechanics, 2^{nd} edition*. Butterworth-Heinenan, Oxford, 1997.

[11] S. Lee. A numerical study of the unsteady wake behind a sphere in a uniform flow at moderate reynolds numerbers. *Comput. Fluids*, 29:639–667, 2000.

[12] D. Legendre and J. Magnaudet. The lift force on a spherical bubble in a viscous linear shear flow. *J. Fluid Mech.*, 368:81–126, 1998.

[13] C. Lin, J. H. Peery, and W. R. Schowalter. Simple shear flow round a rigid sphere: inertial effects and suspension rheology. *J. Fluid Mech.*, 44:1–17, 1970.

[14] R. H. Magarvey and R. L. Bishop. Transition ranges for three-dimensional wakes. *Can. J. Phys.*, 39:1418–1422, 1961.

[15] R. H. Magarvey and R. L. Bishop. Wakes in liquid-liquid systems. *Phys. Fluids*, 4:800–805, 1961.

[16] J. Magnaudet and D. Legendre. Some aspects of the lift force on a spherical bubble. *Appl. Sci. Res.*, 58:441–461, 1998.

[17] J. Magnaudet, M. Rivero, and J. Fabre. Accelerated flows past a rigid sphere or a spherical bubble. *J. Fluid Mech.*, 284:97–135, 1995.

[18] G. Mougin and J. Magnaudet. Path instability of a rising bubble. *Phys. Rev. Letters*, 88:014502, 2002.

[19] M. A. Naciri. *Contribution à l'étude des forces exercées par un liquide sur une bulle de gaz: portance, masse ajoutée et interactions hydrodynamiques*. PhD thesis, L'Ecole Central de Lyon, 1992.

[20] A. Prosperetti. Bubbles. *Phys. Fluids*, 16:1852–1865, 2004.

[21] R. Rubinov and J. B. Keller. The transverse force on a spinning sphere moving in a viscous fluid. *J. Fluid Mech.*, 11:447–459, 1961.

[22] H. Sakamoto and H. Haniu. The formation mechanism and shedding fequency vortices from a sphere in uniform shear-flow. *J. Fluid Mech.*, 287: 151–171, 1995.

[23] L. Schouveiler and M. Provansal. Self-sustained oscillations in the wake of a sphere. *Phys. Fluids*, 14:3846–3854, 2002.

[24] E. A. van Nierop, S. Luther, J. J. Bluemink, J. Magnaudet, A. Prosperetti, and D. Lohse. Drag and lift forces on bubbles in a rotating flow. *J. Fluid Mech.*, 571:439–454, 2007.

[25] C. H. J. Veldhuis, A. Biesheuvel, L. van Wijngaarden, and D. Lohse. Motion and wake structure of spherical particles. *Nonlinearity*, 18:C1–C8, 2005.

[26] Z. Zhang and A. Prosperetti. A second-order method for three-dimensional particle simulation. *J. Comput. Phys.*, 210:292–324, 2005.

Chapter 5

Asymmetrical particles and bubbles[‡]

The bubbles and particles studied up to this point in this thesis were spherical or slightly oblate. In this chapter we consider bubbles and particles that are strongly deformed. We report on an intriguing phenomenon taking place in a liquid rotating around a fixed horizontal axis. Under suitable conditions, bubbles and particles are observed to drift along the axis of rotation maintaining a constant distance from it and a constant angle of elevation above the horizontal. Absence of fore-aft symmetry of the bubble or particle shape is a prerequisite for this phenomenon. For bubbles, this requires a volume sufficiently large for surface tension effects to be small and large deformations possible. Particle image velocimetry and flow visualization suggest that the particle wake does not play a role. The dependence on bubble radius, particle shape, liquid viscosity and speed of rotation is investigated.

5.1 Introduction

In the course of an ongoing project to study the forces acting on bubbles in a rigid-body rotating flow, we encountered an intriguing phenomenon which is reported in this paper. In the experiment, a liquid-filled horizontal glass cylinder (length 500 mm, diameter 100 mm) is in steady rotation around its axis. Under certain conditions, a large bubble (equivalent radius $R_b > 5$ mm) injected in the liquid starts

---

[‡] J.J. Bluemink, E.A. van Nierop, S. Luther, N. Deen, J. Magnaudet, A. Prosperetti and D. Lohse, *Asymmetry-induced particle drift in a rotating flow*, Phys. Fluids. **17**, 072106 (2005).

moving back and forth along a line parallel to the axis of the cylinder, while maintaining a constant distance from the axis and elevation to the horizontal, without any external force acting in this direction. Further experiments indicate that certain particles also exhibit a similar axial drift.

5.2 Experiments

The cylinder is filled with a glycerin-water mixture and maintained in steady rotation with angular velocities ω between 0 and 40 rad s^{-1}. In this flow, small bubbles (bubble radius $R_b \approx 1$ mm) reach a steady equilibrium position under the action of buoyancy, drag, added mass, and lift [3, 5]. In a water-glycerin mixture with relatively large viscosity ($\nu \geq 10^{-5} m^2 s^{-1}$) and at sufficiently large angular velocities, on the other hand, large bubbles (equivalent bubble radius $5\ mm \leq R_b \leq 10\ mm$) are observed to drift parallel to the cylinder axis. Their shape has no obvious symmetry. The drift appears to be very regular and steady and to take place at a fixed distance r_e from the axis of rotation and at a fixed angle of elevation φ_e above the horizontal. When the bubble reaches an end cap of the cylinder, it bounces, its shape is reflected, and it starts travelling in the opposite direction at the same speed as before. At lower viscosities, these large bubbles tend to break and, when they do not, their translational motion in general is less stable. If the bubble is too large ($R_b \geq 15\ mm$) or the rotation rate is too high, the bubble also breaks.

5.3 Results

The drift velocity v_z is found to be dependent on the angular velocity ω, the equivalent bubble radius R_b, and the liquid viscosity. Figure 5.1 shows v_z vs. the rotation rate for different R_b and ν.

In order to gain some understanding of the nature of the flow near the bubble, the liquid was seeded with tracer particles illuminated by a light sheet perpendicular to the cylinder axis in a standard PIV arrangement. Figure 5.2, in which the black silhouette is the bubble, shows a cross section of the flow field obtained in this way. Here the rotational Reynolds number, defined as $Re_r = \omega r_e R_b / \nu$ is about 20. The x-axis is horizontal and the y-axis vertical in a plane perpendicular to the cylinder axis the position of which, located at $(x = 0, y = 0)$, is marked by a cross. The color coding gives the magnitude of the velocity vectors. The image suggests that the wake trailing the bubble in the circular motion has essentially dissipated by the time the liquid has completed an entire revolution. Thus, the bubble does not seem to interact appreciably with its own wake.

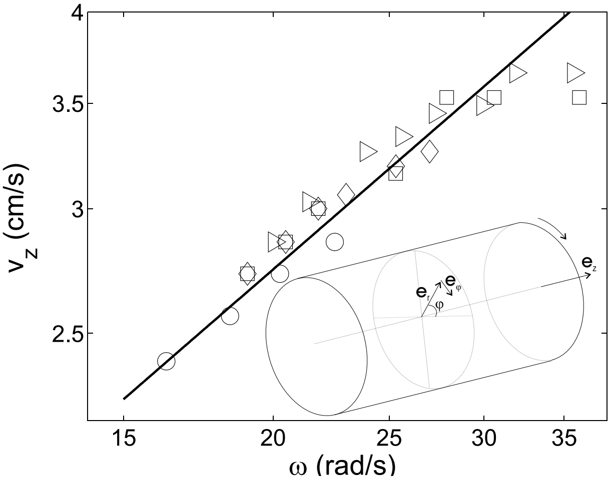

Figure 5.1: The axial drift velocity versus the rotation rate of the cylinder for large bubbles on a log-log scale. □ $R_b \approx 6.2$ mm, ∘ $R_b \approx 7.2$ mm; ▷, ◊ R_b not specifically measured. □ $\nu = 6.7\times10^{-5}$ m^{2}s^{-1}; ∘, ▷ and ◊ $\nu = 1.7\times10^{-5}$ m^{2}s^{-1}. Solid line: $v_z \propto \omega^{0.66}$.

By recording the tracer particles trajectories with a longer exposure we obtain an indication of the pathlines of the flow. In Fig. 5.3 the pathlines in a cross-section of the (x,y)-plane are shown for a bubble moving away from the camera. In frames 4, 5 and 6 the bubble travels through the light sheet. Here several vortices are apparent, although it is not clear whether they remain attached to the bubble or are shed similarly to a Kármán vortex street. The relatively low Reynolds number of the rotational flow, $Re_r \sim 20$, suggests the first possibility as the more likely one.

Since the phenomenon only occurs with strongly deformed bubbles, we decided to investigate whether it would also occur with asymmetrically shaped rigid bodies made out of a plastic material with a density $\rho = 900$ kg m^{-3}. As a control, we used particles with fore-aft symmetry such as solid spheres, prolate spheroids, and cylinders and spheroids cut by planes parallel to the major axis. All these symmetric bodies aligned their major axes with that of the rotating cylinder and came to an equilibrium position (fixed r_e, φ_e, and axial location) just like spherical bubbles. When the fore-aft symmetry was broken, however, the same axial drift observed with large bubbles set in. The presence or absence of axial symmetry did not seem to play a role. Thus, we find that cones (Fig. 5.4 a, b, c) exhibit axial drift, as well as “mutilated” cylinders (Fig. 5.4 d), and spheroids cut at an angle to their symmetry axis (Fig. 5.4 e, f). The linear dimensions of the particles we studied were of the order of 10 mm and the angular velocities for which the drift

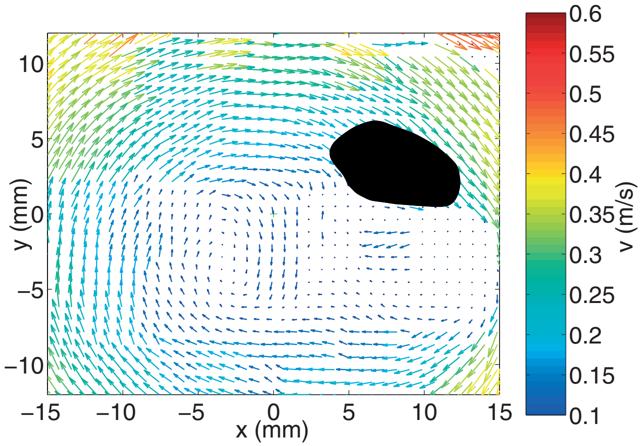

Figure 5.2: (Color) Velocity field in a plane perpendicular to the cylinder axis; the bubble (black silhouette) is moving towards the camera. ω = 22.6 rad/s, ν = $9.9{\times}10^{-5}$ m^2/s, R_b = 8 mm.

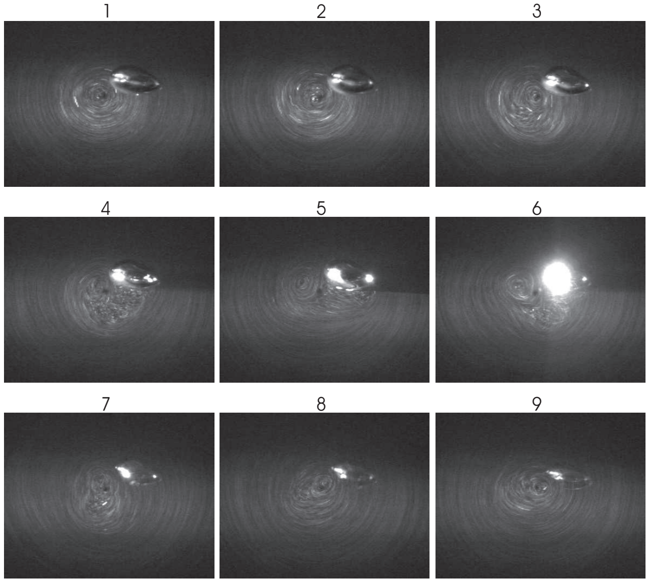

Figure 5.3: Pathlines in (x, y)-plane around a bubble moving through a light sheet, away from the camera. ω = 28.3 rad/s, ν = $1.8{\times}10^{-4}$ m^2/s, R_b = 10 mm.

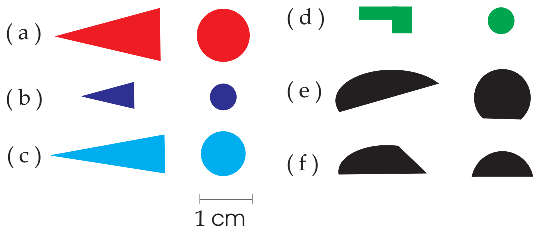

Figure 5.4: Particles that display axial drift in rigid-body rotation. Side view (left) and top view (right). The legends in figures 5.5, 5.6, 5.7, 5.8 refer to the letters in this figure.

occurred were substantially lower than for bubbles, between 2 rad s^{-1} and 20 rad s^{-1}. Unlike bubbles, for particles the axial drift was found in fluids with both high and low viscosities (e.g. water); however, the phenomenon was robust when $\nu \geq 10^{-5} \mathrm{m}^2\mathrm{s}^{-1}$. In addition, in contrast to bubbles, which are observed to turn around once they reach one of the bases of the cylinder, solid particles remain at the bases.

We characterize the size of the particles in terms of the radius of the base shown in the right column of Fig. 5.4; this characteristic length will be denoted by the same symbol R_b used earlier for the equivalent bubble radius. Given the variables ω, ν, R_b and the gravitational acceleration g, two non-dimensionless parameters can be defined, a "Froude number" $Fr = \omega^2 R_b/g$ and a dimensionless angular velocity $\Omega = \omega {R_b}^2/\nu$. This latter parameter represents the square of the ratio of the particle radius to the viscous diffusion length. The response of the system can be characterized in terms of the rotational Reynolds number Re_r defined earlier, the drift Reynolds number $Re_d = v_z R_b/\nu$, and the angle of tilt α of the particle with respect to the cylinder axis.

Figure 5.5 shows the tilt angle α vs. Ω for a glycerin-water mixture of 80% glycerin by weight. The particles only tend to align with the cylinder axis at high rotation rates, while at low rotation rates the tilt can be quite substantial. The particles display the largest drift velocity when their angle of tilt is between 20 and 40 degrees.

In Fig. 5.6 the drift Reynolds number Re_d is plotted as a function of the dimensionless numbers Ω and Fr for particles of different size and shape, and for different viscosities. The cut cylinder and small cone have the same base surface, while the base surface of the large cone is twice as large. The aspect ratios for all particles in the figure is 2:1. The cones follow their tips, the cut cylinder follows the side where the material is cut away.

It was already mentioned that the particle drift depends on the liquid viscosity.

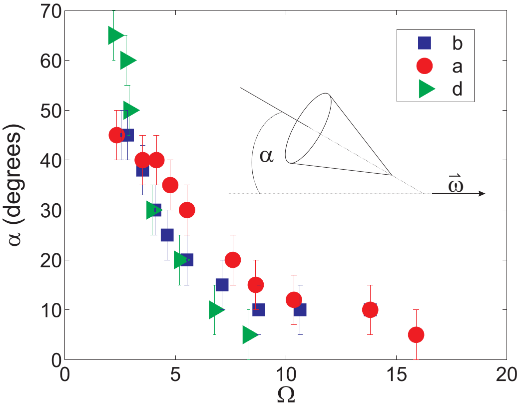

Figure 5.5: Tilt of the particle with respect to the cylinder axis (α) versus Ω. The tilt is determined with a protractor, which accounts for the rather large error.

Figure 5.6 shows the drift Reynolds number of the particles in glycerin-water mixtures of 60% and 80% by weight vs. Ω (Fig. 5.6 a) and vs. Fr (Fig. 5.6 b). The straight lines in Fig. 5.6 a correspond to $Re_d \sim 1/\Omega^2$, or $v_z \sim \nu^3/(\omega^2 R_b^5)$, while the straight lines in Fig. 5.6 b show the relation $Re_d \sim Fr^{-1}$, or $v_z \sim \nu g/(\omega^2 R_b^2)$. These figures seem to exhibit two different regimes, one for the lower values of Ω or Fr, and one for larger values of these quantities.

In Fig. 5.7 the same data are plotted in the form of Re_d/Ω vs. Fr^2/Ω. This figure indicates that, for sufficiently large values of the parameter Fr^2/Ω and the larger viscosity, the results for Re_d/Ω exhibit an approximate collapse onto a line $Re_d/\Omega \sim \Omega/Fr^2$, implying $v_z \sim g^2 R_b/(\nu\omega^2)$.

It seems that the direction of motion depends on the orientation of the particle: The tip seemed to be inclined towards the axis of rotation, when the drift was in the direction of the tip. For drift in the opposite direction, the tip seemed to be oriented away from the axis. If the orientation is reversed by shaking the cylinder, so immediately is the direction of travel. The reverse motion seemed to be favored for larger particle and less viscous liquids. Figure 5.8 shows the drift Reynolds number Re_d plotted as a function of Ω and Fr for the larger cones in a fluid with a lower viscosity. These cones drift in the direction opposite to the orientation of their tip. The two cones have the same surface area and different aspect ratios of 2:1 and 3:1.

An obvious concern in the interpretation of these data is the possibility of wall effects when the particles stabilize too close to the cylinder wall. While a precise measurement of the distance of the particles from the cylinder axis was not possible, an approximate estimate can be found by a force balance in the plane through

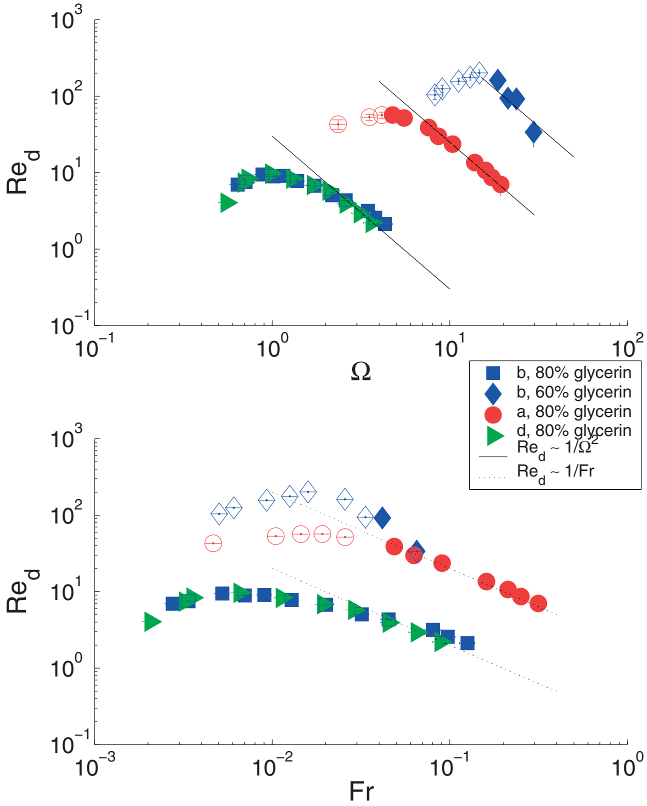

Figure 5.6: Drift Reynolds number vs. (a) $Re_d = \omega {R_b}^2/\nu$, and (b) $Fr = \omega^2 R_b/g$ for cones moving in the direction of the tip. Open symbols: data for particles estimated to be near the cylinder wall.

the particle perpendicular to the axis of rotation. For the purposes of a rough estimate we assume that the same forces act on the particle as would act on a spherical bubble, except for buoyancy. Expressions for the forces on bubbles can be found in [4] and in [3]. The drag force is expressed in terms of a drag coefficient, for which we take the large Re limit $48/Re_r$ [4]. The inertial, or added mass, force has the usual expression in terms of a coefficient C_A for which we use the sphere value 1/2. For the lift force we use the high-Reynolds number expression of [1] with a lift coefficient C_L also equal to 1/2. In this way, as shown in Ref. [3], one finds

$$r_e \simeq \frac{{R_b}^2(\rho_l - \rho_b)g}{\rho_l \omega \sqrt{81\nu^2 + \frac{1}{4}{R_b}^4\omega^2}}. \tag{5.1}$$

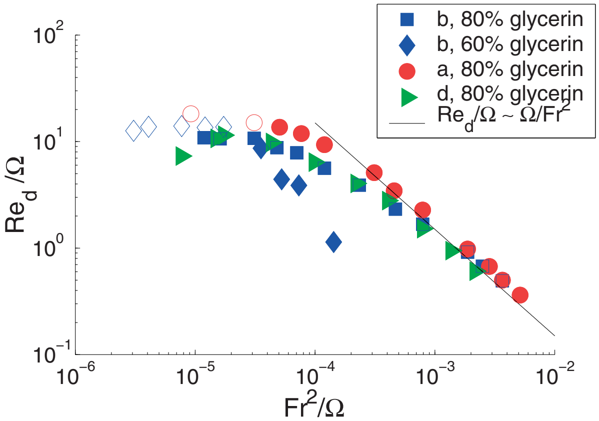

Figure 5.7: (a) Scaled drift Reynolds number Re_d/Ω vs. Fr^2/Ω for cones moving in the direction of the tip.

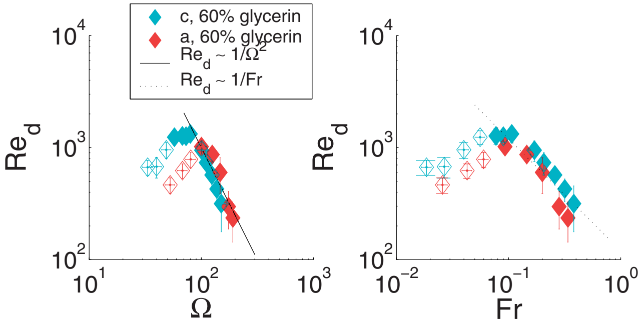

Figure 5.8: Drift Reynolds number versus (a) Ω, and (b) Fr for cones moving away from the tip. Decreasing the viscosity or increasing the size of the particle can reverse the direction of drift.

Here ρ_l and ν are the liquid density and kinematic viscosity, and ρ_b the bubble or particle density. For small viscosity this relation reduces to $\rho_l r_e \omega^2 \simeq (\rho_l - \rho_b)g$, which expresses a balance between the centrifugal and gravitational pressure gradients. Similarly, when viscosity dominates, we find $\mu_l(\omega r_e)R_b \simeq R_b^3(\rho_l - \rho_b)g$, which balances Stokes-like drag in a liquid with viscosity μ_l with buoyancy. Thus, while (5.1) may not rest on a particularly firm theoretical basis, it does embody the correct limiting behaviors and may offer a reasonable interpolation between the two for intermediate situations.

At large rotation rates, Eq. (5.1) shows that $\omega r_e \propto \omega^{-1}$. The proportionality of the drift velocity v_z to ω^{-2} pointed out before in connection with Fig. 5.7 would then be understandable if the force causing the drift were to scale like the square of the rotational velocity at the particle position as with a Bernoulli effect. For low rotation rates, on the other hand, Eq. (5.1) shows that the particle is closer to the cylinder wall and wall effects eventually may become dominant. The data for which the particles are estimated (with Eq. (5.1)) to be less than a particle diameter from the wall are indicated by open symbols in Figs. 5.6, 5.7, and 5.8. While most of the data points falling away from the straight lines appear to correspond to locations affected by proximity to the wall, others do not. Hence, whether the two regimes apparent from the figures are indeed to be ascribed to wall effects must remain an open question at present.

5.4 Conclusion

A qualitative explanation for the transverse motion can be found by considering the pressure distribution over the particle or bubble surface. When a fluid flows over an object, on the high velocity-sides of the object surface the pressure is low, causing suction forces. If the flow did not separate, while the drag force would of course vanish due to a cancellation of the pressure forces in the direction of the flow, a non-zero lift force would be generated since opposite surface elements are not parallel to the axis. It is likely that a similar stress distribution is responsible for the phenomenon described before. Under the action of this lift force, the particle would drift axially at a velocity such that the drag balances the lift. In this sense the drift we have observed can be understood as analogous to the forward motion of a falling inclined cone, with the falling velocity replaced by the liquid rotation.

Mathematically, an equivalent description may be given in terms of the added mass tensor [2]. In the absence of fore-aft symmetry, the added mass tensor has non-zero off-diagonal elements when expressed in the cylindrical coordinates of the present situation. In particular, there will be a non-zero rz-element with the result that a radial acceleration (in the present case the centrifugal acceleration) produces a force in the z-direction. At low rotation rates the particle has more tilt with respect to the cylinder axis, the situation is more asymmetric, and the off-diagonal components of the tensors increase, giving rise to higher transverse velocities.

References

[1] T. R. Auton, J. C. R. Hunt, and M. Prud'Homme. The force excerted on a body in inviscid unsteady non-uniform rotating flow. *J. Fluid Mech.*, 197:241–257, 1988.

[2] H. Lamb. *Hydrodynamics, 6th Edn.* Dover, New York, 1932.

[3] D. Lohse and A. Prosperetti. Controlling bubbles. *J. Phys.: Condens. Matter*, 15:S415–S420, 2003.

[4] J. Magnaudet and I. Eames. The motion of high-Reynolds number bubbles in inhomogeneous flows. *Ann. Rev. Fluid Mech.*, 32:659–708, 2000.

[5] M. A. Naciri. *Contribution à l'étude des forces exercées par un liquide sur une bulle de gaz: portance, masse ajoutée et interactions hydrodynamiques*. PhD thesis, L'Ecole Central de Lyon, 1992.

Chapter 6

Hydrodynamic interactions between identical spheres in a solid body rotating flow[‡]

Potential flow predicts that two particles will attract each other, whereas in the creeping flow limit they repel. In this chapter we will explore the intermediate Reynolds range and show the effects of the particle center-to-center distance and of the angle between the incoming flow and the line that connects the particle centers. Lift and drag coefficients and particle spin rate as functions of the distance, angle, Reynolds number and flow vorticity are studied. The effect of the rotation of the flow becomes especially relevant if a particle pair is oriented parallel to the main flow.

6.1 Introduction

Experimental results of Duineveld [4] and Kok [11] indicate that bubbles that started off in a line arrange horizontally with respect to the incoming flow. Irrotational flow models predict that spherical bubbles form horizonal clusters [16, 17, 21]. On the other hand there is only one brief report of such clustering in experiments of bubble laden flows [5]. Bubble shape and the vorticity in the wake of the bubbles are indicated as possible causes for the discrepancy between experimental results and the irrotational predictions.

[‡] To be published as J.J. Bluemink, A. Prosperetti and L. van Wijngaarden, *Hydrodynamic interactions between identical spheres in a solid body rotating flow*.

For particles in industrial applications, Reynolds numbers in the range of 20–300 are of interest. Particles will behave differently from bubbles, however, as its surface adsorbes surfactants, the bubble will display behavior comparable to that of a solid sphere. Therefore, studying sphere interaction is relevant for bubble behavior in non-clean water.

The two most investigated arrangements of two interacting particles are particles placed (1) side-by-side (the line connecting the centers of the particles is perpendicular to the incoming flow) and (2) in line with respect to the incoming flow.

At zero Reynolds number there is no transverse force on the particles. For particles aligned side-by-side at small but finite Reynolds numbers the distance between the particles determines their interaction forces (see Happel and Brenner [7]). When the particles are far apart, the situation is governed by inertia effects and the particles weakly attract. When they are close, viscous effects become significant. The gap between the spheres blocks the flow and the fluid at the sides of the particles furthest from the symmetry plane moves faster than that at the sides close to the symmetry plane. As a result the pressure is lower at the sides furthest from the symmetry plane and the particles repel.

In the intermediate Reynolds range Kim et al. [10] investigated the forces on two spheres arranged side-by-side in a uniform flow at $Re = 50, 100, 150$ for different spacings D_{cc} (distance between sphere centers d_{cc} normalized by the particle radius R) between the spheres. They found that the spheres repel when they are close ($D_{cc} < 15.8$ for $Re = 50$, $D_{cc} < 8$ for $Re = 100$ and $D_{cc} < 6.8$ for $Re < 150$) and weakly attract when they are at intermediate distance. When far enough apart ($D_{cc} > 42$) there is no longer interaction between the spheres. For $D_{cc} < 8$ the drag increases with decreasing D_{cc}. A slight increase in drag compared to a single sphere is seen for $8 < D_{cc} < 42$. When the spheres are close their tops rotate towards the symmetry plane, whereas for intermediate distances their spin is in the opposite direction. The distance where the transition in torque direction occurs is earlier then for the attraction/repulsion case: $D_{cc} < 9.2$ for $Re = 50$, $D_{cc} < 5.0$ for $Re = 100$ and $D_{cc} < 3.9$ for $Re < 150$. Particle spin was not studied.

Folkersma et al. [6] studied two spheres side-by-side at $Re = 10$, 50 and 5×10^{-7}. They also found the change from repulsion to weak attraction (for $Re = 10$ at $D_{cc} = 46$ and for $Re = 50$ at $D_{cc} = 15.8$).

Legendre et al. [12] studied hydrodynamic interactions between two bubbles side-by-side for a wide range of Reynolds numbers ($0.02 \leq Re \leq 500$) and center-to-center distances normalized by the bubble radius ($2.25 \leq D_{cc} \leq 20$). Their work shows a smaller drag compared to the single bubble drag for small Re and a larger drag from $Re \sim O(10)$ due to the presence of the other bubble. Furthermore, the bubbles repel for Re below around 20 and after that start to attract. The exact values of the Re depend on the center-to-center distance.

Particles and bubbles rising in line with respect to the incoming flow have also been studied extensively. Harper [8] investigated theoretically the situation of two spherical gas bubbles rising steadily in a line in a pure liquid for large Re. He assumed the flow to be irrotational and superposed a uniform stream on a set of image doublets. An equilibrium distance between the bubbles was predicted.

Spherical bubbles in line where numerically studied by Yuan and Prosperetti [23] for $Re \leq 200$ and separation distances of $D_{cc} > 2.6$. An equilibrium separation distance was predicted, where the wake effect and the inertial repulsion balance. The results show very strong viscous effects, even at $Re = 200$, indicating the high-Reynolds-number results for spherical bubbles impractical (since for even higher Re sphericity is not likely).

Harper [9] improved on the theoretical analysis of Harper [8] by allowing for viscosity in the wake between the bubbles and obtained a better agreement with the numerical results of Yuan and Prosperetti [23].

Ruzicka [15] studied numerically the dynamical behavior of a chain of spherical gas bubbles rising in a vertical line in the range $50 < Re < 200$, bubble spacing $D_{cc} > 2.6$ (low spacing or touching bubbles was excluded). He found a progressive drag reduction down the chain for the anterior bubbles due to the velocity disturbances caused by the previous bubbles. Three bubbles had no steady solution for $Re < 135$, but yielded a fast leading pair with a slow singlet behind it. He showed that when inertial effects increase, the drag difference becomes smaller, so that a triplet can be stable and that it rises slightly faster than a pair.

Chen and Lu [3] investigated experimentally both particles side-by-side and in line for $Re < 200$ and found for the latter case a reduced wake for the trailing particle under influence of the leading sphere. Tal et al. [18] investigated numerically the interaction of two spheres in line for two different separation distances at Re=40. Zhu et al. [24] experimentally measured the effect of the wake of one particle on the other for $20 \leq Re \leq 130$. Tsuji et al. [20] studied both particles in line and side-by-side experimentally for $Re < 1000$. They found that for particles in line the interaction effects disappear when the separation distance becomes larger than 5 to 10 times the sphere diameter, but for particles side-by-side the effect already disappears for separation distances of 2 to 3 times the sphere diameter. More experimental work studying the drag force for particles in line and side-by-side was done by Liang et al. [13] and [3]. Tsuji et al. [19] numerically studied particles side-by-side and in line for Re = 30, 100, 200, and 250 .

As indicated in the conclusions of Legendre et al. [12] it is important to explore how the equilibrium distance depends on the angle between the incoming flow and the line that connects the bubble or particle centers to be able to come to a more general moderate-to-high Reynolds number description for interaction forces.

Several authors studied the effect of the angle between the line connecting the particle centers and the incoming flow together with the effect of the separation distance. Prahl et al. [14] numerically studied the drag and lift coefficient of two fixed spheres at particle Reynolds numbers Re of 50, 100 and 200 for separation distances up to 6 times the sphere diameter. They found a large decrease of the drag when the particles are placed in line and an increase for the side-by-side arrangement. The largest effect on the lift was found for a particle slightly upstream and at a small separation distance. Yoon and Yang [22] numerically studied the mean drag and lift coefficient as functions of the angle and the separation distance (up to 4 times the sphere diameter) for Re = 300.

This chapter focusses on a pair of identical spheres in different arrangements with respect to the incoming flow. In two ways this work is different from previous numerical simulations. Firstly, the particles are in a solid body rotating flow. However small the rotation may be, there will be some curvature in the flow and this will affect the symmetry. Secondly, the spheres are allowed to reach a torque-free spin rate. In most of the earlier studies the spheres were fixed and not allowed to spin.

6.2 Geometry and numerical method

In this chapter we consider particles with a radius R in a solid body rotation flow field defined by (3.15) with the prefactors α and β set equal to 1. The particle at $(x, y) = (0, 0)$ in figure 3.14 is referred to as the **reference particle**. The relevant dimensionless numbers in the numerical simulations for the reference particle are the particle Reynolds number Re as defined in (3.1) and the vorticity parameter Sr_ω as defined in (3.10).

Particle interactions in a solid body rotation flow field can be studied in several ways. In this chapter we restrict ourselves numerically to two situations. In the first situation we study an infinite line of particles parallel to the axis of rotation. Further details are given in § 6.2.1. In § 6.2.2 we consider a second interaction situation, i.e. two particles interacting in a plane perpendicular to the vorticity. The numerical method is the same as in § 3.4. The domain size is chosen in the same way as in § 3.4, i.e. the boundary is always at least 10 particle radii away from the particle centers, expect in the axial direction (where period boundary conditions are applied), where it is at least 8 particle radii away. The resolution and the order of the analytical expansion (discussed in § 3.4) may behave somewhat differently in the case of two interacting particles compared to a single particle. For further detail see § 6.3.1.

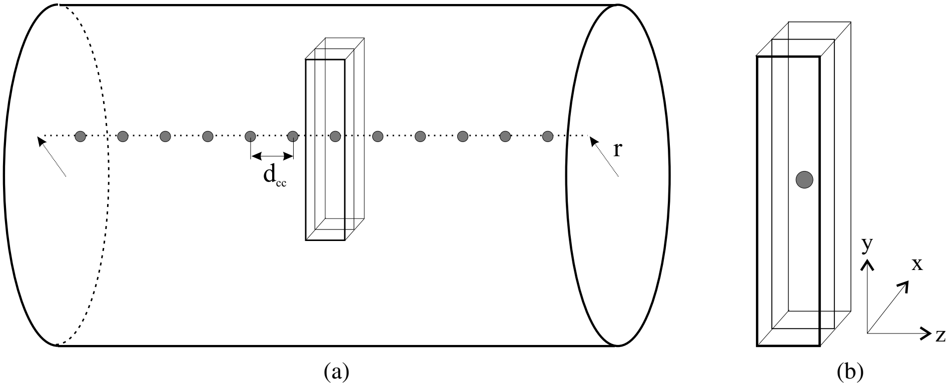

(a) (b)

Figure 6.1: (a) Line of particles simulated as a result of periodic boundary conditions on the xy-planes. (b) Simulation domain where the domain size in z-direction determines the center-to-center distance d_{cc} for the line of particles.

Experimentally the particle interactions are studied by inserting several spheres in the cylinder the characteristics of which were described in chapter 4. The procedure described in § 4.3.2 was followed and a long settling time was allowed. Inserting only a few spheres will make the chance on interaction very small in the experimental situation since the cylinder covers a length of 500 mm. Therefore about 30 particles were inserted to increase the probability of an interaction.

6.2.1 Particles along a line parallel to the axis of rotation

As described in § 3.4 periodic boundary conditions were used on the bounding planes normal to the rotation axis of the solid body rotation. As a result, if the simulation domain contains one sphere, we simulate an infinite line of spheres a center-to-center distance d_{cc} apart, equivalent to the situation in figure 6.1a. When the domain size in the axial direction is sufficiently large as in chapters 3 and 4, the presence of the other spheres is not noticeable. If however the domain in the axial direction is small as in figure 6.1b, the particles are close and affect the forces on each other. Changing the domain in the axial direction is equivalent to changing d_{cc}. In fact d_{cc} equals the box size in axial direction. The center-to-center distance d_{cc} is normalized by the particle radius R and the ratio is referred to as D_{cc}. The effects of changing D_{cc} on the drag coefficient as defined in (4.1), the lift coefficient as defined in (4.2) and the torque-free spin rate are considered.

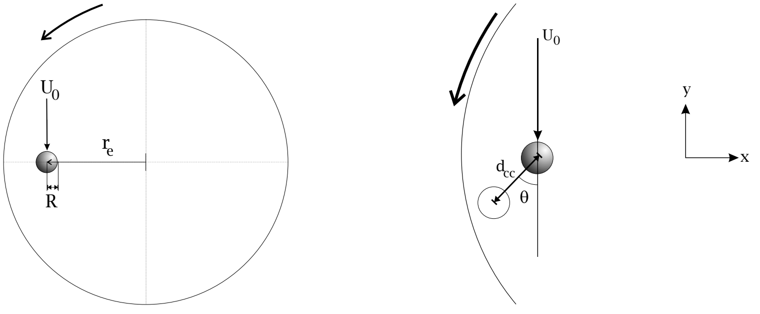

(a) (b)

Figure 6.2: (a) Geometry for the reference particle. (b) Geometry for two particles interacting in a plane perpendicular to the vorticity, defining d_{cc} and θ.

6.2.2 Two particles interacting in solid body rotation

Figure 6.2a displays the position of the reference particle in the solid body rotation flow field. To study interactions between two particles in this flow field, a second particle is placed at a distance d_{cc} from the center of the first particle in the same axial plane as the reference particle. Note that d_{cc} is no longer the center-to-center distance in axial direction, but now refers to the distance in one axial plane. The periodic boundary conditions on the bounding planes normal to the rotation axis are maintained, however the domain in axial direction is so large (at least 16 sphere radii) that the presence of the other particles on the line parallel to the axis has no effect.

The center-to-center distance between the particles d_{cc} is again normalized by the particle radius R and the ratio is referred to as D_{cc}. The line connecting the two particles defines the angle θ with the direction of the incoming flow, the negative y-axis, see figure 6.2b. In the numerical simulations both the reference particle and the second particle are fixed. The forces on the reference particle and the torque-free spin rates (see chapter 3) of both particles are considered as functions of D_{cc}, θ, Re, and Sr_ω.

When Sr_ω is small, the reference particle is far from the axis of rotation. The flow will be very similar to a uniform flow in that case. For a single particle on the horizontal axis, the force in the y-direction can be seen as a drag force. The force in the x-direction is a combination of lift, added mass and pressure gradient forces, see (4.2). When a second particle is placed near the first particle, these forces will be changed by the hydrodynamic interactions. The forces are expressed in terms

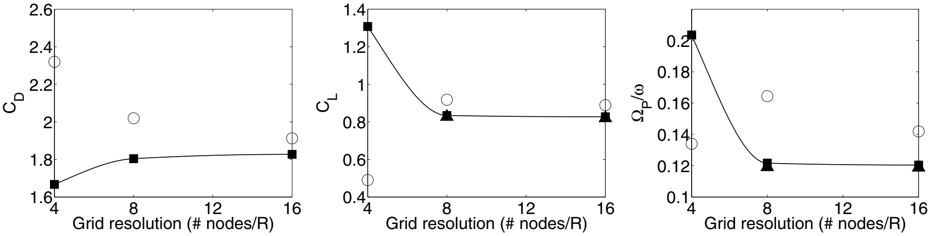

Figure 6.3: Drag and lift coefficients and Ω_P/ω at Re = 50 and Sr_ω = 0.2 for different resolutions and order of the analytical expansion. Circles: order 1, squares: order 2 and triangles: order 3.

of the coefficients C_D and C_x

$$C_D = F_y/(\frac{1}{2}\pi R^2 \rho U_0^2), \tag{6.1}$$

$$C_x = F_x/(\frac{1}{2}\pi R^2 \rho U_0^2), \tag{6.2}$$

where F_x and F_y are the forces in the horizontal (x-) and the vertical (y-) direction, ρ is the liquid density and U_0 is the undisturbed velocity at the center of the reference sphere.

Both particle centers are fixed, but the particles are free to rotate. Although in realistic flow situations particles are seldom fixed to their positions, the evaluation of the forces can give an idea of equilibrium distances and particle behavior in particle-laden flows.

6.3 Results

6.3.1 Numerical accuracy and validation

All simulation results are for steady-state cases, the drag and lift forces having reached a constant value and the particles having settled into their torque-free spin rates. We will first consider the accuracy of simulations with a single sphere and then address the accuracy of the simulations with two interacting particles.

Influence of resolution and order for a single sphere

Figure 6.3 shows the effect of the grid resolution and the order of the analytical expansion on a single particle in a flow in solid body rotation at $Re = 50$, Sr_ω = 0.2. Comparing the drag coefficient (defined in (6.1)), lift coefficient (defined in (4.2)) and torque-free spin rate, indicates that order 2 (squares) and 3 (triangles) yield almost identical results. The results with order 1 (open circles) clearly deviate and consequently order 1 is not sufficiently accurate. Three different resolutions have been checked: 4, 8 and 16 grid cells per radius. The difference between 8 and 16 cells per radius is small, while for 4 cells per radius there is a clear deviation. We can conclude that for a single particle 8 cells per radius and order 2 for the analytical expansion suffices to get acceptable accuracy.

Influence of resolution and order for two interacting spheres

For two interacting particles the order of the analytical expansion and the grid resolution needed to obtain accurate results may be different from the single particle case. Here we examine the influence of the computational parameters for several interaction situations. In table 6.1 the results for two particles with D_{cc} = 4 and $\theta = 270^\circ$ are displayed. Changing the order results in a 4% change of the force in the x–direction, a 1.5% change in the y–direction. Changing the resolution results in a change of about 6% in the x–direction, and again 1.5% in the y–direction. The particle spin proves very sensitive to both the order and the resolution for this case. Changing the order or resolution has a dramatic effect on the torque-free spin rate. The effect of the dramatic change in spin on the lift coefficient is only minor. As we will see in section § 6.3.3 the situation under consideration here (D_{cc} = 4, $\theta = 270^\circ$) is a worst-case scenario, since the force in the x–direction and the torque-free spin rate are changing dramatically when the particle is displaced slightly from its position. Therefore, the force in x–direction and the torque-free spin rate will not be so sensitive to the analytical expansion order and grid resolution in other simulation scenarios. When we consider for example particle interaction at the same angle, but at D_{cc} = 3, table 6.2 shows that changing the order of the analytical expansion has a far less dramatic effect on the forces and torque-free spin rate, only in the order of a few percent. The drag coefficient is compared with the value of Folkersma et al. [6] and the results agree. To obtain insight into the accuracy for different simulation conditions, in table 6.3 the results for order 2 and 3 are compared for the case when there is a particle above the reference particle at Re = 50. C_x shows a 2% change, Ω_P/ω changes by 12%. For the results in table 6.4 the reference particle is above the interacting particle at Re = 20; now the change in C_x is about 5%, in Ω_P/ω about 2%. For the simulations a grid resolution of 8 nodes per particle radius was adopted, and in most cases the order of the analytical expansion was set to 3. We expect to obtain results that would vary at maximum 2% in C_D by changing resolution or order. For C_x we expect an accuracy of about 5% and for Ω_P/ω about 10%, cases for which a small change in position causes a large change in C_x and Ω_P/ω excluded.

# nodes/R	order	C_D	C_x	Ω_P/ω
8	2	1.82	-4.52 10^{-2}	4.15 10^{1}
8	3	1.79	-4.35 10^{-2}	5.40 10^{1}
16	3	1.82	-4.11 10^{-2}	3.38 10^{1}

Table 6.1: Comparison between results with different resolution and order of the analytical expansion for two particles side by side, D_{cc} = 4, $\theta = 270°$, Re = 50, $Sr_\omega = 1 \times 10^{-4}$. Note that at these values of θ and D_{cc}, C_x and Ω_P/ω are very sensitive to small changes D_{cc} in as shown in figures 6.11 and 6.12.

# nodes/R	order	C_D	C_x	Ω_P/ω
8	2	1.69	-1.26 10^{-1}	2.62 10^{2}
8	3	1.69	-1.24 10^{-1}	2.54 10^{2}
[6]		1.69		

Table 6.2: Comparison between results with different resolution and order of the analytical expansion for two particles side by side, D_{cc} = 3, $\theta = 270°$, Re = 50, $Sr_\omega = 1 \times 10^{-4}$.

# nodes/R	order	C_D	C_x	Ω_P/ω
8	2	6.89 10^{-1}	1.77 10^{-4}	9.40 10^{-1}
8	3	6.89 10^{-1}	1.74 10^{-4}	8.40 10^{-1}

Table 6.3: Comparison between results with different resolution and order of the analytical expansion for two particles side by side, D_{cc} = 3, $\theta = 180°$, Re = 50, $Sr_\omega = 1 \times 10^{-4}$.

# nodes/R	order	C_D	C_x	Ω_P/ω
8	2	2.47	1.45 10^{-4}	1.10
8	3	2.49	1.38 10^{-4}	1.12

Table 6.4: Comparison between results with different order of the analytical expansion for two particles side by side, D_{cc} = 3, $\theta = 0°$, Re = 20, $Sr_\omega = 1 \times 10^{-4}$.

6.3.2 Particles along a line parallel to the axis of rotation

Figure 6.4 shows C_D, C_L and Ω_P/ω as a function of the domain size in axial direction normalized by the particle radius R, which equals the normalized center-to-center distance D_{cc} in axial direction between the particles. Results for Re = 20 are indicated by circles, for Re = 50 by squares; for all cases $Sr_\omega = 0.1$. For very small inter particle separation, equal or smaller than one particle radius, the results are indicated by gray symbols. Since there are only 8 grid points per particle radius, the number of grid points in the axial direction is for these cases very small and thus these results may be unreliable. When the distance between the particles is more than 10 particle radii, i.e. if the box is over 5 particle radii in each direction, the results remain constant and the particles no longer affect each other. The results for the drag coefficient are somewhat above those for the standard drag curve. Part of this is caused by the vorticity of the flow. As shown in chapter 3, table 3.1, an increase in Sr_ω increases the drag coefficient. Another cause for the increased drag force may lie in the finiteness of the box size. On the other had it is not unusual to find results somewhat above those of the standard drag curve in numerical simulations, see e.g. [1]. In general, when the particles are closely arranged on the line, they experience a higher drag. The torque-free spin rate decreases as d_{cc} decreases. Surprisingly, the lift coefficient shows an increase for decreasing d_{cc}. As indicated in chapter 3 and Bluemink et al. [2] an increase in Ω_P/ω causes an increase in C_L due to a Magnus-like effect. The increase in lift occurring when the spheres on the line parallel on the axis have a smaller separation distance, is a consequence of the displacement of the streamlines by the neighboring spheres.

6.3.3 Two particles interacting

Dependence on angle

For two interacting particles the orientation of the line joining their centers with to the incoming flow is very important. In figure 6.5 the effect of this orientation on the drag coefficient C_D is shown, while the center-to-center distance is kept constant at $D_{cc} = 4$ or 8. The results are for $Re = 50$ and with a small dimensionless vorticity $Sr_\omega = 1 \times 10^{-4}$, such that the flow is almost uniform flow. The dashed-dotted line indicates the drag coefficient for a single particle. When the reference particle is below the second particle, θ = 180°, we see a clear shielding effect: a strong decrease of the drag force. But also when the reference particle is above the second particle ($\theta = 0°$) the drag is decreased. An increase in drag is seen when the particles are arranged side-by-side with respect to the incoming flow. When the particles are at $D_{cc} = 8$, the increase is hardly noticeable. However, the decrease

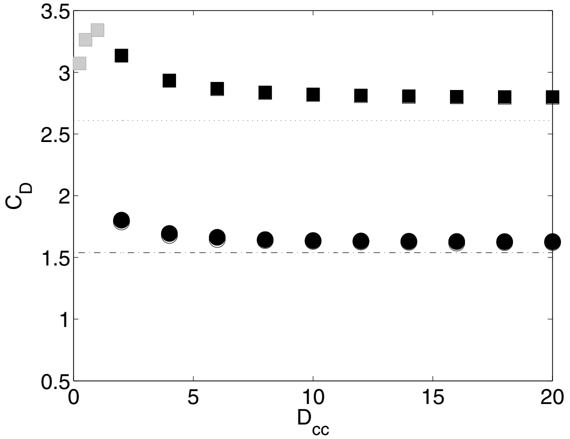
C_D
3.5
3
2.5
2
1.5
1
0.5
0
5
10
15
20
D_cc

(a)

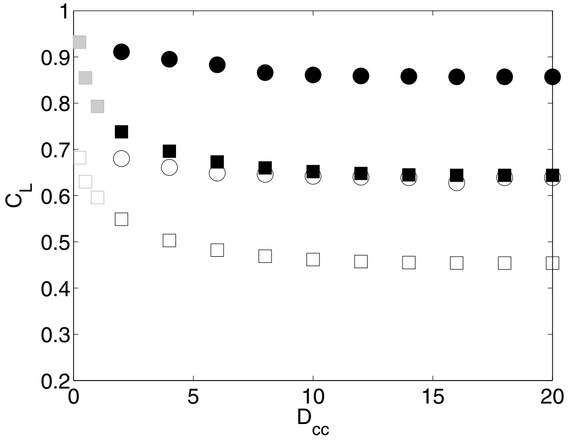
C_L
1
0.9
0.8
0.7
0.6
0.5
0.4
0.3
0.2
0
5
10
15
20
D_cc

(b)

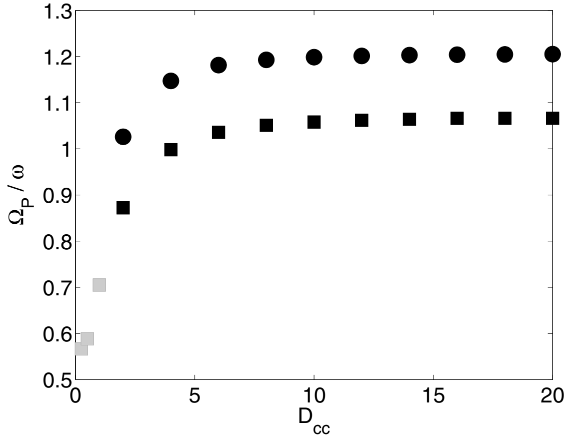
Ω_P / ω
1.3
1.2
1.1
1
0.9
0.8
0.7
0.6
0.5
0
5
10
15
20
D_cc

(c)

Figure 6.4: (on the previous page) Drag (a) and lift (b) coefficients and normalized particle spin rate (c) as functions of the distance between the spheres, normalized by the particle radius, for $Re = 20$ (squares) and $Re = 50$ (circles), $Sr_\omega = 0.1$. Closed symbols are for rotating spheres, open symbols for non-rotating spheres. Grey symbols indicate simulations where the box size is equal to or smaller than the distance between the spheres and the simulations may not have sufficient resolution to simulate such a situation. The dotted line in (a) represents the value of the standard drag curve at $Re = 20$, the dashed dotted line at $Re = 50$.

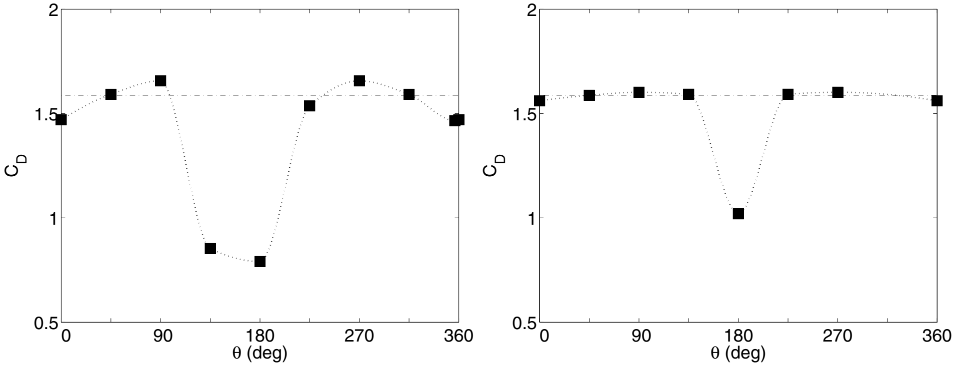

(a) (b)

Figure 6.5: Effect of varying the angle θ on C_D. Re = 50, $Sr_\omega = 1 \times 10^{-4}$. (a) D_{cc} = 4. (b) D_{cc} = 8. Dashed–dotted line is the result for a single particle. Dotted lines function as guide to the eye.

in drag due to the shielding effect is still strong. For the force in the lateral direction (expressed in C_x) we see that the particles are repelled when they are in the side-by-side arrangement ($\theta = 90°$ or $270°$) at the separation distances considered in figure 6.6. For D_{cc} = 4, the reference particle is repelled from the other particle, except around $\theta = 225°$. For D_{cc} = 8, the attraction and repulsion forces have decreased by a factor of 5 approximately and the result is more symmetric. Both at $\theta = 135°$ and $225°$ the lateral force is attractive. For these angles the fluid passes mostly along one side of the upper sphere as sketched in figure 6.8a, creating a low pressure at that side. For the upper sphere the force is always repulsive. However, in between the two particles the flow may accelerate and cause an attractive force for the lower sphere. Whether this acceleration occurs is however highly dependent on the exact situation. For example the conditions $\theta = 135°$, D_{cc} = 3, $Re = 20$, $Sr_\omega = 1 \times 10^{-4}$ give rise to a repulsive force. The flow field for this situation is

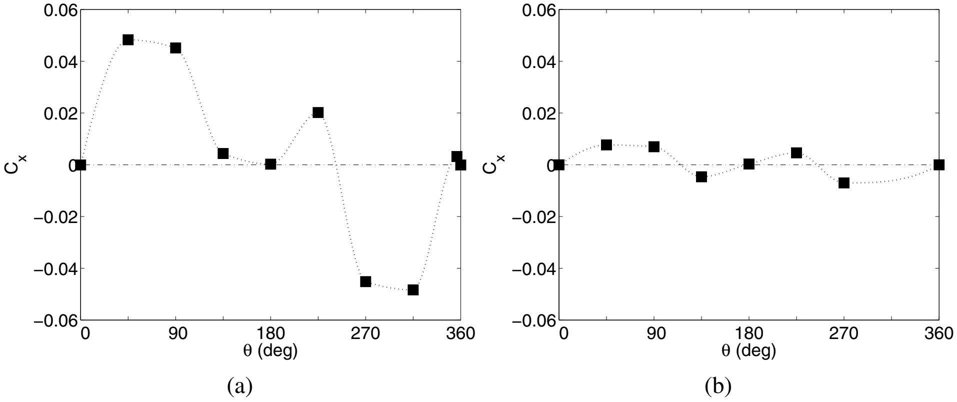

(a)

(b)

Figure 6.6: Effect of varying the angle θ on C_x. Re = 50, $Sr_\omega = 1 \times 10^{-4}$. (a) D_{cc} = 4. (b) D_{cc} = 8. Dashed–dotted line is the result for a single particle. Dotted lines function as guide to the eye.

shown in figure 6.8b. The fact that we don't see an attractive force when D_{cc} = 4, $\theta = 135°$, may be due to the curvature of the flow. Even though the rotation is small ($Sr_\omega = 1 \times 10^{-4}$) the flow deflects somewhat. For $y > 0$ it deflects to the left, for $y < 0$ to the right. In the case of $\theta = 135°$ it is as if the flow is tilted slightly so that it encounters a more side-by-side arrangement of the particle and the effect is a repulsive force.

For the particle spin rate figure 6.7 displays the following behavior: a nearly zero spin rate when the particles are oriented in line with the incoming flow, the top of the sphere rotating away from the other when they are arranged side-by-side. For the diagonal arrangements the direction of the spin rate depends on whether the reference particle is above or below. When it is above, the top of the sphere rotates in the direction of the other sphere. The presence of the bottom particle delays the flow separation from the surface of the top particle at one side, which causes the top of the upper particle to rotate towards the bottom particle. When the reference particle is below the other particle the top of it rotates away from that particle. Again the small dimensionless vorticity of the flow breaks the symmetry of figure 6.7a: the spin rates at θ = 225° and 315° are not as high as at 45° and 135°.

In figure 6.9 the effect of increasing the dimensionless vorticity is studied for $Re = 50$, $D_{cc} = 4$. The effect of increasing Sr_ω on the drag force is very small, although it is somewhat increased in the case of $\theta = 180°$. This is probably a result of the wake deflection of the top sphere, which decreases the shielding effect. Also

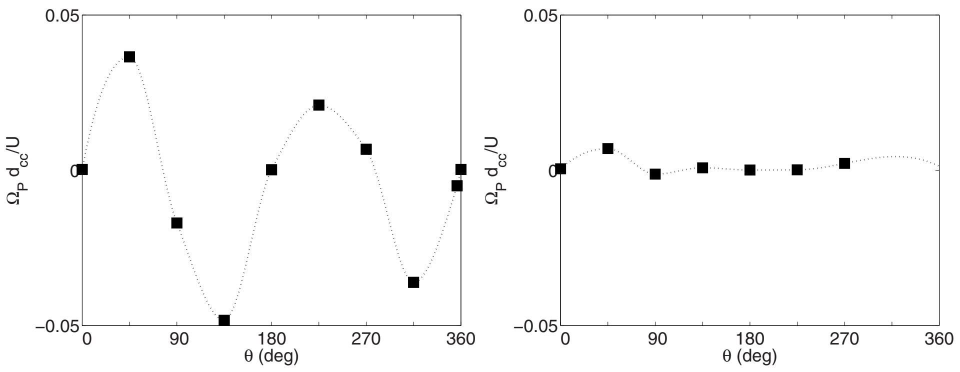

(a) (b)

Figure 6.7: Effect of varying the angle θ on $\Omega_P\ d_{cc}/U$. Re = 50, $Sr_\omega = 1 \times 10^{-4}$. (a) D_{cc} = 4. (b) D_{cc} = 8. Dotted lines function as guide to the eye.

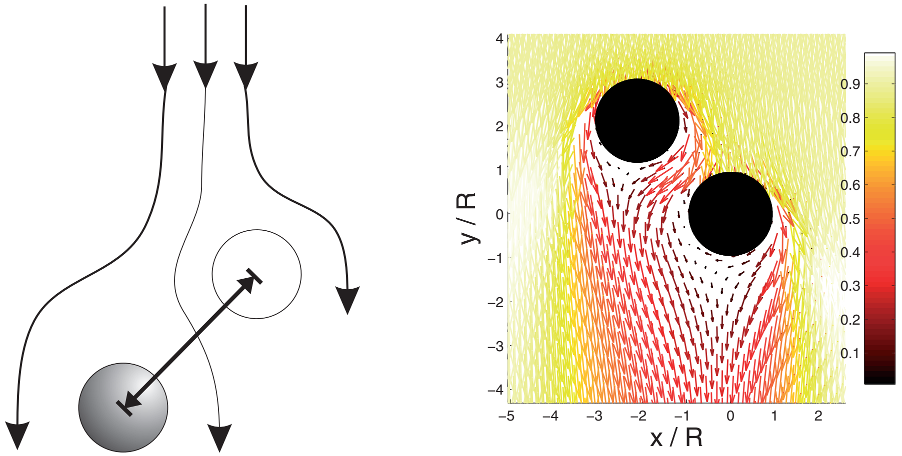

(a) (b)

Figure 6.8: (a) Sketch of the flow past two spheres with $\theta = 225°$. (b) Flow field for $Re = 20$, $\theta = 135°$, D_{cc} = 3, $Sr_\omega = 1 \times 10^{-4}$. The length of the arrows is proportional to the velocity. The color code is in units of the undisturbed velocity at the center of the sphere U_0.

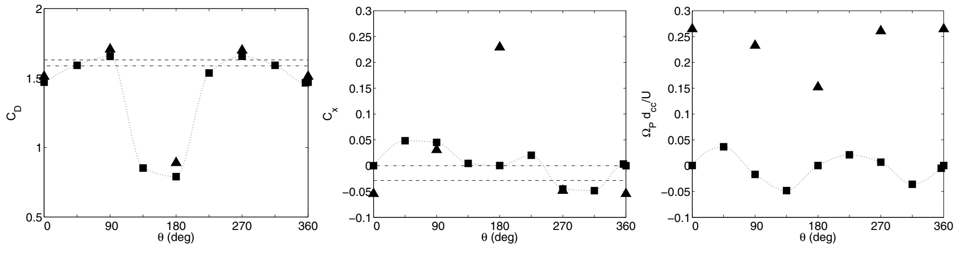

(a) (b) (c)

Figure 6.9: Effect of varying the angle θ on C_D (a), C_L (b) and $\Omega_P\ d_{cc}/U$ (c). Re = 50, $D_{cc} = 4$. Squares: $Sr_\omega = 1 \times 10^{-4}$, triangles: $Sr_\omega = 0.1$. The dashed–dotted line is the result for a single particle at $Sr_\omega = 1 \times 10^{-4}$. The dashed line is the result for a single particle with $Sr_\omega = 0.1$. Dotted lines function as guides to the eye.

the force in lateral direction shows little change due to a change in Sr_ω accept when θ is close to 180°. Here the sudden increase is also a consequence of the wake deflection. Due to the curvature of the flow, the wake of the upper particle is deflected somewhat towards the negative x–direction (since it is located on the positive y–axis). As a result the left side of the reference sphere is in the wake of the upper particle and the right side encounters a faster flow. This results in a force in the positive x–direction. The torque-free spin rate behaves quitely different for $Sr_\omega = 0.1$. The spin is mostly caused by the vorticity in the flow. However, the interaction changes the spin rate. For example, when there is a particle above the reference sphere, $\theta = 180°$, the spin rate decreases due to the wake of the upper sphere.

Dependence on distance

Although we have seen some effects of the distance on the forces and torque-free spin rate by comparing $D_{cc} = 4$ and $D_{cc} = 8$ results, we will now consider the forces for a fixed angle θ as functions of the center-to-center distance.

First we consider the side-by-side arrangement for $Re = 20$ and 50. Figure 6.10 shows the results for the drag coefficient. For $Sr_\omega = 1 \times 10^{-4}$ and both Reynolds numbers, the drag is high when the particles are close. As they are located farther apart, the drag takes the single particle value. The point for $D_{cc} = 3$, $Re = 50$, deviates from this trend. The order of the analytical expansion was 2 for this simulation. Presumably this order was too small to give an accurate result for two particles at such small separation. In general the drag force approximates

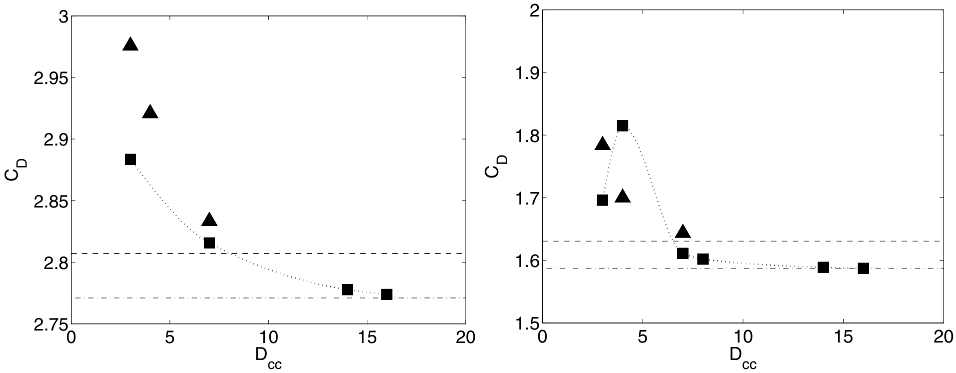

(a) (b)

Figure 6.10: C_D as function of D_{cc}, $\theta = 270°$. (a) $Re = 20$, (b) $Re = 50$. Squares: $Sr_\omega = 1 \times 10^{-4}$, triangles: $Sr_\omega = 0.1$. The dashed–dotted line is the result for a single particle at $Sr_\omega = 1 \times 10^{-4}$. The dashed line is the result for a single particle with $Sr_\omega = 0.1$. Dotted lines function as guides to the eye.

the drag force on a single sphere when $D_{cc} > 15$. For $Sr_\omega = 0.1$ the drag force approximates the drag for a single particle for smaller D_{cc}. In the x–direction for both $Re = 20$ and 50 the force is repulsive, figure 6.11. The repulsive force decays strongly for $D_{cc} < 7$. For $Re = 50$ a specifically steep decrease is seen between $D_{cc} = 3$ and $D_{cc} = 4$. The repulsive force approaches 0 at $D_{cc} \approx 15$. This is close to the center-to-center distance where the repulsive force changes into a weakly attractive force according to Kim et al. [10] and Folkersma et al. [6]. Since simulations with a large separation require a large domain, these are very costly and no simulations with $D_{cc} > 15$ were performed for this situation. When $Sr_\omega = 0.1$ the force in x–direction approaches zero at a smaller separation distance. The rotation rate for $Sr_\omega = 1 \times 10^{-4}$ approaches zero when $D_{cc} > 7$. For $Sr_\omega = 0.1$ the rotation rate will not approach zero but increases with D_{cc}. This is because a single sphere will spin fast in this flow and in the direction opposite to that caused by the interaction. As the spheres are farther apart, the opposing spin due interaction decreases and the total spin rate increases.

To consider the forces when the reference particle is above or below the interacting particle, we normalize the force with the force on a single sphere in this type of flow, in order to be able to display the results for both $Sr_\omega = 0.1$ and $Sr_\omega = 1 \times 10^{-4}$ in the same plot. (The lateral force and the spin rate normalized in the previous way are far smaller when $Sr_\omega = 1 \times 10^{-4}$ as compared to $Sr_\omega = 0.1$.) Figure 6.13 shows the drag results for $Re = 50$. Figure 6.13a displays

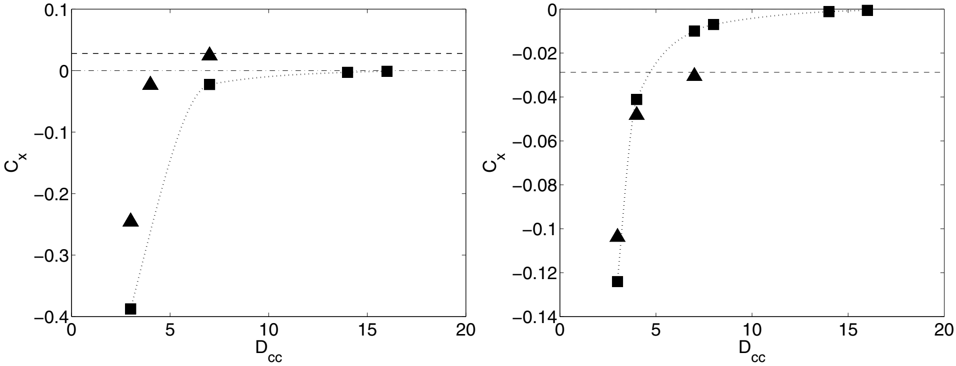

(a) (b)

Figure 6.11: C_x as function of D_{cc}, $\theta = 270°$. (a) $Re = 20$, (b) $Re = 50$. Squares: $Sr_\omega = 1 \times 10^{-4}$, triangles: $Sr_\omega = 0.1$. The dashed–dotted line is the result for a single particle at $Sr_\omega = 1 \times 10^{-4}$. The dashed line is the result for a single particle with $Sr_\omega = 0.1$. Dotted lines function as guides to the eye.

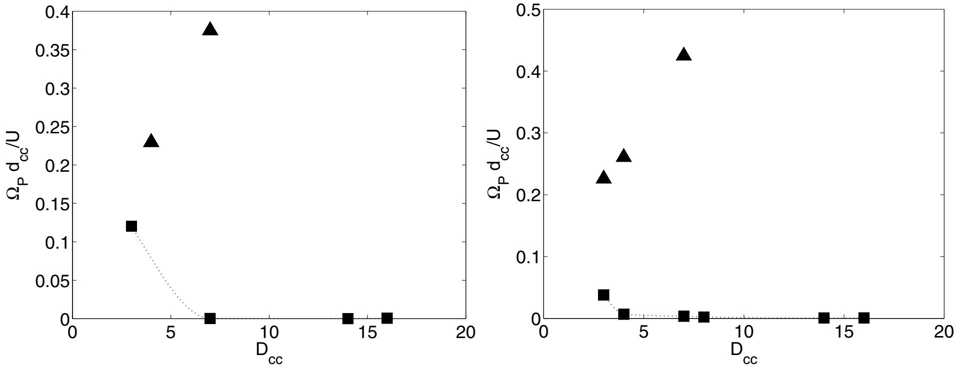

(a) (b)

Figure 6.12: $\Omega_P \, d_{cc}/U$ as function of D_{cc}, $\theta = 270°$. (a) $Re = 20$, (b) $Re = 50$. Squares: $Sr_\omega = 1 \times 10^{-4}$, triangles: $Sr_\omega = 0.1$. Dotted lines function as guides to the eye.

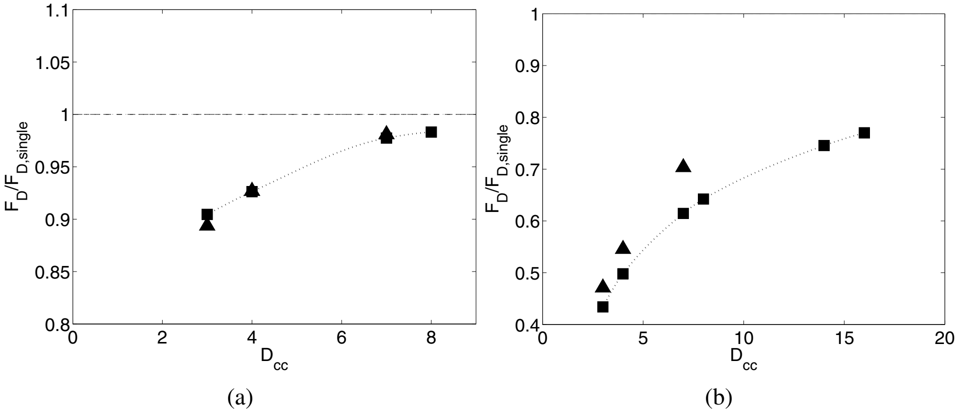

Figure 6.13: Drag force normalized by the single particle drag force as function of D_{cc}, $Re = 50$. (a) $\theta = 0°$, (b) $\theta = 180°$. Squares: $Sr_\omega = 1 \times 10^{-4}$, triangles: $Sr_\omega = 0.1$. Dotted lines function as guides to the eye.

the normalized drag versus D_{cc} for the situation where the interacting particle is below the reference particle ($\theta = 0°$). The drag on the reference particle is lowered by the particle below, and it becomes close to the single particle value at $D_{cc} = 8$. If however the reference particle is below ($\theta = 180°$), figure 6.13b indicates that even when $D_{cc} = 15$ the drag force is still about 20% smaller than the single particle value. Results for $Re = 20$ (not displayed here) show similar behavior. When $Sr_\omega = 0.1$, the results for $\theta = 0°$ remain the same, however the deviation from the single sphere case for $\theta = 180°$ is smaller due to the higher dimensionless vorticity. Probably this is caused by the wake deflection, which decreases the shielding effect. The lift force in figure 6.14a shows a steep rise between $D_{cc} = 3$ and 4 for both $Sr_\omega = 1 \times 10^{-4}$ and $Sr_\omega = 0.1$. After $D_{cc} = 8$ it approaches the single sphere value. However, when the reference particle is below the second particle as in figure 6.14b the particle will encounter a negative lateral force due to the interaction with the deflected wake of the upper sphere. It is unclear what separation distance in the y–direction is needed in order to have no interaction effects between the particles. To compare the spin rates in figure 6.12 the sphere spin rate was normalized with the flow rotation rate ω. The plots show that for the upper particle the effect of the lower particle is noticeable up to $D_{cc} \sim O(10)$. For the lower sphere however, the effect is increasing with D_{cc} at least for $D_{cc} < 15$ and it is not at all clear how far the spheres need to be separated to secure that the lower particle feels no longer any influence of the upper particle.

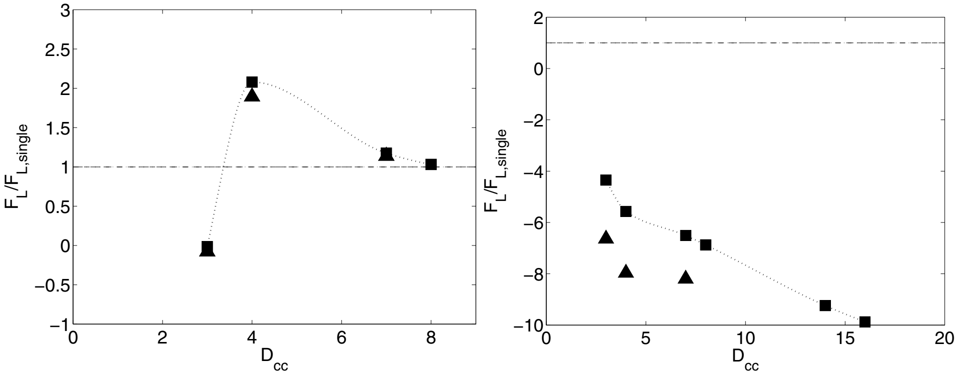

(a) (b)

Figure 6.14: Lift force normalized by the single particle lift force as function of D_{cc}, $Re = 50$. (a) $\theta = 0°$, (b) $\theta = 180°$. Squares: $Sr_\omega = 1 \times 10^{-4}$, triangles: $Sr_\omega = 0.1$. Dotted lines function as guides to the eye.

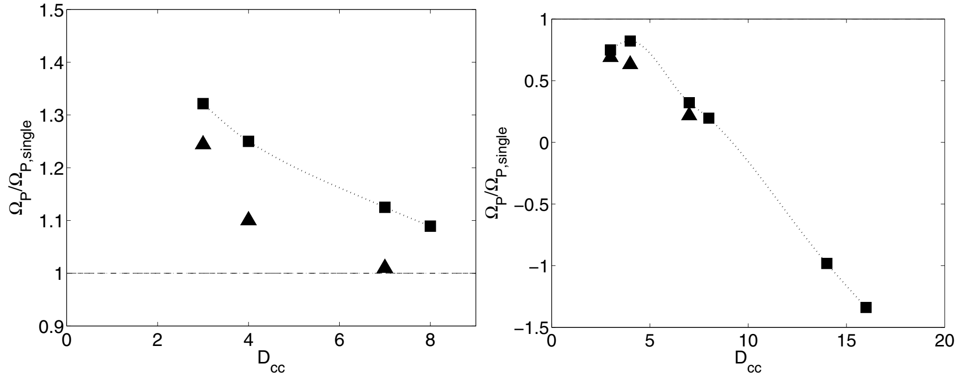

(a) (b)

Figure 6.15: Spin rate normalized by the single particle spin rate as function of D_{cc}, $Re = 50$. (a) $\theta = 0°$, (b) $\theta = 180°$. Squares: $Sr_\omega = 1 \times 10^{-4}$, triangles: $Sr_\omega = 0.1$. Dotted lines function as guides to the eye.

6.3.4 Experimental observations

When introducing several spheres in a viscous fluid ($Re \approx 5$), no steady state situation was reached. The particles tended to cluster in several groups, but the number of particles per cluster was varying in time, due to exchange of particles between the clusters. Inside the cluster two main types of behavior were seen. Spheres would align parallel to the cylinder axis and revolve around fixed points. Alternatively, two or three spheres would circle around each other in a plane perpendicular to the cylinder axis. No clear preference for one of the motions was observed. The particles were never seen to collide. This in contrast to bubbles, which were observed to collide (even several times) when in the same axial plane.

6.4 Conclusion

In this chapter several particle interaction situations in a solid body rotation were studied. For the numerical method employed for this investigation, a resolution of 8 nodes per particle radius and an analytical expansion order of 3 appeared to yield sufficiently accurate results for most cases.

In general, when particles are close and arranged side-by-side with respect to the incoming flow the drag increases. When they are in a line parallel to the axis of rotation, the lift force pointing in the plane perpendicular to the axis of rotation increases as the spacing between them becomes smaller, but their spin rate decreases. When the separation distance is more than 10 particle radii, a particle no longer feels the presence of the other ones.

If two particles are in a plane perpendicular to the axis of rotation the forces are very dependent on the angle of the particle pair with respect to the incoming flow. The results are comparable to previous work for most cases. This indicates that the effect of the flow field due to the solid body rotation is usually quite small. An exception is the case of a sphere directly under another sphere; in this case the wake deflection results in large lateral forces. For a particle separation distance of more than 15 particle radii the forces approach those on a single particle. Again when there is a particle above another this is no longer valid.

In general, to obtain a good approximation for the force on a sphere interacting with another sphere one should well consider the angle between the particle pair and the incoming flow if the separation distance between the particles is less than 15 particle radii. If the particles are arranged in line with the incoming flow, the effects extend much farther. For a solid body rotation, when the dimensionless vorticity is increased (from $Sr_\omega = 1 \times 10^{-4}$ to $Sr_\omega = 0.1$), the separation distance at which the single particle value is approached decreases.

References

[1] P. Bagchi. *Particle dynamics in inhomogeneous flows at moderate-to-high Reynolds number*. PhD thesis, University of Illinois, 2002.

[2] J. J. Bluemink, D. Lohse, A. Prosperetti, and L. van Wijngaarden. A sphere in a uniformly rotating or shearing flow. *J. Fluid Mech.*, 600:201–233, 2008.

[3] R. C. Chen and Y. N. Lu. The flow characteristics of an interactive particle at low Reynolds numbers. *Int. J. Multiphase Flow*, 25:1645–1655, 1999.

[4] P. C. Duineveld. *Bouncing and coalescence of two bubbles in water*. PhD thesis, University of Twente, 1994.

[5] B. Figueroa-Espinoza and R. Zenit. Clustering in high Re monodispersed bubbly flows. *Phys. Fluids*, 17:091701, 2005.

[6] R. Folkersma, H. N. Stein, and F. N. van de Vosse. Hydrodynamic interactions between two identical spheres held fixed side by side against a uniform stream directed perpendicular to the line connecting the spheres' centres. *Int. J. Multiphase Flow*, 26:877–887, 2000.

[7] J. Happel and H. Brenner. *Low Reynolds number hydrodynamics*. Prentice Hall Inc., Englewood Cliffs, 1965.

[8] J. F. Harper. On bubbles rising in line at large Reynolds numbers. *J. Fluid Mech.*, 41:751–758, 1970.

[9] J. F. Harper. Bubbles rising in line: why is the first approximation so bad? *J. Fluid Mech.*, 351:289–300, 1997.

[10] I. Kim, S. Elghobashi, and W. A. Sirignano. Three-dimensional flow over two spheres places side by side. *J. Fluid Mech.*, 246:465–488, 1993.

[11] J. B. W. Kok. Dynamics of a pair of gas bubbles moving through liquid. part 1: Experiment. *Eur. J. Mech B*, 12:541–560, 1993.

[12] D. Legendre, J. Magnaudet, and G. Mougin. Hydrodynamic interactions between two spherical bubbles rising side by side in a viscous liquid. *J. Fluid. Mech.*, 497:133–166, 2003.

[13] S.-C. Liang, T. Hong, and L.-S. Fan. Effects of particle arrangements on the drag force of a particle in the intermediate flow regime. *Int. J. Multiphase Flow*, 22 (2):285–306, 1996.

[14] L. Prahl, A. Hölzer, D. Arlov, J. Revstedt, M. Sommerfeld, and L. Fuchs. On the interaction between two fixed spherical particles. *Int. J. Multiphase Flow*, 33:707–725, 2007.

[15] M. C. Ruzicka. On bubbles rising in a line. *Int. J. Multiphase Flow*, 26: 1141–1181, 2000.

[16] A. S. Sangani and A. K. Didwania. Dynamic simulations of flows of bubbly liquids at large Reynolds numbers. *J. Fluid Mech.*, 250:307–337, 1993.

[17] P. Smereka. On the motion of bubbles in a box. *J. Fluid Mech.*, 254:79–112, 1993.

[18] R. Tal, D. N. Lee, and W. A. Sirignano. Heat and momentum transfer around a pair of spheres in viscous flow. *Int. J. Heat Mass Transfer.*, 11:1953–1962, 27.

[19] T. Tsuji, R. Narutomi, T. Yokomine, S. Ebara, and A. Shimizu. Unsteady three-dimensional simulation of interactions between flow and two particles. *Int. J. Multiphase Flow*, 29:1431–1450, 2003.

[20] Y. Tsuji, Y. Morikawa, and K. Terashima. Fluid-dynamic interaction between two spheres. *Int. J. Multiphase Flow*, 8:71–82, 1982.

[21] L. van Wijngaarden. The mean rise velocity of pairwise-interacting bubbles in liquid. *J. Fluid Mech.*, 251:55–78, 1993.

[22] D.-H. Yoon and K.-S. Yang. Flow-induced forces on two nearby spheres. *Phys Fluids*, 19:098103, 2007.

[23] H. Yuan and A. Prosperetti. On the in-line motion of two spherical bubbles in a viscous fluid. *J. Fluid Mech.*, 278:325–349, 1994.

[24] C. Zhu, S.C. Liang, and L.-S. Fan. Particle wake effects on the drag force of an interacting particle. *Int. J. Multiphase Flow*, 20:117–129, 1994.

Chapter 7

Conclusions and outlook

Throughout this thesis differences between particle and bubble behavior in a solid body rotating flow, as compared to a linear shear flow or uniform flow, have been discussed. In chapter 1 the importance of understanding bubble and particle behavior for several applications, industrial and natural was indicated. Some differences between particle and bubble behavior and some specifics of solid body rotation were discussed.

The results for the lift coefficient for bubbles in a solid body rotating flow in chapter 2 confirm the statement in the beginning of the thesis that the behavior of objects in a solid body rotating flow is qualitatively different from that in a linear shear flow. In the low Reynolds regime even negative lift coefficients were observed for reasonably spherical bubbles.

Chapter 3 explored torque-free spin rates of spheres in several types of flows. Experimentally and numerically it was shown that a sphere in a solid body rotating flow spins faster around its axis than the surrounding flow. By numerical simulation of different flow types it was shown that a shear component directed parallel to the main flow dramatically changes the spin behavior. A study of the stress distribution over the surface of the sphere indicated that a change in the location of flow separation is the basis for the change in spin rate for different flow types. The particle spin in turn changes the lift force. Surprisingly, when two different flow types are added, the spin rate obtained in the resulting flow is equal to the addition of the spin rates in the flows of which it is composed at Reynolds numbers of 20 and 50.

Chapter 4 explored drag and lift for solid spheres. The parameterization for lift and drag is quite different for spheres than for bubbles and also the effect of the vorticity contained in the solid body rotation differs. The lift coefficient rises logarithmically with the Reynolds number up to the critical Reynolds number where a sphere rising in a quiescent flow would start to display zigzagging or helical motion. After that the lift decreases with increasing Reynolds number. The normalized sphere spin rate increases linearly with the Reynolds number up to the critical Reynolds number. Comparing the numerical results for freely spinning spheres with non-spinning spheres indicates the effect of the spin on the lift force. Up to a Reynolds number of 200 the results show that the lift on a sphere can be decoupled into a flow-induced part and a spin-induced part. The spin-induced part has a same effect on the lift force in the solid body rotating flow as it has, according to previous results, in a linear shear flow.

Chapter 5 described an unexpected phenomenon occurring when asymmetrical particles or bubbles are injected in the solid body rotational flow: axial motion caused by the asymmetry of the object. The phenomenon was explained in terms of the stress distribution over the object.

In chapter 6 the interactions between two spheres have been explored. The results show that the angle between the line connecting the spheres and the incoming flow is very important for the forces that one sphere induces on another. The effect of the solid body rotation is particularly relevant when one sphere is above another. The wake displacement of the upper sphere then results in a lateral force on the lower sphere and the shielding effect of the drag is decreased by this wake displacement compared to a uniform flow.

In general regarding symmetrical objects in solid body rotation, the wake displacement behind the object is the common cause for different behavior of particles and bubbles as compared to a uniform flow or a linear shear flow.

In this thesis we studied the behavior of bubbles and particles. The particles experimentally studied have a density close to that of the fluid. As a result the equilibrium positions are not very stable. Future experiments with spheres with a much smaller density may yield more stable equilibrium positions. It would be of interest to compare the behavior of these light spheres with that of small spherical bubbles. Furthermore a more detailed analysis of the stability of the equilibrium position in different flow regimes is of interest for a better understanding of the behavior of spheres.

In the low Reynolds number regime the history force may be studied by experiments or numerical simulations. By analyzing the trajectories of a sphere or bubble one may be able to get a better insight in this force. In the simulations in this work the spheres were fixed to one location and the steady state situation was considered. By considering an unsteady situation or allowing the sphere to translate, an idea of the relevance of the history force at low but finite Reynolds numbers may be obtained.

Another aspect that could be studied is the way a large bubble deforms in a rotating flow and how this deformation changes the forces on it. Numerical results obtained by Front Tracking simulations can provide detailed information about the shape of the bubble.

Several other experiments can be devised. To further study the impact of a cross-stream shear on particle or bubble behavior, one could allow a particle of bubble to rise in a flow that is sheared in the direction perpendicular to the main velocity component. The effects of the wake deflection on the forces, the sphere spin or on an object below could be considered.

At Reynolds numbers of 20 and 50 we observed that the spin rate of a sphere in a composed flow is the addition of the spin rates the sphere obtains in the separate flows. It would be of interest to investigate up to what Reynolds number this additivity is valid.

The decoupling of the lift force into a flow-induced part and a spin-induced part has been shown to hold up to a Reynolds number of 200. It would be of great interest to see if the decoupling remains valid at higher Reynolds numbers.

Visualization experiments with bubbles, reported by others, have shown that tracer particles on a bubble's interface rotate faster that the surrounding flow in a solid body rotating flow. In future work one could see if the rotation of the bubble's surface causes the same effects on the lift force as we have demonstrated for a spinning sphere.

Numerical simulations of interaction situations over a wider range of Reynolds numbers would help towards the development of low-cost models for hydrodynamic interactions.

Summary

The behavior of bubbles and particles in flows is of interest from a fundamental point of view as well as relevant in many chemical, mechanical and environmental applications. Some forces on bubbles and particles are well known. Several parameterizations for the drag force are available, which cover a wide range of Reynolds numbers. These parameterizations are generally for a uniform flow. Less clear is how the drag changes for flows deviating from the uniform case. Other forces such as added mass and buoyancy are straightforward for every flow type. For the lift force, however, there is little agreement between different results. To experimentally study forces in a steady flow, a bubble or sphere (with a density smaller than that of the fluid) can be inserted in a horizontally rotating cylinder. If the cylinder is rotated with a constant rotation rate and sufficient spin-up time is allowed, the object will, in many cases, find an equilibrium position where all forces balance. By measuring the equilibrium position, two forces - the lift and the drag force - can be determined.

For bubbles, the parameterization of the lift force in a solid body rotating flow appears to be very different from that found in a linear shear flow. In the low Reynolds number range ($Re < 5$) the lift points toward the low-fluid-velocity side instead of the high-fluid-velocity side. The drag force behaves in a similar way to a linear shear flow, i.e. the drag rises as the velocity gradient over the sphere, normalized by the local flow velocity rises.

For particles, the lift behaves quite differently: direct numerical simulations of a pinned sphere show that it rises logarithmically with the Reynolds number up to $Re = 200$ when the sphere cannot spin. If the sphere is allowed to spin freely (as is the case in the experiment), both experimental and numerical results show a linear increase of the spin rate with the Reynolds number. Although the parameterization of the lift force on a sphere as function of the Reynolds number is completely different in solid body rotation from that in a linear shear flow, the effect of the spin on the lift force is similar, i.e. the spin increases the lift on the sphere. The rise in lift coefficient and spin rate break down when the Reynolds number exceeds the critical Reynolds number at which the wake behind a sphere in a uniform flow

loses its axisymmetry ($Re = 212$) or becomes unsteady ($Re = 274$).

In a solid body rotating flow several phenomena have been observed that are not found in other common flow types. The spin rate that a particle adopts under the torque-free condition is above the rotation rate of the solid body rotating flow. This is in contrast the linear shear flow case, where the spin rate of the sphere is smaller than that of the surrounding flow at finite Reynolds numbers. The results of careful examination of the shear stress distribution on the particle surface suggest that due to the flow component perpendicular to the main flow direction (the cross component), the separation is delayed on the high-fluid-velocity side of the sphere and advanced on the low-fluid-velocity side. As a result the sphere spins faster. The effect of the cross component is also translated in a deflection of the wake behind the sphere towards the rotation axis. As the Reynolds number increases, the shear stress and the wake deflection decrease. The relative difference in shear stress as well as the strength of the vorticity in the wake, however, increase. Consequently a sphere spins faster as the Reynolds number increases up to Reynolds numbers of 200. Numerical simulations of a straining flow or a shear flow with the shear perpendicular to the main flow component show similar behavior. The simulations of a sphere freely rotating in a linear shear flow, however, show a decrease of the spin rate with the Reynolds number, which is in agreement with previous findings. Surprisingly, when two different flow types are added, the spin rate obtained in the resulting flow is equal to the addition of the spin rates in the flows of which it is composed at Reynolds numbers of 20 and 50, values far beyond where one would expect such linear behavior.

Another phenomenon pertaining to the solid body rotating flow is the drift of asymmetrical particles: at certain conditions a (large) asymmetrical bubble or a particle with a broken fore-aft symmetry drifts back and forth along a line parallel to the cylinder axis, although the undisturbed flow has only components perpendicular to the cylinder axis.

Numerical results of interactions between two spheres show that the rotation component has a large effect when the particle pair is in line with the main flow component. Dramatic changes in forces occur as well when the particle pair is arranged diagonally with respect to the incoming flow.

Samenvatting

Het gedrag van bellen en deeltjes is zowel vanuit een fundamenteel oogpunt van belang als ook met het oog op vele chemische, mechanische en milieukundige toepassingen. Enkele krachten op bellen en deeltjes zijn bekend. Verscheidene parametrisaties voor de weerstand zijn beschikbaar, welke een groot gebied van Reynolds-getallen beslaan. Deze parametrisaties zijn over het algemeen geldig in een uniforme stroming. Minder duidelijk is hoe de weerstand verandert voor stromingen die afwijken van de uniforme stroming. Andere krachten, zoals de toegevoegde massa en de opwaartse kracht zijn eenvoudig voor ieder stromingstype. Voor de liftkracht is er echter weinig overeenstemming tussen verschillende resultaten. Voor het experimenteel bestuderen van krachten in een tijdsonafhankelijke stroming kan een bel of deeltje (met een lagere dichtheid dan die van de vloeistof) in een horizontaal roterende cylinder gebracht worden. Als de cylinder met een constante snelheid roteert en voldoende opstarttijd in acht wordt genomen, zal het object in veel gevallen een stabiel evenwichtspunt vinden waar alle krachten balanceren. Door het meten van dat evenwichtspunt kunnen twee krachten - de lift en de weerstand - worden bepaald.

Voor bellen blijkt dat de parametrisatie van de liftkracht in een roterende stroming sterk verschilt van die in een lineaire schuifstroming. Voor lage Reynolds-getallen ($Re < 5$) wijst de lift in de richting van de lage vloeistofsnelheid in plaats van in de richting van de hoge vloeistofsnelheid. De weerstand gedraagt zich op eenzelfde wijze als in een lineaire schuifstroming. De weerstand stijgt met de snelheidsgradient over het deeltje, genormalizeerd met de lokale snelheid.

Voor deeltjes gedraagt de liftkracht zich anders: directe numerieke simulaties van een gefixeerd deeltje laten zien dat de lift logaritmisch stijgt met het Reynolds-getal tot $Re = 200$ als het deeltje niet kan roteren. Als het deeltje vrij is om te roteren rond zijn as (zoals het geval is in het experiment) dan laten zowel de experimentele als de numerieke data een lineaire stijging van de rotatiesnelheid van het deeltje met het Reynolds-getal zien. Hoewel de parametrisatie van de liftkracht op een deeltje als functie van het Reynolds-getal totaal anders is in een roterende stroming vergeleken met een lineaire schuifstroming, is het effect van de rotatie van het deeltje op de liftkracht voor beide stromingen gelijk (de rotatie zorgt voor een stijging van de lift). De stijging van de liftkracht en de rotatiesnelheid van het deeltje om zijn as stoppen als het Reynolds-getal die waarde heeft bereikt waarbij het zog achter een bol in een uniforme stroming niet langer axi-symmetrisch is ($Re = 212$) of tijdsafhankelijk wordt ($Re = 274$).

In een roterende stroming worden verscheidene fenomenen waargenomen die niet gevonden worden in de meeste andere veelvoorkomende stromingen. De rotatiesnelheid waarmee een deeltje om zijn as gaat draaien zodat het momentvrije condities bereikt ligt boven die van de roterende stroming. Dit in tegenstelling tot de rotatiesnelheid van een deeltje in een lineaire schuifstroming, die lager ligt dan die van de omliggende stroming voor eindige Reynolds-getallen. De resultaten van nauwkeurig onderzoek van de schuifspanningsverdeling op het oppervlak van het deeltje suggereren dat door de stromingscomponent loodrecht op de hoofdstroom, de loslating aan de zijde van hoge stroomsnelheid vertraagd is en dat zij versneld is aan de zijde van lage stroomsnelheid. Als gevolg roteert het deeltje sneller om zijn as. Het effect van de stromingscomponent loodrecht op de hoofdstroom ziet met ook terug in een afbuiging van het zog achter het deeltje in de richting van de rotatie-as van de cylinder. Als het Reynolds-getal stijgt, verminderen de afschuifspanning en de afbuiging van het zog. Het relatieve verschil in afschuifspanning als ook de sterkte van de vorticiteit in het zog stijgen echter. Als gevolg daarvan roteert het deeltje sneller naarmate het Reynolds-getal stijgt tot Reynolds-getallen van 200. Numerieke simulaties van een schuifstroming met de verschuiving loodrecht op de hoofdstroom of een rekstroming laten gelijksoortig gedrag zien. De simulaties van een deeltje dat vrij roteert in een lineare schuifstroming laten echter een vermindering van de rotatiesnelheid van het deeltje met het Reynolds-getal zien, hetgeen in overeenstemming is met eerdere bevindingen. Een verrassend resultaat is dat wanneer twee stromingstypes opgeteld worden, de rotatiesnelheid die het deeltje bereikt gelijk is aan de som van de rotatiesnelheden in de afzonderlijke stromingstypes bij Reynolds-getallen van 20 en 50, ver voorbij de waardes waar men nog linear gedrag zou verwachten.

Asymmetrische deeltjes vertonen bijzonder gedrag in roterende stromingen. Bij bepaalde condities blijkt een (grote) asymmetrische bel of een deeltje met een asymmetrie (tussen voor-en achterkant) heen en weer te drijven langs een lijn parallel aan de cylinder-as, hoewel de onverstoorde stroming alleen maar componenten loodrecht op deze as heeft.

Numerieke resultaten van interacties tussen twee deeltjes laten zien dat de rotatiecomponent een grote invloed heeft als het deeltjespaar parallel aan de hoofdstroom staant. Sterke veranderingen in de krachten treden ook op als het deeltjespaar diagonaal ten opzichte van de hoofdstroom georiënteerd is.

Acknowledgements

The past four years I have had the great pleasure to work with many inspiring people, in the first place professors Leen van Wijngaarden, Detlef Lohse and Andrea Prosperetti. I would like to thank all three of them for their motivating words, great ideas, support, and help with writing papers. I would like to thank my promotor Detlef Lohse for the opportunity to carry out my PhD work. Our discussions and conversations have been a source of great motivation for me. Ever since Leen van Wijngaarden became my supervisor, I felt there was always someone available for all my questions. He has always been willing to give feedback on papers, abstracts and presentations. I also would like to thank him for his patience in explaining me the theoretical aspects of Fluid Mechanics. I would like to thank Andrea Prosperetti for our nice discussions and his great ideas for new simulations, experiments and ways to analyze data. Moreover, many thanks for the opportunity to visit his group in Baltimore, where I had the chance to attend several inspiring lectures and seminars and where I learned to work with the numerical method 'Physalis'.

I would like to thank professors Jacques Magnaudet, Rob Mudde, Jaap van der Vegt and Hans Kuipers for reading my thesis and being a member of my promotion committee. A special thanks to Jacques Magnaudet for many interesting discussions regarding unexpected results observed in rotating flows.

The work I carried out was sponsored by Technologiestichting STW, FOM, the ministry of economic affairs, Akzo Nobel Chemicals BV, DSM Research BV, Marin and Shell Global Solutions. Many thanks to the members of the project team, in particular professors Hans Kuiper and Jaap van der Vegt for their support during the user committee meetings, and to my fellow PhD students Lars Pesch and Dongsheng Zhang. I would also like to thank the other members of the user committee: Dr. ir. Niels Deen, Prof. dr. ir. G. Kuiper and Ir. J. Bosschers (MARIN), K. Al Bataineh and W. Harteveld (Shell), Dr. ir. B. P. B. Hoomans (DSM), Dr. ir. P. K. Ptasinski (Akzo Nobel), Dr. ir. J. Kockx (FOM) and Dr. ir. F. A. Karelse, Mariël Schweizer and Dorien van der Maat (STW).

I would like to thank our technicians Gert-Wim Bruggert and Martin Bos for their fantastic work on the setup, for joining me in considering the experimental procedure and for always being willing to manufacture or order whatever I needed. I would like to thank our system administrator Bas Benschop for retrieving several of my computers out of the 'Computer Bermuda Triangle' (located wherever I work, notion pertaining to Henk Jan). Moreover, he found a way to recover almost all my files from a broken back-up external hard disc after I had dropped my ordinary external hard disc (twice) to a point where it was beyond all hope and repair. I would like to thank our secretary Joanita Leferink for the many questions she answered and the many phone calls she made and emails she wrote on my behalf.

I would like to thank all people from the Physics of Fluid group. During the past four years I have had the privilege to carry out my research in a great working environment with a very friendly atmosphere. In particular I thank my roommates Henk Jan van Gerner, Marlies Overvelde and Álvaro Gómez Marín and my former roommates Ramon van den Berg and Sander van der Meer for making the office such a nice place, for being open to good discussions on physics or any other topic and for all the fun we have had.

A lot of details about path instability, the subject of the thesis of Christian Veldhuis, were explained to me by him. Thanks for the discussions on this and the help with planning my trip in Baltimore.

For my time in Baltimore I would like to thank Zhongzhen Zhang and Lorenzo Botto for showing me around and helping me to understand 'Physalis'. Without their help I could not have mastered the code.

I would like to thank the master and bachelor students I have supervised: Claas Willem Visser, Stijn Klaassen and Lars Weber. Performing experiments or discussing Fluid Dynamics with them was great fun. A special thanks to Claas Willem Visser for setting up the optical part of the setup and developing a big part of the measurement procedure, and to Lars Weber for his enthusiasm in doing PIV experiments.

Many thanks to Dennis van Gils for helping me to organize the visit of the primary school children at the end of 2007. Also to all PhD and master students of the group who participated with much enthusiasm in meetings about what experiments to set up, for all their efforts before and on the day itself.

Apart from the people of the Physics of Fluids group, I am indebted a lot to my friends and family. Many thanks to my parents for their never failing support and to Mart-Jan and Patricia for the beautiful time in New Zealand in 2006. Many thanks also to Liesbeth Bouwhuis and Bas van Schoonhoven, my 'Paranimfen', whose standing by me at my defence day is a very appropriate illustration of how they have supported me during my whole PhD time. Furthermore I would like to thank Annemieke Vliegen, who did far more for me than just help me with the cover design; Karin Truijen, with whom talking is so much fun that I can somehow keep doing it even when she has completely exhausted me by outracing me by bike. I would like to thank Jetse and Letizia for always giving me the feeling that I'm welcome for a good conversation or to stay at their place. I would further like to thank (in no particular order) Annemieke den Admirant, Cecile de Vos, Judith Prakke, and Maartje Damstra for our long friendships. A last thanks to many people at Aloha who made training the past four years a lot of fun.

Hanneke Bluemink
Enschede, November 2008

About the author

Johanna Jacoba (Hanneke) Bluemink was born in Utrecht, The Netherlands, on August 9, 1979. After living first in Oosterbierum, a small village in the North of the Netherlands, she moved to Apeldoorn and attended the last part of primary school and her secondary school ’het Stedelijk Gymnasium Apeldoorn’ there. She graduated from high school in May 1997. After that she went to Chili for ten months to tutor four of her Dutch cousins living there. Subsequently she studied Applied Physics at the University of Twente between 1998 and 2004. She co-organized a symposium titled ”Let’s Bubble” in 1999 and a study tour to Switzerland and Italy in 2001 and was involved in a number of other activities for the study association of Applied Physics ’Arago’. In 2002 she spend 5 months in Switzerland. She participated in the CERN Summer School and did her internship at the University of Geneva. She obtained her master’s degree in 2004, having done her research at the Physics of Fluids group of prof. Detlef Lohse, and she continued her PhD at the same group. During her PhD she spend about four months in Baltimore at the group of prof. Andrea Prosperetti. Having returned she started training for triathlon and later on became president of the board of the triathlon club ’Aloha’ of the University of Twente. After her defense she will travel around the world visiting Canada, New Zealand and Thailand to visit her family members and enjoy the sceneries. Apart from travelling she takes an interest in about everything, but, because it is quite exhausting to do so, she tries to focus on her friends, triathlon, hiking and philosophy. The last is demonstrated by the choice of her ’Paranimfen’ who both studied Philosophy of Science, Technology and Society.